Investigation of Paraxial Light Concentration and Homogeneously Trapped Two-Dimensional Optical Quantum Gases

Dissertation

zur

Erlangung des Doktorgrades (Dr. rer. nat.)

der

Mathematisch-Naturwissenschaftlichen Fakultät

der

Rheinischen Friedrich-Wilhelms-Universität Bonn

vorgelegt von

Erik Busley

aus

Neuwied

Bonn 2022

Angefertigt mit Genehmigung der Mathematisch-Naturwissenschaftlichen Fakultät der Rheinischen Friedrich-Wilhelms-Universität Bonn

1. Gutachter:	Prof. Dr. Martin Weitz
2. Gutachter:	Prof. Dr. Sebastian Hofferberth

Tag der Promotion:	12.5.2022
Erscheinungsjahr:	2022

Abstract

Trapped degenerate quantum gases in tailored environments allow for the investigation of otherwise unaccessible microscopic phenomena as they appear e.g. for the electron gas inside a solid. The field grew rapidly after the first Bose-Einstein condensate of dilute atomic gases was created in 1995, providing a very illustrative example for the effect of quantum statistics leading to a phase transition when the thermal wavelength of the constituent particles exceeds the mean interparticle distance. Apart from material particles, quantum gases of light can be realized in optical microresonators inside of which the photons interact with a medium. In the regime of strong coupling between photons and the medium, quasi-particles known as polaritons form. Those systems have allowed for the direct investigation of behavior such as superfluidity and superconductivity due to the here established combination of quantum degeneracy and instantaneous contact-like interaction. In our system, the photon gas is created inside a high-finesse optical microcavity that is filled with a liquid dye solution. The thermally related absorption and emission spectra of the dye molecules combined with the strong decoherence due to frequent molecular collisions of dye and solvent molecules allow for the creation of an ensemble that behaves closely to the ideal Bose gas. The short cavity length of several half wave lengths fixes the longitudinal mode number, rendering the gas two-dimensional. Variable potential landscapes for the photon gas can be established via mirror surface topographies, where spherically curved mirrors result in a harmonic oscillator potential for the photon gas and surface-structured plane mirrors can yield finite size box potentials.

In the present work, a quantum degenerate homogeneously trapped two-dimensional photon gas is experimentally realized, providing a novel platform for the investigation of uniform photon gases. Basic properties such as spatial, momentum and spectral distribution are successfully probed and found to be consistent with predictions for the ideal Bose gas at room temperature. Extraction of the specific heat for various photon numbers below and above criticality reveals the absence of a second-order phase transition as expected from theory. Mechanical tilting of one cavity mirror superimposes the trap with a linear potential gradient and allows from the responding density profiles to extract the equation of state and the isothermal compressibility of the gas. The latter is for the ideal Bose gas expected to diverge towards infinity when the system forms into a Bose-Einstein condensate as the macroscopically occupied ground state does not exert any pressure. Owing to the finite size of the sample, this behavior is validated in the quantum degenerate regime but breaks down in the condensed regime due to the nonzero ground state energy.

In other work carried out in this thesis, it is investigated if the apparatus can be employed as a so-called solar light concentrator, as an initially prepared "hot" photon cloud in a harmonic trap is expected to redistribute towards the trap center when cooled to ambient temperature via coupling to the dye heat bath as could potentially be useful for photovoltaic applications. Compared to observed light concentration in dye-doped thin glass-plates that capture a certain fluorescence angle, the here investigated approach relies on systematic reabsorption of trapped fluorescence. Despite observing a shrinking of the cloud, we find that optical losses in the system presently prevent the system from experiencing a phase space density increase.

Publication List

Parts of the presented work have been published:

- E. Busley, L. Espert Miranda, A. Redmann, C. Kurtscheid, K. K. Umesh, F. Vewinger, M. Weitz and J. Schmitt, *Compressibility and the Equation of State of an Optical Quantum Gas in a Box*, Science **375**, 1403–1406 (2022)

  DOI: 10.1126/science.abm2543

Further publications related to this thesis:

- C. Kurtscheid, D. Dung, E. Busley, F. Vewinger, A. Rosch and M. Weitz, *Thermally condensing photons into a coherently split state of light*, Science **366**, 894–897 (2019)

  DOI: 10.1126/science.aay1334

- C. Kurtscheid, D. Dung, A. Redmann, E. Busley, J. Klärs, F. Vewinger, J. Schmitt and M. Weitz, *Realizing arbitrary trapping potentials for light via direct laser writing of mirror surface profiles*, Europhysics Letters **130**, 5 (2020)

  DOI: 10.1209/0295-5075/130/54001

Contents

CHAPTER 1

Introduction

Light is universally employed in fields ranging from energy transfer, information processing and spectroscopy where a variety of technological advancements are based on decades of aforegoing basic research. For a long time, the sun was the only source of visible electromagnetic radiation accessible to humankind. With the taming of fire, the continuous process of an exothermic reaction, several 100 000 years ago [1] a controllable source of light and heat entered the accessible toolbox. Both light sources are related as they belong to the family of thermal emitters, where their internally equilibrated oscillators cause the body (outer shell of the sun or hot reaction products, respectively) to emit a radiation field that has the emitter temperature imprinted in its spectrum. The temperature also determines the radiation intensity leading to a dissipative energy flow to the environment, as both emitters are typically much hotter than their surrounding. The sun with its surface temperature of 5800 K provides a constant net energy flow towards the earth, keeping it at roughly 300 K and even nowadays remains the only external harvestable light – and thus energy – source.

Phase space compression of light via coupling to the environment could also be relevant in fields ranging from metrology to solar light collection [2–4]. Currently, in the field of luminescent solar light collectors, one aims for concentration of an initially undirected light field onto a smaller area, as predominantly motivated to reduce photo voltaic cell material usage [5]. Spatial light concentration has been observed in luminescent dye-doped transparent plates by capturing the emission falling into a certain angular cone via total internal reflection [4].

Identifying the light field to be comprised of quanta, namely the photons, immediately leads to the treatment of light as a quantum gas. In fact, recent technological advancements allowed for experimental creation and control of atomic quantum gases, exciton-polaritons or even pure photons in controlled environments; all of which provide a powerful platform for the studies of many-body physics in- and out of equilibrium [6–8]. Around 70 years after its initial proposal by Bose and Einstein [9–11], the first so-called Bose-Einstein condensate of trapped dilute gases was experimentally achieved with ultracold alkali atoms like ^{87}Rb or ^{23}Na [12, 13]. In the following years, further works focused on atomic quantum gases in harmonic or periodic lattice potentials until recent technological advancements allowed for the creation of homogeneous trapping potentials. Three-dimensional uniform quantum gases have been achieved with bosons [14] and fermions [15, 16]. Further two-dimensional uniform gases were realized with massive particles [17–19] as well as in thermalized photonic systems [8] like exciton-polaritons [20] or even pure photonic gases [21]. Contrary to an ensemble of exciton-polaritons – hybrid quasi-particles of matter and light – where contact interaction between condensate particles is provided by the material constituents, which allows for the observation of superfluidity and (second) sound propagation, the ideal Bose gas resembles the counterpart due to the absence of reasonable contact interaction, predominantly for the here covered pure photonic gas, allowing for mostly unbiased thermodynamic and statistical physics investigations.

The presented thesis deals with two-dimensional photon gases, which link the fields of photonics and material quantum gases. The photon gas is confined in a concave resonator imprinting a non-vanishing ground state energy for the photons that lies in the visible wavelength regime, in stark contrast to the omnipresent example of black body radiation. The latter has no low frequency cutoff and the thermodynamic ground state corresponds to the absence of light. In paraxial approximation, the dispersion relation of the cavity photons is equivalent to a massive particle in two dimensions. The resonator is filled with a liquid dye-solution whose absorption and emission spectra are related by a Boltzmann-like frequency scaling. Coupling to the photon gas happens via absorption and subsequent fluorescence processes, causing the light spectrum to ultimately acquire a temperature. In 2010, a research group in Bonn reported about experimental signatures of photon Bose-Einstein condensation in such a system [22] followed by groups in London [23], Utrecht [24], Twente [25] and Kaiserslautern (no publications yet, contributions to [26]). Photon gases in optical fibers are investigated in Haifa, Israel [27].

In the present thesis, first a novel approach for light concentration based on coupling of a prepared high-temperature photon gas to the dye environment is probed that reduces the transverse temperature of the gas, manifested as a decrease in spatial and momentum variance, which are measured as a function of the dye concentration and hence the reabsorption time. Spatial and momentum profiles of the photon gas are compared with respect to their initial configuration in the absence of heat bath coupling to investigate if a phase space density increase occurs. The second part of this thesis deals with two-dimensional photon gases in box potentials which are created via local mirror surface structuring. The flat potential can be superimposed with a linear gradient, realized via a mechanically tilted mirror. In such a system, thermodynamic quantities can be extracted from density profiles [28–33], which are related via an equation of state to parameters such as pressure, volume, chemical potential μ or temperature. The presented implementation has allowed for extracting the equation of state $n = n(\mu, T)$ as well as the isothermal compressibility $\kappa_T = n^{-2}(\partial n/\partial \mu)_T$ of the photon gas directly from the density response to the varied potential gradient, which are quantities not yet determined previously for an optical quantum gas. A classical gas is harder to compress as its density increases whereas upon emerging quantum degeneracy, the compressibility increases again and, in the limit of an infinite gas, diverges towards infinity. Since we are dealing with a finite size system, however, we observe that the nonzero ground state energy ultimately leads to a breakdown of the infinite system theory upon condensation, making the ensemble less compressible again.

Thesis Outline: In the following introductory sections the general scheme of the investigated two-dimensional photonic quantum gas and a phase space formalism is introduced, as well as the dye-filled microcavity apparatus, which here serves as the experimental platform. We will also discuss the basic thermodynamics of ideal two-dimensional Bose gases in a homogeneous environment and how the dye-filled microcavity could serve as a platform for solar light concentration. Chapter 2 deals with the principles of the experiment, i.e. the used dye medium as a thermalization mediator and the confining high-finesse cavity, with its photonic band gap characteristics and electric field eigenmodes. The interaction of trapped photons (discrete occupation of resonator modes) with the dye molecules can be well described by a grand canonical rate equation model that allows for straight forward Monte-Carlo simulations of the time evolution.

The experimental investigation of the feasibility of the presented apparatus as a solar light concentrator is covered in chapter 3. First, the available parameter space is probed via numerical calculations, which are later compared to experimental data. Chapter 4, which resembles the main part of this thesis, deals with the implementation and characterization of the new platform for homogeneously trapped photon gases. First, the gas is probed regarding its basic characteristics, namely the distributions in real and momentum space as well as the spectrum. The equation of state and the compressibility are extracted from the data obtained when superimposing the flat potential with a linear gradient introduced by mechanical tilting of one cavity mirror.

1.1 Photons in Equilibrium

Mechanical equilibrium is understood as a stationary state of an object where the net force acting on it is zero and thus no motion occurs. In thermodynamics, equilibrium refers to the internal state of a system with vanishing net macroscopic flow of matter or energy. To achieve thermal equilibrium in complex systems, the subsystems must be in thermal contact to each other to counteract gradients in e.g. temperature, pressure or chemical potential by exchanging energy or particles. Quantitatively, one defines the thermalization process as the minimization or maximization process of certain quantities, such as entropy S (microcanonical ensemble), Helmholtz free energy F (canonical) or the grand canonical potential [34, 35]. This thermodynamic formalism can in particular be valid also for a gas of photons. In the following, it will be demonstrated that although free photons hardly show any stationary characteristics or reasonable contact interaction [36], equilibrium properties can be mediated by coupling to an internally thermalized medium.

1.1.1 Ideal Bose Gas

When investigating thermodynamic properties of quantum gases, one distinguishes between two particle classes, namely fermions (carry half integer spin) and bosons (integer spin) with the latter also including photons as they carry a full spin quantum $s = 1$. A multi particle fermionic wave function experiences a sign flip under particle exchange. As a consequence, it will destructively interfere with itself which ultimately prevents two or more fermions from occupying the same quantum state (Pauli exclusion principle [37]). Bosons are not subject to this phenomenon and can multiply occupy a state, a regime referred to as quantum degenerate. In a thermalized Bose gas at temperature T one finds on average

$$\bar{n}_{\mu,T}(E) = \frac{g(E)}{\exp\left(\frac{E-\mu}{k_\mathrm{B}T}\right) - 1} \tag{1.1}$$

particles in states with energy E and degeneracy $g(E)$ – the Bose-Einstein distribution. Here, k_B is Boltzmann's constant and μ the chemical potential, which for non-interacting particles, is the energy required to add a particle to the system, $\mu = (\partial F/\partial N)_{T,V}$. Only $\bar{n} \geq 0$ is physically meaningful, which implies $\mu \leq 0$; if not otherwise mentioned, throughout this manuscript excitable energies will always be shifted such that $\min\{E\} \stackrel{!}{=} 0$. The (average) total particle number $\bar{N}$ of the system is obtained by summation over all single particle states

$$\bar{N} = \sum_i \bar{n}_{\mu,T}(E_i) = \int_0^\infty n_{\mu,T}(E)\,\mathrm{d}E \tag{1.2}$$

$$= \int_0^\infty \bar{g}(E)\left[\exp\left(\frac{E-\mu}{k_\mathrm{B}T}\right) - 1\right]^{-1}\mathrm{d}E \quad . \tag{1.3}$$

Here, the degeneracy was replaced by the density of states $\bar{g}(E)$, which is typically used for systems with a mode continuum, but can still represent discrete energy levels using the delta distribution function as $\bar{g}(E) = \sum_i \delta(E - E_i)$. At fixed temperature, $\bar{N}$ depends on μ only; In particular, for a given $\bar{N}$, μ will adjust such that (1.2) is fulfilled. At high temperatures or low particle numbers, i.e. $-\mu(\bar{N}, T) \gg k_\mathrm{B}T$, the -1 term in (1.2) can be omitted and the Bose-Einstein distribution merges into the Boltzmann relation

$$\bar{n}_{\mu,T}(E_i) \stackrel{-\mu \gg k_\mathrm{B}T}{\simeq} g(E_i) \cdot \exp\left(-\frac{E_i}{k_\mathrm{B}T}\right)\exp\left(\frac{\mu}{k_\mathrm{B}T}\right) \tag{1.4}$$

$$\propto \quad g(E_i) \cdot e^{-E_i/k_\mathrm{B}T} \tag{1.5}$$

where the fugacity $\exp(\mu/k_\mathrm{B}T)$ can be treated as a scaling factor that sets the total particle number N if necessary. The validity of this approximation is connected to the consideration if a system behaves classically or quantum mechanically, resulting from enhanced occupations of certain energy states. Referring to (1.5) is sometimes sufficient when estimating thermodynamic scaling laws as e.g. in sec. 4.6.

Spin Multiplicity and Polarization

The degeneracy of energy levels is not exclusively imprinted by the environment but with the principal spin quantum number s also includes an intrinsic property of the constituent particles. Possible spin vector projections onto a quantization axis are $\{s, s-1, ..., -s\}$ multiples of $\hbar$, where the number of possible projections, $2s+1$, is called (spin) multiplicity. For photons with $s = 1$ one would expect a multiplicity of $2s+1 = 3$. However, for a particle moving at light speed, the exclusively allowed configurations are parallel or anti-parallel arrangement of spin and momentum vector [38], causing the lack of a transverse component. Thus, the actual degeneracy of photon states only gains an additional factor of 2. Photon spin corresponds to circular polarization of the electromagnetic field, hence a linearly polarized photon is a superposition of forward and backward spin states. Their relative phase determines the polarization angle, e.g. horizontal or vertical. Polarization degeneracy is thus an equivalent term for spin multiplicity.

In the context of light matter interaction, however, this type of degeneracy might be partially lifted: For a photon to get absorbed by an atom via a dipole transition, the atomic dipole has to align with the polarization vector of the incident photon. Analogously, photon emission can prefer a polarization axis if the medium itself is polarized, as further discussed in sec. 4.3.2.

Low Temperature Behavior and Bose-Einstein Condensation

An outstanding property of quantum gases is their distinct behavior at low temperatures where quantum effects start to dominate the statistical properties. When the chemical potential of a Bose gas becomes comparable to thermal energy scales, $|\mu| \lesssim k_\mathrm{B}T$ (e.g. via cooling down the system at constant $\bar{N}$), the occupation numbers of single particle states with energy $E_i \lesssim k_\mathrm{B}T$ start to become overpronounced with respect to their Boltzmann counterpart value. Further, if $|\mu|$ becomes smaller than the energy of the first excited mode, the ground state becomes macroscopically occupied whereas all the excited modes saturate in their occupation, given by the finite maximum value of $n_{i,\max} = (\exp(E_i/k_\mathrm{B}T) - 1)^{-1}$ for $\mu = 0$. Upon reaching this regime, every additional particle occupies the motional ground state – the gas undergoes a phase transition to a Bose-Einstein condensate (BEC) [39]. This effect is reminiscent to liquefaction of water vapor when the relative humidity saturates at 100 %, hence the term "condensation".

The onset point of the phase transition can be determined by computing the total particle number N, i.e. integrating over all excited mode occupations like in (1.3) for vanishing chemical potential. At the transition point, the contribution of the ground state is negligible since $N_0 \approx 1$. However, it turns out that the integral diverges in certain cases and condensation is not possible for $T > 0$. Let the density of states be given by $\bar{g} = C_\alpha E^{\alpha-1}$ where C_α is a constant. The particle number in excited states at the transition temperature T_c is then given by

$$N_\mathrm{exc}(T_c, \mu = 0) = C_\alpha \int_0^\infty \frac{E^{\alpha-1}}{\exp(E/k_\mathrm{B}T_\mathrm{c}) - 1}\,\mathrm{d}E \tag{1.6}$$

$$= C_\alpha\,(k_\mathrm{B}T_\mathrm{c})^\alpha\,\Gamma(\alpha)\,\zeta(\alpha) \tag{1.7}$$

where $\Gamma(\alpha)$ is the gamma function and $\zeta(\alpha) = \sum_{n=1}^\infty n^{-\alpha}$ the Riemann zeta function. It follows from the latter, that the integral is only finite for $\alpha > 1$. Experimental Bose-Einstein condensed ensembles are most commonly three dimensional harmonically trapped atomic Bose gases [12,

40], where the density of states scales like $\bar{g} = C_3 E^2$ and hence $\alpha = 3$. Homogeneous three-dimensional gases ($\alpha = 3/2$) [14] or even two-dimensional harmonically trapped gases ($\alpha = 2$) were achieved recently [18], also including photonic systems [22, 23, 41].

For an infinite two-dimensional Bose gas in the absence of a trapping potential, one finds the density of states to be independent of the energy ($\alpha = 1$, cf. sec. 2.4.2) and hence the system does not condense for finite temperatures $T > 0$, as any number of particles can be accommodated by the excited states. However, experimentally one always deals with finite size (volume) systems, as any apparatus is spatially limited in its dimensions and no real world sample can be truly infinite. We show in sec. 2.4.2 that the finite spatial extent of the system allows for a quasi saturation of N_{exc} and correspondingly a macroscopically occupied ground state. It is debatable to speak of a phase transition in the thermodynamic sense here as it would have to be robust in the thermodynamic limit ($N, V \to \infty$) [42]. By probing the system response under external manipulation (e.g. applied pressure) one can make estimates about the regime where the sample behaves like a cropped infinite homogeneous system and where finite size effects dominate. For the photon gas studied in this thesis work, corresponding measurements are presented in chapter 4.

1.1.2 Black Body Radiation

The probably most omnipresent ideal Bose gas is the thermal radiation field of a black body. The latter refers to an idealized object that perfectly absorbs (and emits) incident radiation regardless of e.g. frequency, polarization or angle of incidence. If such a body comprises a closed box with side length L and volume $V = L^3$, the spectral energy density u between the walls reads

$$u(\omega, T) = \hbar\omega \frac{\omega^2}{\pi^2 c^3} \left[\exp\left(\frac{\hbar\omega}{k_{\mathrm{B}} T} \right) - 1 \right]^{-1} \tag{1.8}$$

$$\frac{\bar{N}(\omega, T)}{V} = \frac{\omega^2}{\pi^2 c^3} \left[\exp\left(\frac{\hbar\omega}{k_{\mathrm{B}} T} \right) - 1 \right]^{-1} \tag{1.9}$$

where in (1.9), the spectral energy density was converted into a spectral photon density. Note that in contrast to (1.1) the chemical potential here vanishes because the photon number is not a conserved quantity as photons can be created and annihilated inside the walls by thermal energy; $\bar{N}$ is entirely dictated by the temperature of the system. By comparing (1.9) to (1.3) one identifies the density of states per volume in free space as $\bar{g}_{\mathrm{free}}(\omega) = \omega^2/\pi^2 c^3$, which already includes a factor of 2 to account for an additional polarization degree of freedom.

This law was empirically discovered in 1900 by Max Planck [43]; several years later, Albert Einstein proposed the underlying mechanism of this light thermalization to be subsequent absorption and reemission of photons inside the walls of the enclosing medium, which microscopically are a set of oscillators that can absorb and emit photons [44, 45]. The transition rates per volume are given by the so-called Einstein coefficients A for spontaneous emission and B for stimulated absorption and emission. The last mentioned processes scale with the spectral energy density $u = u(\omega)$, hence one can write the transition rates between (un-)excited oscillators N_1, N_2 as

$$\frac{\partial}{\partial t} N_1 = -\frac{\partial}{\partial t} N_2 = -N_1 B_{12} u + N_2 B_{21} u + N_2 A_{21} \quad . \tag{1.10}$$

In the steady state, absorption and emission compensate each other, hence $\partial/\partial_t N_1 = \partial/\partial_t N_2 \stackrel{!}{=} 0$. Requiring that the wall itself is in thermal equilibrium, we know that

$$\frac{N_2}{N_1} = \exp(-\hbar\omega / k_{\mathrm{B}} T) \tag{1.11}$$

which yields the spectral energy density $u(\omega)$ as the above given expression (1.8) when the ratio of A and B is identified with the density of states in free space.

We see that a thermalized medium can imprint its temperature onto the coupled radiation field. The wall oscillators are here thermally excited, but we will see in sec. 2.5 that also an optically induced excitation of dye molecules (cf. sec 2.1) can imprint their temperature onto a light field if the sublevels in their respective ground and excited state are internally thermalized. Other than in a black body, one finds that the fluorescence process can here only change the frequency of the photon instead of removing it entirely. Therefore, the chemical potential does not vanish and such a system can, other than a black body, show signatures of Bose-Einstein condensation.

1.2 Phase Space Formalism

The here investigated photon gas in the microcavity can in the regime of low particle numbers be regarded as a classical collection of particles. Many of the extractable quantities such as local density, momentum distribution or the thermal wavelength can be described in the context of phase space density. Here, a brief introduction is given, first about the classical distribution as widely used for the experiments presented in chapter 3 and the quantum description of the thermal wavelength as it constantly appears in the context of homogeneously trapped photon gases, mostly in chapter 4.

In the Hamiltonian formalism of classical mechanics a non-interacting particle in k dimensions is characterized by its position $\boldsymbol{x} = (x_1, \dots, x_k)$ and momentum $\boldsymbol{p} = (p_1, \dots, p_k)$ vector. The corresponding equations of motion describe the time evolution of a system in the so-called phase space whose constituents are $\boldsymbol{x}$ and $\boldsymbol{p}$ [46]. The associated phase space density $\mathcal{D}(\boldsymbol{x}, \boldsymbol{p})$ yields the number of particles that occupy a certain point in phase space or, in the limit of a state continuum, the corresponding probability density distribution

$$\mathrm{d}N = \mathcal{D}(\boldsymbol{x}, \boldsymbol{p})\, \mathrm{d}^k x\, \mathrm{d}^k p \quad . \tag{1.12}$$

In a thermalized system the phase space density scales with the Boltzmann factor (1.5) (or, depending on the context, with the Bose-Einstein distribution (1.1), respectively) as

$$\mathcal{D}(\boldsymbol{x}, \boldsymbol{p}) \propto \exp\left(-\frac{\mathcal{H}(\boldsymbol{x}, \boldsymbol{p})}{k_\mathrm{B} T}\right) \tag{1.13}$$

where the Hamiltonian $\mathcal{H}(\boldsymbol{x}, \boldsymbol{p}) = |\boldsymbol{p}|^2/2m + V(\boldsymbol{x})$ consists of kinetic and potential energy $V(x)$ of a particle with mass m. The non-relativistic dispersion relation $E \propto |\boldsymbol{p}|^2$ imprints a Gaussian shape onto the distribution ρ of each momentum component

$$\rho(p_x) = \frac{1}{\sqrt{2\pi}\sigma_{p_x}} \exp\left(-\frac{{p_x}^2}{2\sigma_{p_x}^2}\right) \tag{1.14}$$

with $\sigma_{p_x} = \sqrt{m k_\mathrm{B} T}$, which is commonly known as the Maxwell-Boltzmann distribution [47]. This relation holds true for a variety of potential landscapes as long as quantum effects are negligible; in contrast, the spatial distribution $\rho(x)$ heavily depends on $V(x)$. In a harmonic potential $V(x) = 1/2 m\Omega^2 x^2$ with trapping frequency Ω the quadratic scaling with x leads to a Gaussian shape also for the spatial density distribution

$$\rho(x) = \frac{1}{\sqrt{2\pi}\sigma_x} \exp\left(-\frac{x^2}{2\sigma_x^2}\right) \tag{1.15}$$

with $\sigma_x = \sqrt{k_\mathrm{B} T/m\Omega^2}$. The final phase space density is the product of spatial and kinetic probability distribution along each dimension scaled with the total particle number N

$$\mathcal{D}(\boldsymbol{x}, \boldsymbol{p}) = N \prod_{i=1}^{k} \rho(x_i)\, \rho(p_i) \quad . \tag{1.16}$$

In the experiments described in chapter 3 we investigate a two-dimensional photon gas in a radially symmetric harmonic trap, i.e. we reduce the Cartesian axes (x, y) to a single radial coordinate r, i.e. $\sigma_r \equiv \sigma_x = \sigma_y$. On the optical axis ($x_i = 0, p_i = 0$) the phase space density then simplifies to

$$\mathcal{D}^{2\mathrm{D}}(\mathbf{0}, \mathbf{0}) = \frac{1}{4\pi^2} \frac{N}{\sigma_r^2 \, \sigma_{p_r}^2} \quad . \tag{1.17}$$

Photon number N and cloud widths σ_{r,p_r} are directly experimentally accessible. While the real space distribution of a trapped ensemble is obtained by imaging the emission onto a camera, the momentum space distribution is accessible by imaging in the opposite Fourier plane (see sec. 1.6).

1.2.1 Thermal De-Broglie Wavelength

A quantum particle does neither carry a fixed momentum nor is it located at a certain position but those two compose a set of conjugated variables, meaning that the product of their uncertainties always obeys $\Delta x \Delta p \geq \hbar/2$ [48] which renders the above mentioned classical formalism inapplicable to a certain extent. In fact, particles behave as matter waves and based on their momentum p can be assigned a de-Broglie wavelength $\lambda_{\mathrm{dB}} = 2\pi\hbar/p$. Below this length a particle abandons its point-like character and occupies a k-dimensional volume of $V \approx \lambda_{\mathrm{dB}}^k$. Many length scales in a thermal system such as particle density or the coherence length can be expressed based on the thermal wavelength λ_{th} of an ensemble of particles with mass m at temperature T. Due to the frequent occurrence, two distinct interpretations are explained in the following.

Statistical Physics A widely used definition of the thermal wavelength λ_{th} is base on statistical properties. Consider a k-dimensional box of side length L and volume $V = L^k$. For a massive particle the Hamilton operator solely contains kinetic energy terms with each dimension contributing a portion of $p_i^2/2m$. Assuming the energy levels of the box are separated by much less than $k_{\mathrm{B}}T$, the canonical partition function $\mathcal{Z}_{\mathrm{C}}$ can be approximated by an integral, which for a single particle ($N = 1$) in classical statistical mechanics reads

$$\mathcal{Z}_{\mathrm{C}} = \frac{1}{(2\pi\hbar)^k} \iint \exp\left(-\frac{\mathcal{H}(\boldsymbol{x}, \boldsymbol{p})}{k_{\mathrm{B}}T}\right) \mathrm{d}^k x \, \mathrm{d}^k p \tag{1.18a}$$

$$= \frac{1}{(2\pi\hbar)^k} \int_0^L \mathrm{d}^k x \int_{-\infty}^{\infty} \exp\left(-\frac{p_i^2}{2m} \frac{1}{k_{\mathrm{B}}T}\right) \mathrm{d}^k p \tag{1.18b}$$

$$= \frac{L^k}{(2\pi\hbar)^k} \sqrt{2\pi m k_{\mathrm{B}} T}^k \tag{1.18c}$$

$$\equiv \frac{V}{\lambda_{\mathrm{th}}^k} \tag{1.18d}$$

with

$$\lambda_{\mathrm{th}} \equiv \sqrt{\frac{2\pi\hbar^2}{m k_{\mathrm{B}} T}} \quad . \tag{1.19}$$

The factor $(2\pi\hbar)^k$ denotes the phase space unit cell volume which sets the correct units and acts as a normalization constant. Note that this expression of λ_{th}, which only depends on m and T, does on first glance not explicitly represent a physical quantity and is only meaningful in a statistical sense. However, when comparing it to spatial interpretations like the de-Broglie wavelength one finds for a particle with thermal momentum $p = \sqrt{2m\,k_{\mathrm{B}}T}$ that $\lambda_{\mathrm{dB}} = \sqrt{\pi}\lambda_{\mathrm{th}}$ or for the *average* de-Broglie wavelength of an ensemble at temperature T a value of $\bar{\lambda}_{\mathrm{dB}} = \pi\lambda_{\mathrm{th}}$ in two dimensions

or $\bar{\lambda}_{\mathrm{dB}} = 2\lambda_{\mathrm{th}}$ in three dimensions, respectively. The (temperature) scaling of λ_{th} is exactly the same for both the spatial and statistical interpretation with prefactor variations being of order unity.

Spatial Autocorrelation Another characteristic length scale of a quantum gas is its spatial coherence length, which can be interpreted as overlapping single particle wave packets. To quantify this aspect, one can calculate the range up to which a system interferes with itself, namely the first-order autocorrelation function $g^{(1)}(x,t)$. The Wiener-Khinchin-theorem [49, 50] relates the autocorrelation function of an ensemble to its power spectrum and applies to conjugated variable pairs, e.g. position and momentum [51, 52]. The theorem states that the autocorrelation function $g^{(1)}(x)$ can be obtained via the inverse Fourier transform of the power spectrum, here represented by the thermal momentum distribution $n(p)$:

$$g^{(1)}(x) \propto (\mathcal{F}_p^{-1} n(p))(x) \propto \int_{-\infty}^{\infty} n(p)\, e^{\mathrm{i}px/\hbar}\, \mathrm{d}p \tag{1.20}$$

$$\propto \int_{-\infty}^{\infty} \exp\left(-\frac{p^2}{2m\, k_{\mathrm{B}} T} + \mathrm{i}px/\hbar\right) \mathrm{d}p \tag{1.21}$$

$$= \exp\left(-\pi \frac{x^2}{\lambda_{\mathrm{th}}^2}\right) \quad . \tag{1.22}$$

In fact, the characteristic correlation length $\sqrt{\pi}\lambda_{\mathrm{th}}$ agrees with the above introduced value of λ_{th}. A more rigorous way to calculate $g^{(1)}(x)$ employs the Wigner quasi-probability function [53] which leads to the same result as (1.22) [54, 55].

The statistically motivated expression of λ_{th} in (1.19) shows strong relations to spatial interpretations of a particle volume since the obtained value scales correctly with the inverse average momentum of an ensemble. Hence, for normally distributed momenta, λ_{th} is a good expression for the variance of the distribution. Recalling phase space density as "particles per space per momentum" the expression reduces to

$$\mathcal{D}(\boldsymbol{x}) = n(\boldsymbol{x})\lambda_{\mathrm{th}}^k \tag{1.23}$$

representing the number of particles per box-like volume λ_{th}^k, determined by the temperature dependent momentum distribution or, similarly, the number of particles per phase space unit cell $(2\pi\hbar)^k$.

A system is said to behave classically as long as the coherence length is comparable to the width of a single particle wave packet, which can therefore be treated as point-like objects. For increasing phase space densities in a Bose-Einstein condensate, the contribution of the low energetic degenerate modes cause a drastic increase in the systems coherence length (see sec. 2.4.2) due to the bimodal phase space distribution. Here, the usage of (1.23) renders partially invalid.

1.3 Homogeneous Two-Dimensional Bose Gases

The behavior of a particle ensemble is not an exclusive property of the particle type but also depends on the confinement. For trapped quantum gases, different trapping potentials can imprint disctinct behavior, i.e. the scaling of certain thermodynamic quantities or the occurrence of phase transitions [39]. In the following we first discuss the density profile of homogeneously trapped 2D Bose gases and how any trap can be treated to be homogeneous on short length scales in the local density approximation. Further discussion of thermodynamic quantities can be found in sec. 2.4.2.

We start with the density of states

$$\bar{g} = \frac{mL^2}{2\pi\hbar^2} = \frac{1}{k_\mathrm{B}T}\frac{V}{\lambda_\mathrm{th}^2} = \text{const.} \tag{1.24}$$

which in the homogeneous system is an energy-independent constant and hence resembles the case of $\alpha = 1$, see sec. 1.1.1. As here, apart from the potential walls, the particles do not feel any spatially varying potential, the entire energy is stored in the kinetic components with wave vector (k_x, k_y), resulting in two degrees of freedom per particle. The here investigated photon gas can exchange energy and particles with the environment (heat bath, see section 1.4), hence we operate in the grand canonical regime of thermodynamics. The variables which determine the state of the system are temperature T and chemical potential μ, whereas the volume V is assumed to be constant in the following. A reasonable starting point for the discussion of thermodynamic properties is the derivation of the partition function. For independent bosons (in the absence of contact interaction) the grand partition function can be worked out exactly with the single particle eigenenergies E_i as

$$\mathcal{Z}_G = \prod_i \sum_{n_i=0}^{\infty} \exp\left(-n_i \frac{E_i - \mu}{k_\mathrm{B}T}\right) \tag{1.25a}$$

$$= \prod_i \left[1 - \exp\left(-\frac{E_i - \mu}{k_\mathrm{B}T}\right)\right]^{-1} \quad . \tag{1.25b}$$

All thermodynamics parameters can be obtained from $\mathcal{Z}_G$ [34, 56]. Thermal equilibrium is established when the grand potential

$$\mathcal{G}(T, V, \mu) = -k_\mathrm{B}T \, \log(\mathcal{Z}_G) \tag{1.26}$$

$$= \quad k_\mathrm{B}T \sum_i \log\left(1 - e^{(\mu - E_i)/k_\mathrm{B}T}\right) \tag{1.27}$$

$$= -k_\mathrm{B}T \frac{L^2}{\lambda_\mathrm{th}^2} \mathrm{Li}_2\left(e^{\mu/k_\mathrm{B}T}\right) + k_\mathrm{B}T \log(1 - e^{\mu/k_\mathrm{B}T}) \tag{1.28}$$

is minimized. $\mathrm{Li}_s(z) = \sum_{k=1}^{\infty} z^k \, k^{-s}$ is the polylogarithm. For the computation, the sum was converted to an integral over the density of states again which does not include the contribution of the ground state at $E_i = 0$ which hence has to be treated separately. $\mathcal{G}$ relates to macroscopic thermodynamic quantities via

$$\mathcal{G}(T, V, \mu) \quad = \quad \bar{U} - TS - \mu\bar{N} \tag{1.29}$$

$$\overset{\text{homog.}}{=} -pV \tag{1.30}$$

where the last mentioned pressure-volume relation (pV) is only valid for homogeneous systems in the absence of an external potential. Note that internal energy U and particle number N are only given by their mean value. Intuitively, one would assume the state of minimal energy is acquired when every particle occupies the ground state and hence $U = 0$. However, at finite temperature $T > 0$ the system carries a certain amount of energy. Additionally, the fluctuating particle number N can continuously add or remove energy to the ensemble. Thermal occupation of the single particles states (and hence increasing U) will then maximize the entropy S, where balancing both quantities ultimately yields the Bose-Einstein factor. Due to the equivalence of grand canonical and canonical ensemble for a well-defined mean particle number $\bar{N}$, the $\mu\bar{N}$ term could physically as well be treated as an internal energy offset [34]. The exact differential of the grand potential reads

$$\mathrm{d}\mathcal{G} = -S\mathrm{d}T - P\mathrm{d}V - \bar{N}\mathrm{d}\mu \quad . \tag{1.31}$$

from where the mean particle number $\bar{N}$ in the system can be calculated via

$$\bar{N} = -\frac{\partial \mathcal{G}}{\partial \mu} \tag{1.32}$$

$$\equiv N_0(\mu) + N_{\mathrm{exc}}(\mu) \tag{1.33}$$

$$= N_0(\mu) + \frac{mL^2}{2\pi\hbar^2} \int_0^\infty \frac{\mathrm{d}E}{\exp\left(\frac{E-\mu}{k_\mathrm{B}T}\right) - 1} \tag{1.34}$$

$$= N_0(\mu) - \frac{L^2}{\lambda_{\mathrm{th}}^2} \log\left(1 - \exp\left(\frac{\mu}{k_\mathrm{B}T}\right)\right) \tag{1.35}$$

with the ground state occupation $N_0 = 1/(\exp(-\mu/k_\mathrm{B}T) - 1)$. Eq. (1.35) cannot be formally solved for the chemical potential μ. However, when omitting the contribution of the (potentially macroscopically occupied) ground state μ is inferred from N_{exc} via

$$\mu = k_\mathrm{B}T \log\left(1 - e^{-N_{\mathrm{exc}}\lambda_{\mathrm{th}}^2/L^2}\right) \quad . \tag{1.36}$$

Here we see that for every excited particle number N_{exc} there exists a solution for the chemical potential μ such that (1.36) is fulfilled, which confirms the absence of a saturation driven Bose-Einstein condensate at finite temperature T.

1.3.1 Equation of State and Density Profiles

The equation of state of a thermodynamic ensemble relates extensive and intensive state variables of a system, i.e. it describes the state of matter under given physical conditions like pressure p, volume V, temperature T, particle number N or internal energy U [57, 58]. They are frequently used to describe the equilibrium state of classical as well as quantum gases and fluids. The probably most common equation of state is the ideal gas law

$$pV = Nk_\mathrm{B}T \tag{1.37}$$

which is valid at low phase space densities $\mathcal{D} \ll 1$ in the classical regime.

Since the density of states in the infinite (∞) 2D homogeneous system is energy-independent we get from (1.35) the density of the excited states $n_\infty(\mu) \equiv N_{\mathrm{exc}}(\mu)/L^2$ as

$$n_\infty(\mu) = -\lambda_{\mathrm{th}}^{-2} \log\left(1 - \exp\left(\frac{\mu}{k_\mathrm{B}T}\right)\right) \tag{1.38}$$

$$\mathcal{D}_\infty(\mu) = n(\mu)\,\lambda_{\mathrm{th}}^2 \tag{1.39}$$

which is one form of an equation of state $n = n(\mu, T)$ that can equivalently represent the phase space density (1.23) by multiplication with the squared thermal wavelength. The density contribution of the ground state has to be treated separately if necessary. The formalism can also be transferred to inhomogeneous systems, when the chemical potential is assigned a spatial dependence by including the potential energy term, $\mu(x) \equiv \mu_0 - V(x)$. This substitution is the "local density approximation" which is valid as long as $V(x)$ can be treated as locally homogeneous on lengths scales of λ_{th}. When the coherence length of the system exceeds λ_{th} e.g. by a macroscopic occupation of the ground mode, (1.38) does not anymore correctly map the local potential onto the corresponding particle density as we have only included the excited states for the calculation of the density profile.

In the classical regime of $|\mu| \gg k_\mathrm{B}T$, $n_\infty(\mu)$ can be approximated by

$$n_\infty(\mu) \simeq \lambda_{\mathrm{th}}^{-2} \exp(\mu/k_\mathrm{B}T) \tag{1.40}$$

$$n_\infty(x, \mu_0) \simeq n_0(\mu_0) \exp(-V(x)/k_\mathrm{B}T) \tag{1.41}$$

with $n_0 = \lambda_{\mathrm{th}}^{-2} \exp(\mu_0/k_\mathrm{B}T)$. The density in (1.41) formally is the classical occupation of the potential energy degree of freedom.

1.3.2 Compressibility

From the equation of state (1.38) one can directly obtain the compressibility of a medium which is a measure of its relative volume change $\mathrm{d}V/V$ as a response to a pressure change $\mathrm{d}p$. For an isothermal process the coefficient of compressibility κ_T is defined as the inverse bulk modulus

$$\kappa_T = -\frac{1}{V}\left(\frac{\partial V}{\partial p}\right)_{T,N} \quad . \tag{1.42}$$

In the context of quantum gases of light, it turns out handy to replace volume and pressure with more accessible quantities such as the local density as it can be measured directly via real space imaging. For this purpose we start from the Gibbs-Duhem relation [56]

$$\mathrm{d}p = n\mathrm{d}\mu + (S/V)\mathrm{d}T \quad . \tag{1.43}$$

For an isothermal process we have by definition $\mathrm{d}T = 0$ and hence get $\mathrm{d}p = n\mathrm{d}\mu$; from $n = N/V$ one finds $\mathrm{d}V = N/n^2\mathrm{d}n$ for constant N. Plugging into (1.42) yields the expression

$$\kappa_T = \frac{1}{n}\left(\frac{\partial n}{\partial p}\right)_{T,N} \tag{1.44}$$

$$= \frac{1}{n^2}\left(\frac{\partial n}{\partial \mu}\right)_{T,N} \tag{1.45}$$

which allows for determination of the isothermal compressibility using experimentally accessible and controllable quantities, i.e. density and chemical potential.

Compressibility Measurement via Potential Gradients

Measuring the compressibility of light turns out to be a nontrivial task when following (1.42). While the volume of a trapped light field can be inferred from its spatial extent, the mechanical pressure of roughly 1000 photons is not measureable with the here available methods. Additionally, neither of those quantities can be changed during a running experiment, in contrast to the related quantities used in (1.45). While the photon density can be directly measured from calibrated spatial images, the chemical potential can be inferred via the local density approximation as an offset μ_0 from the particle number N as in (1.3) combined with the spatially varying part given by the prepared potential environment $V(x)$, see sec. 4.6 for the experimental implementation. Here, an initially flat mirror is mechanically tilted which results in a shallow linear potential gradient, resulting in a spatial dependence in the chemical potential $\mu(x)$.

Variation of the external parameters such as μ_0 and the potential gradient $\partial V/\partial x$ allows to infer the equation of state $n(\mu)$ and the compressibility κ_T of the photon gas over a large range of densities as described in sections 4.7 and 4.8.

1.4 Experimental Environment: Dye-Filled Microcavity

The experimental setup used in this thesis is based on an high-finesse optical microcavity filled with a liquid dye solution, predominantly rhodamine 6G dissolved in ethylene glycol, as shown in Fig. 1.1a. The dye molecules are optically excited by a pump beam. Upon absorption of a photon, the rotational and vibrational (rovibronic) occupation of the dye molecule is frequently altered by internal conversion processes and collisions with the surrounding solvent molecules (timescales 10^{-12} s). Accordingly, the sublevels of the electronically excited state are Boltzmann-distributed. The same processes also occur within the ground state substructure, which ultimately connects,

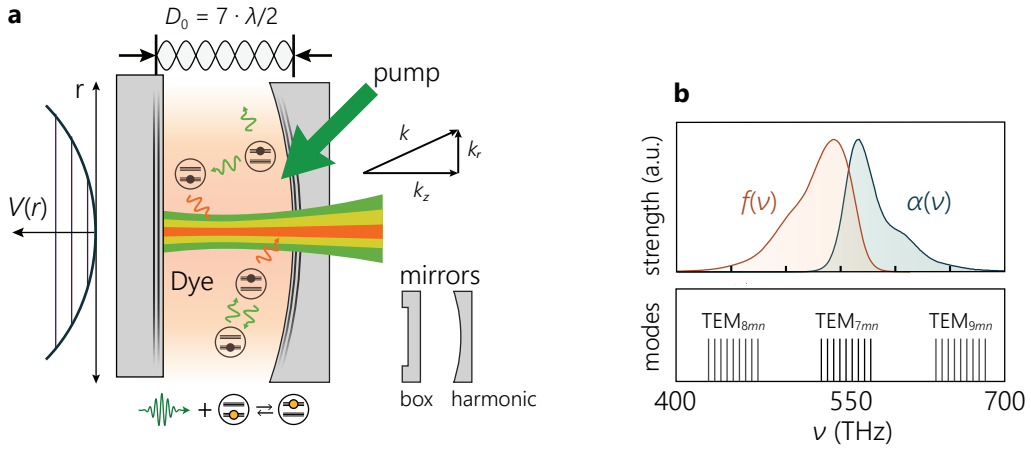

Fig. 1.1: Dye-filled microcavity environment. **a)** A liquid dye solution is enclosed by two highly reflective mirrors, which are only a couple of half waves apart, causing a frequency spacing of neighboring longitudinal modes larger than the dye bandwidth (panel b). The dye molecules are excited by a laser beam. Inside the cavity, reabsorption of emitted photons ultimately imprints a thermal distribution to the photon gas. The mirrors imprint a trapping potential onto the photons following their surface profile, in this thesis both spherical and box-like. Low energy photons propagate close to the optical axis, while photons in highly excited transverse modes leave the cavity with a large divergence angle. **b)** Only one longitudinal mode manifold overlaps with the dye spectra. The occupation of the transverse substructure (spacing determined by trapping geometry) contains thermal information of the gas.

within a certain spectral region, the absorption $\alpha(\omega)$ and fluorescence $f(\omega)$ strength of the dye molecules with the Boltzmann-like frequency scaling (Kennard-Stepanov relation, sec. 2.1)

$$\frac{f(\omega)}{\alpha(\omega)} \propto \omega^3 \exp(-\hbar\omega/k_\mathrm{B}T) \quad . \tag{1.46}$$

Statistically, a light field that undergoes several absorption and re-emission cycles inside such a dye medium, will acquire the temperature of the fluorescent molecules, which here act as a heat bath that can absorb excess energy or fill up energy deficits. Due to the frequent dephasing molecular collisions occurring well within the excited state lifetime of $\tau_\mathrm{spont} \approx 4\,\mathrm{ns}$, no quasi-particles known as exciton-polaritons are formed and the light field can well be considered as purely photonic.

The enclosing cavity mirrors provide a photon storage time of several hundred picoseconds, inferred from the (spectrally varying) mirror reflectance under normal incidence of around $R \approx 99.998\,\%$. The dye solution is typically concentrated at $\rho = 1\,\mathrm{mmol/l}$ and absorbs photons in the spectral region around 580 nm in roughly 50 ps, see sec. 2.1. For the light funneling experiments presented in chapter 3, the dye concentration is systematically varied to probe the effect of the reabsorption processes and eventual spectral redistribution, since the concentration ultimately relates the reabsorption time with respect to the resonator storage time.

On the optical axis, the mirrors impose a standing wave boundary condition onto the photons which results in an integer number q of wave nodes given by the mirror separation $D_0 = q\lambda_\mathrm{c}/2\tilde{n}$, where λ_c is called the cutoff wavelength and $\tilde{n}$ is the refractive index of the dye medium. Typical values are $q = 7$ or 8 result in $D_0 \approx 1.5\,\mu\mathrm{m}$ and cause the free spectral range of the microcavity to be around $\Delta_\mathrm{FSR} = \tilde{c}/2D_0 \approx 70\,\mathrm{THz}$, comparable with the dye bandwidth shown in Fig. 1.1b; $\tilde{c} = c_0/\tilde{n}$ denotes the speed of light in the medium. The mirror separation D_0 and hence λ_c can be adjusted such that only a single longitudinal mode with its transverse substructure overlaps with the dye spectra, which causes the trapped photon gas to be mainly restricted to a single longitudinal mode. This fixation to a certain half wave number reduces the dimensionality of the system as only the two transverse degrees of freedom characterized by transverse quantum

numbers (n_x, n_y) remain. Additionally, the photons obtain a non-trivial ground state energy $E = 2\pi\hbar c_0/\lambda_c$, corresponding to the resonators TEM_{q00} mode.

In order to trap photons in the transverse direction, the cavity mirrors have a concave geometry. It can be shown that the surface topography of the mirrors imprints an effective potential landscape onto the photons which in the transverse plane behave equivalently to massive quantum particles, see sec. 2.3. Thus, mirrors with radius of curvature $\tilde{R}$ will create a radially symmetric harmonic potential for the two-dimensional photon gas with trapping frequency $\Omega = \tilde{c}(D_0\tilde{R}/2)^{-1/2}$. On the other hand, recent advances in mirror surface structuring techniques allow for the creation of almost arbitrary potential landscapes [59, 60]. Here, to investigate homogeneously trapped photon gases, the mirror surface is locally elevated following the outline of a box potential, see sec. 4.1.

The thermodynamic information of the system is encoded in the occupation of the resonator eigenmodes, each having a specific excitation energy above the low energy cutoff. After a cascade of absorption and emission processes, one expects the occupation of the modes to follow a Bose-Einstein distribution if the dye fulfills the Kennard-Stepanov relation, see sec. 2.5. As here the occupation of the excited modes saturates, the gas shows the predicted characteristics for the phase transition to a Bose-Einstein condensate, including calorimetry and spatio-temporal coherence [22, 55, 61]. In the limit of low photon numbers, where stimulated emission processes can be neglected, the Bose-Einstein distribution can be approximated by the classical Boltzmann-distribution. Such information about the photon gas is obtained from the emission through the cavity mirrors. Suited optical arrangements allow for a straight forward acquisition of the photon distribution in real space, momentum space (k-space) and spectrally resolved.

Excited molecules at position x and photons in cavity mode i realize the excitations in the system. The interconversion rates of both species scale with the local squared amplitude of the photonic resonator modes and the corresponding dye spectra. The interchange dynamics between both can be modeled with rate equations as discussed in sec. 2.5 and one can show that the system at long times acquires a thermal distribution even in the presence of large losses in the molecular excitations. In chapter 3 the model is used to investigate light funneling of photons by the dye reservoir (sec. 1.5) by probing the central phase space density in the resonator as determined from the spatial and momentum distributions of the emission.

The central aspect of the present thesis focuses on 2D homogeneously trapped photon gases which are investigated by constructing a microcavity from two plane mirrors, one of which is surface structured with the outline of a box potential. Those experiments require superb mirror quality; a residual surface roughness of $\Delta D_{\mathrm{rms}} \approx 0.5\,\text{Å}$ already perturbs the intensity profile of low energetic transverse modes as the kinetic energy of respective photons falls below the noise potential caused by the sub-atomic roughness. In boxes of well-chosen size, we probe in a first stage general properties of the photon gas in terms of its spatial, momentum and spectral distribution across the classical, degenerate and condensed regime. By controlled tilting of the cavity mirror via piezo actuators we can extract the equation of state and the compressibility of the trapped gas from the surface density response, see chapter 4.

1.5 Luminescent Solar Light Concentrators

The presented thermalization mechanism inside a dye-filled microcavity could conceptionally be employed for solar light concentration [4, 5]. Liouville's theorem of classical statistical mechanics dictates that the phase space volume of a particle ensemble in a closed system is constant [62]. Consequently, for noninteracting particles, the phase space density (particles with the same momentum at the same position) does not surpass its maximum value given by the initial conditions. This constraint also applies to e.g. the transverse beam motion in particle accelerators and to classical ray optics, analogous to the Fourier limit: Focusing a beam to a small diameter at

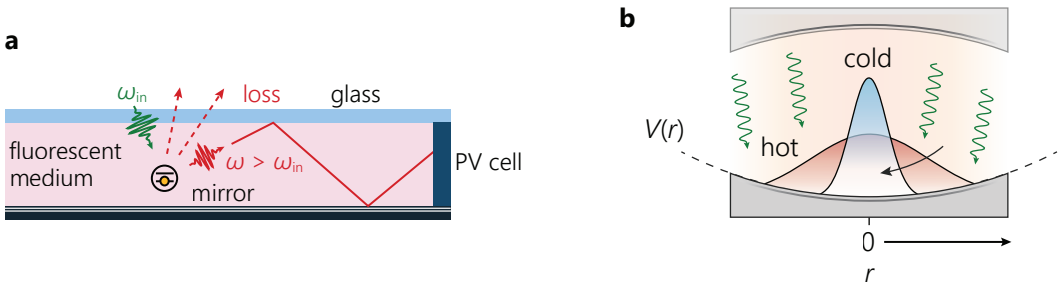

Fig. 1.2: Diffuse light concentrators. **a)** Working Principle of a conventional luminescent solar light collector plate. Dye molecules are excited by incoming light. A part of the undirected spontaneous fluorescence is trapped inside the structure due to total internal reflection and ultimately reaches a photovoltaic cell. **b)** Isotropic excitation of the dye (green arrows) creates a "hot" photon cloud as high energy states in the harmonic potential $V(r)$ are populated. Relaxation towards the trap center corresponds to transverse cooling of the cloud. The resonator mirrors are drawn to hint at the experimental implementation.

an interaction region goes in hand with an increase of the beam divergence in that certain spot. The ability to capture diffuse light, funnel it, and reshape it to a well-formed beam could be of great interest in e.g. future photovoltaic technologies.

A heat reservoir as provided by the dye environment can absorb the transverse kinetic energy and effectively reduce the beam temperature to room temperature. The reduction of the average transverse momentum imprints a spectral red shift to the photon gas (see dispersion relation in sec. 2.3.3), but their number count can in principle be conserved. The here used dye-filled microcavity establishes thermal contact between photons and a heat bath provided by a liquid fluorescent dye solution. Thermal coupling of the photon gas to the reservoir has been thoroughly investigated in previous studies [63–65].

The sun as our most prominent light source emits light with a low phase space density, especially on cloudy days when the light randomly scatters in the atmosphere. Conventional luminescent solar light collectors are based on thin glass plates that act similar to a waveguide mostly via total internal reflection, see Fig. 1.2a. Spontaneous fluorescence of excited dye molecules inside of the waveguide is partially captured when the emission falls within a certain solid angle. While this method concentrates light to a small area at the edge of the plate, its momentum distribution is still isotropic within the total internal reflection angle as the density of states is not modified here. In recent approaches, see e.g. in ref. [66], the efficiency can be increased by inducing permanent dipoles, which partially lift the isotropy of spontaneous emission. Those systems, however, do not increase the phase space density of the absorbed light as the momentum distribution is still mostly homogeneous within the capture angle of the glass plate and does not allow for a systematic reduction of the transverse beam temperature.

1.5.1 Light Concentration via Cooling

Measurements in refs. [22] and [65] hint at the spatial relaxation of the photon gas towards the trap center for increasing coupling to the dye. In the harmonic oscillator potential, where space and position are conjugated such that centrally located photons also propagate closer to the optical axis. A redistribution towards the cavity center can hence be seen as a reduction in temperature, with the principle schematically shown in Fig. 1.2b. An isotropically illuminated resonator corresponds to a hot beam temperature in the paraxial picture due to the large spread in their respective variances σ_r^2 and $\sigma_{p_r}^2$ as described in sec. 1.2. For an ensemble of N harmonically

trapped classical particles, the Hamiltonian reads

$$\hat{\mathcal{H}}(r,p) = \sum_i \left(\frac{p_{r,i}^2}{2m} + \frac{1}{2} m\Omega^2 r_i^2 \right) \tag{1.47}$$

$$\langle \hat{\mathcal{H}}(r,p) \rangle = 2Nk_\mathrm{B}T \quad . \tag{1.48}$$

One finds that each particle on average contributes an energy of $2\,k_\mathrm{B}T$. A cooling process would be evident if $\langle r^2 \rangle = 2\sigma_r^2$ and $\langle p_r^2 \rangle = 2\sigma_{p_r}^2$ are reduced. To quantify cooling one measures the second moments of the central phase space density with its temperature dependence of

$$\mathcal{D}(\mathbf{0},\mathbf{0}) \overset{(1.17)}{=} \frac{1}{4\pi^2} \frac{N}{\sigma_r^2\,\sigma_{p_r}^2} \tag{1.49}$$

$$\propto \; T^{-2} \tag{1.50}$$

The squared temperature dependence implies a strong increase of the phase space density when the ensemble is cooled down. Investigating measurements are presented in chapter 3.

1.6 A Lens as a Fourier Filter

Phase space density measurements require knowledge about the angular distribution (momentum space) of the paraxial light field in 2D, which can be measured with a regular lens. The working principle of the latter is often introduced via its deflection of straight propagating light rays. Diffraction based phenomena nevertheless have to be described in the wave picture to entirely understand the working principle.

Consider a wave propagating along the optical axis z. Following Huygens' principle [67, 68], every point of a wave front is the origin of a new spherical wavelet $E(r) = E_0 \exp(\mathrm{i}kr)/r$, where E_0 is the local complex amplitude of the electric field and r is the distance to the wavelet origin. The amplitude in the plane $(x, y, z = 0)$ is then connected to the field at (x', y', z) via the Fresnel-Kirchhoff diffraction integral

$$E(x',y',z) = \frac{k}{2\pi\,\mathrm{i}} \int_{-\infty}^{\infty} E(x,y,0)\,\frac{\exp(\mathrm{i}kr)}{r}\,\frac{1}{2}(1+\cos(\theta))\,\mathrm{d}x\,\mathrm{d}y \tag{1.51}$$

where we integrate over all partial contributions modified by a directional factor $(1+\cos(\theta))/2$, see Fig. 1.3a. We consider beams traveling close the optical axis (paraxial approximation), such that $\cos(\theta) \approx 1$, $(x'-x) \ll z$ and $(y'-y) \ll z$; hence we can expand r in the exponential as

$$r = \sqrt{(x'-x)^2 + (y'-y)^2 + z^2} \simeq z + \frac{(x'-x)^2}{2z} + \frac{(y'-y)^2}{2z} \tag{1.52}$$

and $z \approx r$ in the denominator since the amplitude varies much slower than the phase. Evaluating the simplified integral leads to

$$E(x',y',z) = \frac{k}{2\pi\mathrm{i}} \frac{e^{\mathrm{i}kz}}{z} \iint_{-\infty}^{\infty} E(x,y,0)\, e^{\frac{\mathrm{i}k}{2z}((x'-x)^2+(y'-y)^2)}\,\mathrm{d}x\,\mathrm{d}y \tag{1.53}$$

$$= E(x,y,0) * \left(\frac{k}{2\pi\mathrm{i}} \frac{e^{\mathrm{i}kz}}{z} e^{\frac{\mathrm{i}k}{2z}(x^2+y^2)} \right) \tag{1.54}$$

$$\equiv E(x,y,0) * h_z(x,y) \tag{1.55}$$

$$= \frac{k}{2\pi\mathrm{i}} \frac{e^{\mathrm{i}kz}}{z} e^{\frac{\mathrm{i}k}{2z}(x'^2+y'^2)}\, \mathcal{F}_{x,y}\left(E(x,y,0)\, e^{\frac{\mathrm{i}k}{2z}(x^2+y^2)} \right)(\nu_x,\nu_y) \tag{1.56}$$

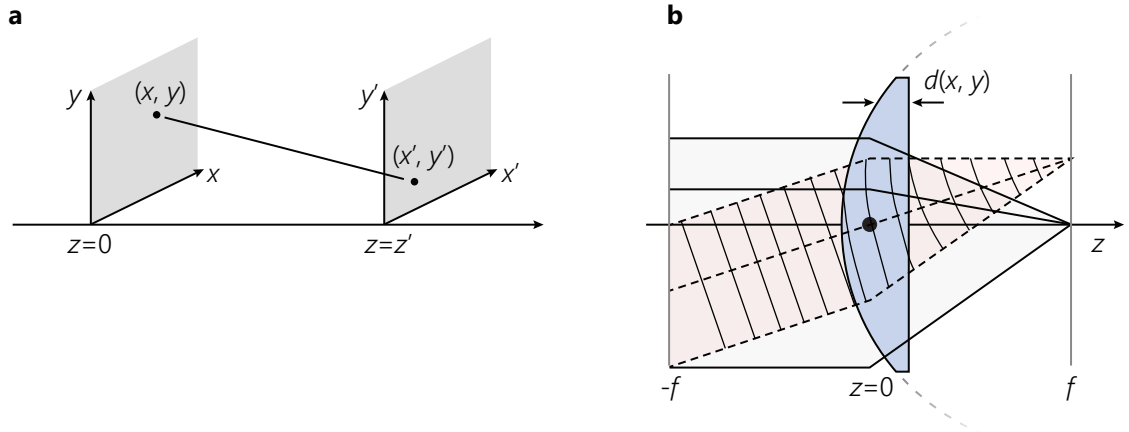

Fig. 1.3: a) Spatial variables in the diffraction planes. **b)** A lens focuses incoming beams with the same angle (or plane waves) onto a certain transverse position in the back focal plane. In the thin lens approximation, the refraction happens only in the central plane, $z = 0$.

where $*$ is the convolution operator and $h_z(x, y)$ is the impulse response of free space. We find that a free propagation along the axis by a distance z is described by a convolution of the initial field with $h_z(x, y)$ and turns out to be a Fourier transform of the initial field multiplied with a quadratic phase factor. The corresponding transformation variables here are the spatial frequencies $\nu_x = kx'/z$ and $\nu_y = ky'/z$ in the detection plane.

We now discuss the effect of a plano-convex lens, i.e. a glass body with refractive index n_L in the beam path, see Fig. 1.3b. Its focal length f is connected to its radius of curvature R via lensmaker's formula $R = f(n_\mathrm{L} - 1)$ [69]. A spherically curved surface on a substrate with thickness d_0 has the radially changing thickness

$$d(x, y) = d_0 + \sqrt{R^2 - (x^2 + y^2)} \overset{x,y \ll f}{\simeq} d_0' - (x^2 + y^2)/2f(n_\mathrm{L} - 1) \tag{1.57}$$

where d_0' represents all constants. When traversing the lens, the wave acquires an additional position dependent phase delay with respect to free propagation scaling quadratically with the distance from the optical axis which can be written as a multiplicative transfer function

$$T_\mathrm{L}(x, y) = e^{-\mathrm{i}kd_0'}\, e^{\mathrm{i}kd(x,y)(n_\mathrm{L}-1)} = e^{-\mathrm{i}k(x^2+y^2)/2f} \quad . \tag{1.58}$$

Now consider the field to be located in the back focal plane of a lens, $z = -f$. After propagating a distance $\Delta z = f$ it traverses the lens and propagates for another $\Delta z = f$ until the back focal plane of the lens where the electric field is then given by

$$E(x', y', f) = \big((E(x, y, -f) * h_f(x, y)) \times T_\mathrm{L}(x, y)\big) * h_f(x, y) \tag{1.59}$$

$$= \frac{k}{2\pi\mathrm{i}} \frac{e^{2\mathrm{i}kf}}{f} \big(\mathcal{F}_{x,y} E(x, y, -f)\big)(\nu_x, \nu_y) \tag{1.60}$$

which, up to a propagation prefactor, is an exact spatial Fourier transform of the electric field distribution in the opposite focal plane. An oblique plane wave traveling at angles (θ_x, θ_y) to the optical axis thus transforms like

$$E(x, y) = E_0 \exp\big(\mathrm{i}kx \sin(\theta_x) + \mathrm{i}ky \sin(\theta_y)\big) \simeq E_0 \exp\big(\mathrm{i}k(\theta_x x + \theta_y y)\big) \tag{1.61}$$

$$\equiv E_0 \exp(\mathrm{i}k_x x + \mathrm{i}k_y y) \tag{1.62}$$

$$\mathcal{F}_{x,y}(E(x, y))(\nu_x, \nu_y) = E_0\, \delta(\nu_x - k_x)\, \delta(\nu_y - k_y) \tag{1.63}$$

where δ is the delta distribution. From the screen position x' one can then infer the propagation angle before the lens via the relation

$$x' \simeq \theta_x f \quad . \tag{1.64}$$

Every light field can be decomposed into a superposition of plane waves at different propagation angles via a Fourier analysis, hence one can from the signal in the detection plane infer the occupation of transverse momentum states or, analogously, the angular photon distribution. Although the dispersion relation in the employed microcavity results in a transverse wave vector $k_x \approx k_z \tan(\theta)$ (see sec. 2.3.3), both results are equivalent for small angles.

We find that with a lens we can obtain the Fourier transform of a transverse electric field distribution $E(x, y)$ which simultaneously yields the transverse momentum distribution required for the phase space density measurements in chapter 3.

CHAPTER 2

Photons in a Dye-Filled Optical Microcavity

The experimental centerpiece used in the present thesis is a dye-filled optical microcavity which hosts the two-dimensional photon gas. For paraxial beams, the high-finesse resonator transforms the density of states from a continuum to a finite set of stationary wave functions. The occupation of those modes with photons can be described statistically when photon reabsorption in the enclosed dye medium occurs on a timescale shorter than the storage time.

The thermalization mediator, the fluorophore rhodamine 6G, is introduced regarding its electronic level structure and how this heat bath can imprint a temperature onto the photon gas. The photon dispersion relation inside an optical resonator becomes equivalent to that of a massive particle; the eigenmodes are derived for various trap geometries and their implications for the statistical physics are discussed. Finally, a rate equation model is presented where the light-matter interaction is modelled via a cascade of discrete absorption, emission, pump and loss processes.

2.1 Dye: Rhodamine 6G

As known from black bodies, repeated absorption and emission of photons in fluorescent walls can lead to a thermal spectral distribution of the light field if the wall oscillators themselves are in thermal equilibrium (cf. sec. 1.1.2), i.e. their internal state occupations scale with a Boltzmann-factor (1.5). The medium then imprints its spectral temperature T_{spec}, which in an ideal system equals the thermodynamic temperature, onto the light field. A related procedure can occur via fluorescent coupling of two electronic levels that have a thermally occupied substructure, which allows for a freely tunable chemical potential. Here we will discuss relevant properties of the fluorophore rhodamine 6G (in the following referred to as "dye"), which is employed in this thesis work. Similar properties hold true for a large group of organic dyes [70].

2.1.1 Electronic Structure and Spectra

For experiments based on repeated absorption and emission of photons in a medium, the key property is the relation of the corresponding transition rates. The molecular formula of rhodamine 6G reads $C_{29}H_{31}N_2O_3Cl$ which accounts for 65 atoms per molecule [71]. The complex interaction of individual constituents causes the level structure and hence the absorption and emission spectra of such molecules to significantly differ from single atoms or even simple molecules such as H_2. Figure 2.1a shows the electronic states and the transition mechanisms between them in a Jablonski diagram. In the here shown simplified picture, the electronic properties of a dye molecule can be described as a spectrally broadened two-level system. The ground state is a spin singlet state with angular momentum of 0 (S_0); excitation mainly happens via a dipole transition of a single electron to the S_1 level. The broadening of both states is a consequence of rotational

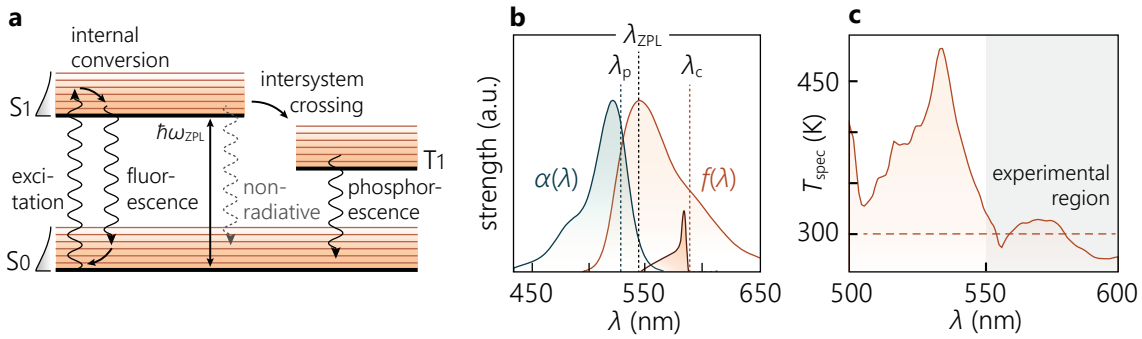

Fig. 2.1: Rhodamine 6G. **a)** Simplified Jablonski diagram. Various processes lead to transitions of electrons between the singlet (S) and triplet (T) state(s). Higher levels like S2 or T2 are not shown. Shaded curves on the left indicate a Boltzmann-like distribution of the rovibrational sublevels. **b)** Absorption $\alpha(\lambda)$ and fluorescence $f(\lambda)$ spectra of rhodamine 6G as a function of the optical wavelength λ in arbitrary linear units. Typical pump laser wavelength λ_p, cavity cutoff wavelength (e.g. $\lambda_c = 587\,\text{nm}$) and zero phonon line λ_{ZPL} are shown. The small subspectrum around 550 nm indicates a typical cavity emission spectrum for comparison. **c)** Spectral temperature of rhodamine 6G calculated from spectra in b).

and vibrational ("rovibronic") degrees of freedom inside the molecule. Their excitation energies form a quasi continuous substructure in each electronic state, which are occupied following Boltzmann statistics. Consequently, the transition energy is not a homogeneously broadened narrow spectral line but instead one observes an absorption spectrum $\alpha(\lambda)$ ranging over about 100 nm as shown in Fig. 2.1b. Accordingly, when the electron spontaneously decays back to S_0, the emitted fluorescence shows a broad spectral distribution $f(\lambda)$ as attributed to the many decay channels. Due to the symmetry of the internal density of states, $\alpha(\lambda)$ and $f(\lambda)$ are to good approximation their corresponding mirror image around the wavelength λ_{ZPL} given by the zero-phonon line, which denotes the transition wavelength between the lowest sublevel of S_0 and S_1 (black bars).

The Boltzmann-distributed occupation of the rovibronic substructure introduces thermodynamics to the discussion. Upon excitation of the dye by a monochromatic source with a photon energy differing from the zero-phonon line, the resulting sublevel occupation in the S_1 strongly differs from a thermal distribution. However, via internal conversion processes, excess energy is dissipated and/or energy deficits are compensates for via the thermal energy of the medium on the 1 ps timescale. This is much faster than spontaneous emission processes in this system, which in the case of rhodamine 6G dissolved in methanol have a time constant of [1] [72–74]

$$\tau_{\text{spont,R6G}} = 4.0(1)\,\text{ns} \approx 1/250\,\text{MHz} \quad . \tag{2.1}$$

The emission spectrum is hence independent of the initially exciting photon since the sublevels equilibrate fast enough to prepare quasi constant fluorescence conditions prior to spontaneous photon emission ("Kasha's rule" [75]).

2.1.2 Spectral Temperature

The sublevel occupation of the angular momentum states is assumed to be Boltzmann-like after sufficiently many internal conversion processes. Absorbance $\alpha(\omega)$ and spectral fluorescence

[1] The given uncertainty is an estimated scattering of published values. The actual lifetime always depends on external parameters such as solvent, molarity or temperature and is eventually biased by corresponding measurement resolution. Measurements in ref. [72] suggest that the here used solvent ethylene glycol and placement of the dye in a high-finesse resonator result in a slightly shorter spontaneous lifetime of around 3.70(3) ns. However, the above given value is used in further studies for consistency reasons as the impact is rather minor.

energy density $f(\omega)$ in free space are then connected via the Boltzmann factor

$$\frac{f(\omega)}{\alpha(\omega)} \propto \omega^3 \exp\left(-\frac{\hbar(\omega-\omega_{\mathrm{ZPL}})}{k_{\mathrm{B}}T}\right) \tag{2.2}$$

which is the Kennard-Stepanov or McCumber relation [76–81]. The spectral properties of every fluorophore deviate from this idealized assumption, similar to that no material has the properties of an ideal black body. As a figure of merrit one defines a spectral temperature as

$$T_{\mathrm{spec}}(\omega) = \frac{\hbar}{k_{\mathrm{B}}}\left[\frac{\partial}{\partial\omega}\log\left(\frac{\alpha(\omega)}{f(\omega)}\omega^3\right)\right]^{-1} \tag{2.3}$$

where $\alpha(\omega)$ and $f(\omega)$ are given in arbitrary dimensionless units as any prefactor will vanish by the derivative of the logarithm [82, 83]. A photon gas coupled to the given medium will then acquire a spectral distribution determined by T_{spec}, see sec. 2.5. The spectral temperature of rhodamine 6G, calculated from the spectra, is shown in Fig. 2.1c. In the experimentally relevant range of 550 nm to 600 nm one finds a roughly uniform spectral temperature close to the ambient temperature $T \approx 300\,\mathrm{K}$. Therefore, if not stated otherwise, both are treated equally in the following.

2.1.3 Quantum Yield and Photobleaching

So far, only a closed photon absorption and emission cycle has been discussed. However, experimentally one finds that an electronically excited electron emits on average less than one photon per decay back to S_0. As shown in Fig. 2.1a there are additional energy levels and transition processes inherent to most fluorophores which enable closed transition loops that do not only include photon emission. For our experiment, where rhodamine 6G is solved in ethylene glycol one finds for the quantum yield, which represents the average number of emitted photons per absorbed photons, that

$$\eta_{\mathrm{R6G}} \approx 95\,\% \tag{2.4}$$

is close to unity [84, 85]. The radiationless 5 % are usually dissipated as heat into the dye solution via various processes. A prominent example is the non-radiative decay from S_1 to S_0 as it can happen by collisions with fluorescence quenchers (e.g. oxygen) diffusing in the solvent [86]. Another process is the transition to a spin triplet state (e.g. S_1 to T_1) which is dipole forbidden but can nevertheless happen due to spin orbit coupling of the angular momenta of heavier nuclei in the molecule to the excited electron with a typical probability of order $P_{\mathrm{isc}} \approx 10^{-6}$ per absorbed photon. Since the transition back to S_0 is also dipole forbidden the lifetime of this state is usually in the millisecond regime. Although the final decay into the ground state would be accompanied by red shifted photon emission, the decay is usually completely quenched by the above mentioned processes due to the long lifetime and hence phosphorescence is suppressed. Due to the vanishing probability of this process, its effect on the numeric value of the quantum yield seems negligible, but is nevertheless highly relevant in a different matter: during the lifetime of a triplet state, other molecules may undergo several absorption and fluorescence cycles and ultimately also end up in the T_1 state when permanently being exposed to incident light. Hence, a significant fraction of dye molecules appear invisible which effectively reduces the number of absorbing dye molecules. Another issue is that dye molecules can be permanently desactivated via photochemical reactions while being electronically excited [87]. For instance they can form irreversible covalent modifications induced by environmental components, also caused by e.g. oxygen. The consequence is that during operation of the experiment, the dye solution bleaches over time scaling with the number of absorbed photons.

Formally, all non-radiative decay channels can be summarized to occur at a rate Γ_{nr}, which competes with the fluorescence rate Γ_r. The quantum yield η can then be expressed as the ratio of the fluorescence rate over the total decay rate via

$$\Gamma_{21} = \Gamma_r + \Gamma_{nr} = 1/\tau_{spont} \tag{2.5}$$

$$\eta = \frac{\Gamma_r}{\Gamma_r + \Gamma_{nr}} \quad . \tag{2.6}$$

For the studies presented in chapter 3 we will formally treat fluorescence of dye molecules into modes not confined by the cavity as a quenching process.

2.2 High-Finesse Optical Microcavity

To realize sufficiently long interaction times of the photon gas with the dye medium, both are confined inside a high finesse resonator. It consists of two opposing mirrors, usually separated by a distance of around one micrometer (hence often referred to as "microcavity") as illustrated in Fig. 1.1a. At least one of the mirror surfaces needs to be curved or show some other type of concave topography to trap photons as known from the stability criterion of laser resonators [88], see also sec. 2.3. With a maximum reflectance of order $R \approx 99.998\,\%$ the cavity finesse reaches values of up to $\mathcal{F} = \pi\sqrt{R}/(1-R) \approx 150\,000$. To give a more intuitive quantity, a photon will undergo on average up to $\bar{N}_{round} = \mathcal{F}/2\pi \approx 25\,000$ round trips before it leaves the resonator via mirror transmission. Due to the short cavity length, the maximum storage time is of order

$$\tau_{cav} = \bar{N}_{round}\frac{2D_0}{\tilde{c}} \tag{2.7}$$

$$= \frac{\mathcal{F}}{2\pi}\frac{7\lambda_c}{2c} \tag{2.8}$$

$$\approx 250\,\text{ps} \tag{2.9}$$

where D_0 is the mirror separation distance, $\tilde{c} = c_0/\tilde{n}$ the speed of light in a medium with refractive index $\tilde{n}$ and $\lambda_c \approx 580\,\text{nm}$ is a typical cutoff wavelength in the experiment. Those short storage times are in competition with the usually even faster interactions with the present dye molecules. In chapter 3 the dye concentration is systematically varied to probe the effect of reabsorption time versus cavity storage time. The mirror spacing of $D_0 = q\lambda_c/2\tilde{n} \approx 1.5\,\mu\text{m}$ causes a free spectral range of

$$\Delta\nu_{FSR} = \tilde{c}/2D_0 = \tilde{c}/7\lambda_c \tag{2.10}$$

$$\approx 70\,\text{THz} \tag{2.11}$$

$$\gg k_B T/2\pi\hbar \approx 6\,\text{THz} \tag{2.12}$$

$$\Delta\lambda_{FSR}(580\,\text{nm}) \approx 80\,\text{nm} \tag{2.13}$$

which is sufficient to push neighboring longitudinal modes out of the dye emission bandwidth (see Fig. 2.1) and prevents thermal excitation, implicating two dimensional behavior as the longitudinal degree of freedom is frozen out.

2.2.1 Mirror Reflection Characteristics

Aside from the peak reflectance of the cavity mirrors, its wavelength and angular dependence is of great significance for the photon gas trapping as highly excited resonator modes propagate at steep angles along the optical axis, see sec. 2.3.3. High reflection values require the use of dielectric mirrors instead of conventional metallic coatings such as silver or aluminum. Here,

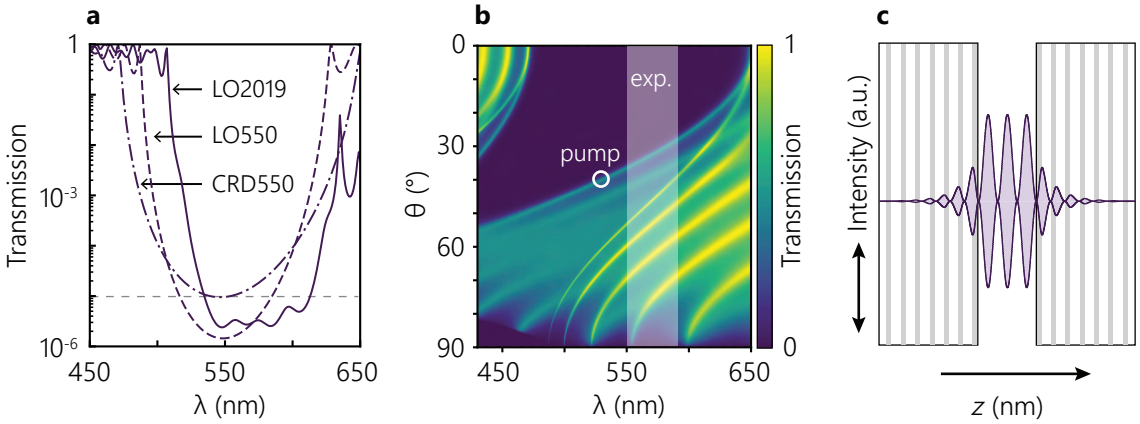

Fig. 2.2: Cavity mirror properties. **a)** Transmission profiles for various mirror types under normal incidence in ethylene glycol ($\tilde{n} \approx 1.44$), calculated with the formalism in sec. A.1. Gray dashed line at a transmission of 10^{-5} roughly indicates the absorption/scattering limit of the coating. **b)** Calculated mirror transmission profile for different incidence angles of the CRD550 mirror in ethylene glycol. Experimentally relevant region is marked as shaded area. The white circle marks the experimental pump beam parameters ($\lambda_p = 532\,\text{nm}, \theta_p \approx 42^\circ$). **c)** Penetration of the optical field into the layered mirror medium. Squared field amplitude $|E(z)|^2$ is mirrored around the zero line for better visibility. Alternating layers are shown as white/gray.

alternating media are layered on top of each other such that constructive interference of many partial Fresnel reflections results in a total reflection coefficient close to unity as compared to a single strong Fresnel reflection on a metal surface, which usually does not significantly exceed $\tilde{R} \approx 99\,\%$. Bragg mirrors (layers with optical thickness $\lambda/4$) with suited center wavelength can often be ordered from stock supply whereas some applications require more complex coatings that are typically designed in cooperation with a supplier. Despite the in principle arbitrary low transmission of the dielectric coating (here going down to $T \approx 10^{-6}$), the reflectance for visible light is usually capped around 99.9985 % in air due to residual scattering and absorption losses in the used materials. However, high reflection often goes along with strong dispersion as seen in Fig. 2.2a where three calculated transmission profiles of the used mirror coatings are shown, all for a surrounding ethylene glycol medium with refractive index $\tilde{n}(\lambda = 580\,\text{nm}) \approx 1.44$. The coating labels like "CRD550" usually contain the supplier name (here: Cavity Ringdown Optics) and in this case the center wavelength of the stop band or in the case of "LO2019" it stands for a coating run by the "Laseroptik GmbH" company ordered in 2019. An extensive description of the involved calculations can be found in sec. A.1.1. The reflection bandwidth of the mirrors is around 100 nm and comparable to the dye spectra. Fig. 2.2b shows the full angular dependence of the transmission profile. The stop band shifts to shorter wavelengths with increasing angle of incidence θ. At $\theta > 20^\circ$ the mirror reflectivity is already significantly lower than the $\theta = 0^\circ$ regime and for $\theta > 45^\circ$ they have almost completely lost their reflectivity in the experimentally relevant spectral region indicated by a white circle in the figure. This behavior depends on the involved materials and the polarization of the light. Conversely, this property makes it possible to irradiate the dye medium inside the resonator ("pump") under high angles with only small minor reflection losses also marked in the figure.

2.2.2 Field Distribution on the optical Axis

The reflection of light on a dielectric layer stack does not occur directly at the stack surface but the electromagnetic field penetrates the medium. For the here used short cavity lengths of a few wavelengths this effect turns out to be quite significant. The effective number of half waves inside the dye medium was experimentally determined to be $q - q_0 = 7 - 4.68(17) = 2.32(17)$

via a pump light absorption measurement [82], where $q = 7$ is typically determined from the free spectral range of the resonator. A comparable value was obtained for the "CRD550" mirrors, i.e. not the ones used in the reference. The actual electric field distribution can be obtained by a numerical simulation (explained in sec. A.1) where the mirror separation was set to three half waves as shown in Fig. 2.2c. For wavelengths inside the stop band of the coating, the wave nodes are still roughly located on the mechanical mirror surface. From the energy density $\mathcal{W} \propto \tilde{n}|E(z)|^2$ one can compare the likelihood of finding a photon inside one mirror compared to that of a single half wave in the dye medium

$$\left(\int_{\text{mirror}} \tilde{n}(z)\,|E(z)|^2 \mathrm{d}z\right) \Big/ \left(\int_{\text{half wave}} \tilde{n}(z)\,|E(z)|^2 \mathrm{d}z\right) \approx 65\,\% \tag{2.14}$$

where the squared field amplitude has to be weighted by the local refractive index $\tilde{n}$. The results suggest that the time spent inside the mirror material would correspond to only 1.3 half waves inside the dye medium. For the presented thesis this is relevant as the calculated photon absorption rates inside the medium usually have to be scaled down by a reasonable factor with respect to the raw absorption time as a photon spends only part of its time inside the dye medium. However, experimentally one nevertheless observes agreement of the resonator eigenmodes with q inferred from the free spectral range (see sec. 4.4). This discrepancy can not be explained with this calculation, which mainly serves the purpose of giving an exemplary intensity distribution inside the cavity.

2.3 Eigenmodes of a Custom Shaped Optical Microcavity

In order to describe the time evolution of an electromagnetic field $\boldsymbol{a}(\boldsymbol{r}, t)$ in an optical resonator knowledge about the cavity eigenmodes is critical as they in many cases allow for an entire description of photon dynamics without the need of complicated wave mechanical computations. If the basis states are chosen as energy eigenstates, they allow for straightforward calculations of thermodynamic parameters. The solutions for a resonator with spherically curved mirrors are well known from laser resonators, but a general formalism shall be introduced here as required for the works with experimental box-like potentials, presented in chapter 4. For this purpose we look for stationary solutions of a field in the employed optical resonator, hence we separate the time dependence of a generic ansatz $\boldsymbol{a}(\boldsymbol{r}, t) = \boldsymbol{a}(\boldsymbol{r})\, e^{-\mathrm{i}\omega t}$ from its spatial part. Furthermore, we assume that our solution is a carrier wave traveling along the optical axis z which is slightly modulated by a complex envelope, hence we separate once more $\boldsymbol{a}(\boldsymbol{r}) = \boldsymbol{A}(\boldsymbol{r})\, e^{\mathrm{i}|\boldsymbol{k}|z}$. In ray optics, this is equivalent to a small angle θ between wave vector $\boldsymbol{k}$ and the z-axis. By inserting $\boldsymbol{a}(\boldsymbol{r})$ into Maxwell's equations one finds that $\boldsymbol{A}(\boldsymbol{r})$ has to fulfill the *paraxial* Helmholtz equation

$$2\mathrm{i}|\boldsymbol{k}|\, \partial_z \boldsymbol{A}(\boldsymbol{r}) = -\nabla_T^2 \boldsymbol{A}(\boldsymbol{r}) \tag{2.15}$$

where $\nabla_T^2 = \partial_x^2 + \partial_y^2$ is the transverse part of the Laplacian [69]. One can now make the paraxial transformation where time is given by the position on the optical axis, $z = \tilde{c}t$, restrict the spatial coordinates to $\boldsymbol{r} = (x, y)$ and finally replace the photon energy with the relativistic rest mass relation $E = \hbar\omega = \tilde{c}\hbar|\boldsymbol{k}| = m_{\text{ph}}\tilde{c}^2$. The substitutions reveal that the transverse part of the paraxial Helmholtz equation is formally equivalent to the Schrödinger equation of a free massive particle in two dimensions [89, 90] when the field vector $\boldsymbol{A}$ is replaced by the wave function ψ:

$$\mathrm{i}\hbar\, \partial_t \psi(\boldsymbol{r}, t) = -\frac{\hbar^2}{2m_{\text{ph}}} \nabla_T^2 \psi(\boldsymbol{r}, t) \quad . \tag{2.16}$$

So far this equation describes the dispersion of a wave packet in the absence of a confining potential, $V(\boldsymbol{r}) = 0$. Confined modes are experimentally realized by concave-shaped resonator mirrors which, as explained in the following, act as an attractive potential for paraxial rays.

We introduce the cavity as depicted in Fig. 2.3 consisting of one flat mirror and an opposing one with surface profile $\Delta D(x)$ at transverse position x, hence the mirrors are separated by a total distance of $D_0 - \Delta D(x)$. Without loss of generality the problem is reduced to one transverse dimension x. Consider a wave $\psi(x, z = 0)$ propagating from the left side towards the right mirror. It acquires a phase envelope during its free propagation that can be expressed by the time evolution operator $\hat{U}(z)$ derived by formal integration of (2.15) or (2.16). On the mirror surface the wave acquires an additional phase due to the slightly differing path lengths $\Delta\varphi = k\Delta D(x)$, represented by the operator $\hat{\Phi}(x)$. The process repeats on the return path where finally, as required for a standing wave, the wave $\psi(x, 2D_0)$ has to reproduce its initial configuration. After integration, the evolution operators look like

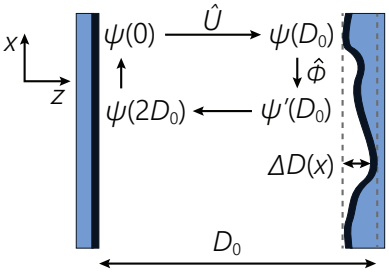

Fig. 2.3: Custom shaped cavity.

$$\hat{U}(z) = \exp\left(-\mathrm{i}\hbar \frac{z}{2m_{\mathrm{ph}}\tilde{c}}\,\partial_x^2\right) \tag{2.17}$$

$$\hat{\Phi}(x) = \exp(\mathrm{i}\,\Delta\varphi(x)) \tag{2.18}$$

$$= \exp(-\mathrm{i}k_z\,\Delta D(x)) \tag{2.19}$$

$$\psi(x, 2D_0) = \hat{U}(D_0)\,\hat{\Phi}^2(x)\,\hat{U}(D_0)\,\psi(x, 0) \tag{2.20}$$

$$\stackrel{!}{=} \psi(x, 0) \tag{2.21}$$

We see that the mirror surface has to compensate the free phase acquired during free propagation in order to obtain a stationary wave pattern. By splitting of $\hat{U}$ into $\exp(\mathrm{i}x) = \cos(x) + \mathrm{i}\sin(x)$, the imprinted phase of the final state with respect to the unperturbed one can be obtained via $\Delta\varphi = \arg(\psi) = \arctan(\mathrm{Im}(\psi)\,/\,\mathrm{Re}(\psi))$ as [91]

$$\Delta\varphi(x) = \arctan\left(\frac{\sin(d\,\partial_x^2)\,\psi(x,0)}{\cos(d\,\partial_x^2)\,\psi(x,0)}\right) \qquad \text{with} \qquad d \equiv \frac{\hbar D_0}{2m_{\mathrm{ph}}\tilde{c}} \quad . \tag{2.22}$$

For paraxial beams, the transverse phase changes much slower compared to longitudinal propagation, hence one can expand the expression for small $d\partial_x^2$ in first order which yields

$$\Delta\varphi(x) \simeq d\,\frac{\partial_x^2\psi(x, D_0)}{\psi(x, D_0)} \quad . \tag{2.23}$$

From the stationary single particle Schrödinger equation ($\partial_t\psi(x, D_0) \stackrel{!}{=} 0$) we know that the effect of a potential $V(x)$ onto the wave function has the form

$$\frac{\partial_x^2\psi(x,z)}{\psi(x,z)} = \frac{2m_{\mathrm{ph}}}{\hbar^2}V(x) \tag{2.24}$$

which we can plug into (2.23) and after a couple of already mentioned substitutions we arrive at

$$V(x) = m_{\mathrm{ph}}\tilde{c}^2\,\frac{\Delta D(x)}{D_0} \quad . \tag{2.25}$$

The full transverse equation of motion with $\boldsymbol{r} = (x, y)$ then reads

$$\mathrm{i}\hbar\,\partial_t\psi(\boldsymbol{r}, t) = \left(-\frac{\hbar^2}{2m_{\mathrm{ph}}}\,\nabla_T^2 + m_{\mathrm{ph}}\tilde{c}^2\,\frac{\Delta D(\boldsymbol{r})}{D_0}\right)\psi(\boldsymbol{r}, t) \quad . \tag{2.26}$$

The eigenstates of an arbitrary resonator are the stationary solutions of (2.26). The formal equivalence between the paraxial Helmholtz equation and the Schrödinger equation implies that the transverse motion of photons inside a concave resonator is equivalent to the one of massive particles in a potential, here determined by the mirror surface topography. In some cases a corresponding solution can be obtained analytically (sec. 2.3.1) while real world situations often require numerical solutions.

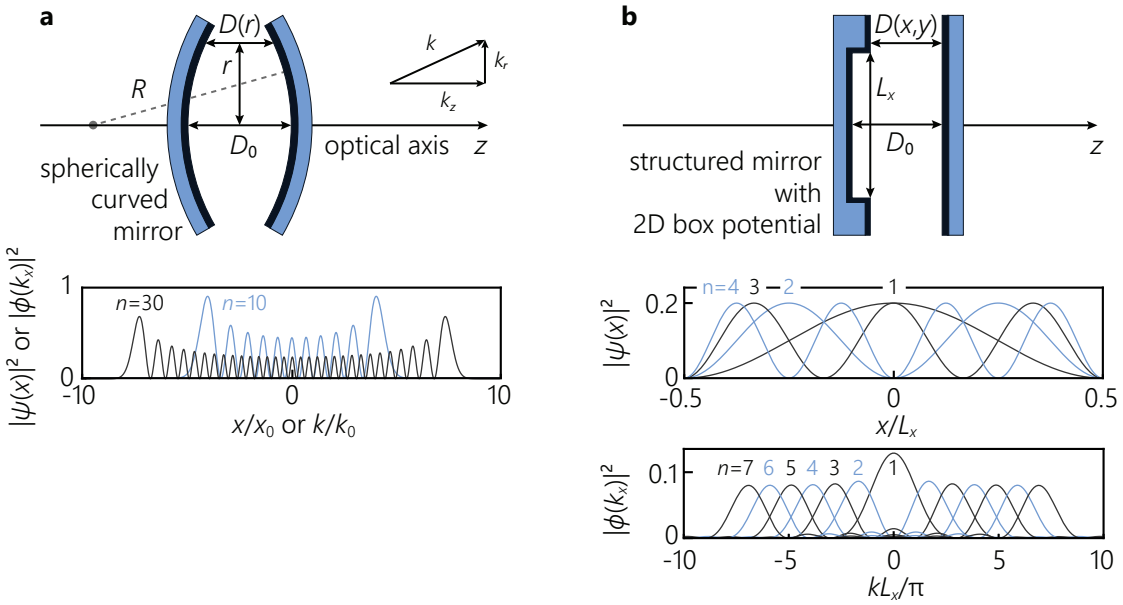

Fig. 2.4: Sketch of the two resonator geometries used in this thesis with exemplary spatial and momentum eigenfunctions $|\psi|^2$ and $|\phi(k)|^2$. **a)** Resonator consisting of two spherically curved mirrors separated by a distance D_0 on the optical axis. The probability densities are shown in arbitrary units. **b)** Resonator consisting of a plane and a structured mirror. The surfaces are always parallel but the separation $D(x, y)$ varies locally resulting in a box-shaped potential for the trapped light.

2.3.1 Analytic Examples: Harmonic and Box Potential

All measurements presented in this thesis work were carried out in either harmonic (spherically curved mirrors) or box-like potentials (microstructured mirror surface, see sec. 4.1), as illustrated in Fig. 2.4.

Harmonic Potential

If a resonator consists of two spherically curved mirrors with radii of curvature $\tilde{R}_1$ and $\tilde{R}_2$, they can be reduced to an effective radius of curvature via $2/\tilde{R} = 1/\tilde{R}_1 + 1/\tilde{R}_2$. The mirror separation $D(r) = D_0 - (\tilde{R}^2 - r^2)^{\frac{1}{2}}$ is radially symmetric and close to the optical axis can be approximated by a quadratic function. The potential thus has the form

$$V(r) = \frac{1}{2} m_{\mathrm{ph}} \Omega^2 r^2 \quad \text{where} \quad \Omega = \frac{\tilde{c}}{\sqrt{D_0 \, \tilde{R}/2}} \tag{2.27}$$

denotes the angular trapping frequency as in a harmonic oscillator potential. The solutions of the Schrödinger equation then read

$$\psi_n(x) = \frac{1}{\sqrt{\sqrt{\pi}\, x_0\, 2^n n!}} H_n\left(\frac{x}{x_0}\right) \exp\left(-\frac{1}{2}\frac{x^2}{x_0^2}\right) \qquad \text{with} \qquad n = 1, 2, 3, \ldots \tag{2.28}$$

$$\psi_{n_x,n_y}(x, y) = \psi_{n_x}(x) \cdot \psi_{n_y}(y) \tag{2.29}$$

where $H_n(x)$ are Hermite polynomials and $x_0 = \sqrt{\hbar/m_{\mathrm{ph}}\Omega}$ is the harmonic oscillator length [92]. The two-dimensional wave functions $\psi(x, y)$ correspond to equally spaced energy eigenvalues

$$E_{n_x,n_y} = E_{n_x} + E_{n_y} = \hbar\Omega(n_x + n_y + 1) \qquad \text{with} \qquad n_x, n_y = 0, 1, 2, \ldots \tag{2.30}$$

The degeneracy (number of states with same Energy E) in the two dimensional case is $g(E) = E/\hbar\Omega + 1$ due to the increasing possible combinations of n_x and n_y yielding the same energy.

The Hamiltonian is a symmetric function of x and p, hence the momentum space eigenfunctions are of identical shape

$$\phi_n(k) = \frac{(-\mathrm{i})^n}{\sqrt{\sqrt{\pi}\, k_0\, 2^n n!}}\, H_n\left(\frac{k}{k_0}\right)\, \exp\left(-\frac{1}{2}\frac{k^2}{k_0^2}\right) \tag{2.31}$$

with $k_0 = \sqrt{m_{\mathrm{ph}}\Omega/\hbar} = 1/x_0$, see Fig. 2.4a.

Box Potential

Next we consider a rectangular 2D box potential with side lengths $L_{x,y}$, infinitely high sharp edge walls with center at $x = y = 0$ where the wave factor k_x, k_y must obey the boundary condition $k_{x,y} = n_{x,y} \cdot \pi/L_{x,y}$. One finds

$$\psi_n(x) = \sqrt{\frac{2}{L_x}}\, \sin\left(k_x x + \frac{n\pi}{2}\right) \qquad \text{with} \qquad n = 1, 2, 3, \ldots \tag{2.32}$$

$$\psi_{n_x,n_y}(x, y) = \frac{2}{\sqrt{L_x L_y}}\, \sin\left(k_x x + \frac{n_x\pi}{2}\right)\, \sin\left(k_y y + \frac{n_y\pi}{2}\right) \tag{2.33}$$

where the phase term $n\pi/2$ shifts the wave nodes onto the end points of the box. Again, since x and y dimension are independent of each other, the two dimensional wave function is a simple product of the 1D solutions. The eigenenergies

$$E_{n_x,n_y} = \frac{\hbar^2|\boldsymbol{k}|^2}{2m_{\mathrm{ph}}} = \frac{\hbar^2\pi^2}{2m_{\mathrm{ph}}}\left(\frac{n_x^2}{L_x^2} + \frac{n_y^2}{L_y^2}\right) \qquad \text{with} \qquad n_{x,y} = 1, 2, 3, \ldots \tag{2.34}$$

scale quadratically with the mode numbers, which ultimately leads to an energy independent density of states in two dimensions, see sec. 2.4.2. Although the wave vector k_x in (2.32) has fixed values $\psi_n(x)$ is not an eigenstate of the momentum operator $\hat{p} = -\mathrm{i}\hbar\partial_x$, hence the momentum space wave functions are obtained via Fourier transform $\mathcal{F}$ and are expressed by

$$\phi_n(k_x) = (\mathcal{F}_x\psi_n(x))(k_x) = \frac{1}{\sqrt{2\pi}}\int_{-\infty}^{\infty}\psi_n(x)\, e^{-\mathrm{i}k_x x}\mathrm{d}x \tag{2.35}$$

$$= \mathrm{i}^{n+1}\sqrt{4n^2\pi L_x}\,\frac{\sin\left((k_x L_x + n\pi)/2\right)}{k_x^2 L_x^2 - \pi^2 n^2} \tag{2.36}$$

which for $n > 1$ resemble a broadened peak around $k_x = \pm n\pi/L$ after taking the absolute square, see Fig. 2.4b. The width is an artifact of the finite box size; the peaks becomes sharply defined for $L_x \to \infty$.

2.3.2 Numerically Solving the Schrödinger Equation

In many potential landscapes, analytical solutions of the Schrödinger equation can not be obtained. Those wave functions have to be computed numerically, see for example sec. 4.1.3 for an application. In our case, the potential $V(x, y)$ is typically known from mirror surface profiles. In one dimension x, $V(x)$ is given by an N-component vector

$$V(x) = \big(V(x_1), V(x_2), \ldots, V(x_N)\big)^{\mathrm{T}} \tag{2.37}$$

due to the finite, here equidistant, sampling of computers or measurement devices e.g. image pixels. As one is looking for a vector-like solution of $\psi = (\psi_{x_1}, \psi_{x_2}, \ldots, \psi_{x_N})^{\mathrm{T}}$ the Hamilton operator $\hat{\mathcal{H}} = \hat{T} + \hat{V}$ is a $N \times N$ matrix. Since the potential is already given in the correct basis,

it transforms to an operator as a diagonal matrix, $\hat{V} = \mathrm{diag}(V(x))$. The kinetic energy operator $\hat{T} = \hat{p}^2/2m$ contains a second derivative in space from the momentum operator $\hat{p} = -\mathrm{i}\hbar\partial_x$ which translates into a numeric operation known as the Laplace filter [93], that is (in one dimension) a convolution of the input vector with the kernel $(1, -2, 1)^{\mathrm{T}}$. The corresponding kinetic energy operator then reads

$$\hat{T}_{mn} = -\frac{\hbar^2}{2m}\left(\frac{N}{|x_{\mathrm{N}} - x_1|}\right)^2 (\delta_{m+1,n} - 2\delta_{m,n} + \delta_{m-1,n}) \tag{2.38}$$

where δ_{mn} is the Kronecker delta. The spatial sampling frequency $N/|x_{\mathrm{N}} - x_1|$ of $V(x)$ determines the maximum k-resolution of this method. The eigenfunctions inside the investigated potential are then given by the eigenvectors of $\hat{\mathcal{H}}$, whereas the eigenvalues are the associated eigenenergies.

This algorithm is already implemented in a package for the Python programming language [94] which is here used for numerical solving. The formalism can be upscaled to the here relevant two dimensional problems, but the computation time scales quadratically with the sample count N inefficient. The potential landscapes investigated in this thesis possess sufficient symmetry to separate and solve the problem in each individual dimension, hence the full wave function is then constructed via $\psi(x, y) = \psi(x)\psi(y)$ with corresponding eigenenergy $E_{xy} = E_x + E_y$.

2.3.3 Dispersion Relation

Although the wave functions already hold the entire phase space information of a particle in that mode, it is often useful to approach the propagation characteristics in a ray-like picture. The photon wave vector of a paraxial light ray $\boldsymbol{k}$ can be decomposed into a longitudinal k_z and a transverse component $k_r^2 = k_x^2 + k_y^2$ with respect to the optical axis z as illustrated in Fig. 2.4. The corresponding dispersion relation in a medium with refractive index $\tilde{n}$ (and hence $\tilde{c} = c_0/\tilde{n}$) then reads

$$E(\boldsymbol{k}) = \tilde{c}\hbar\,|\boldsymbol{k}| = \hbar\tilde{c}\,\sqrt{k_z^2 + k_r^2} \tag{2.39}$$

$$\simeq \tilde{c}\hbar(k_z + k_r^2/2k_z) \quad . \tag{2.40}$$

Regardless of the field penetration into the dielectric cavity mirror (see sec. 2.2.2), the z-dimension behaves box-like. The boundary conditions imprinted onto the field by the cavity mirrors are wave nodes located on the mirror surface, see Fig 2.2.

$$k_z \stackrel{!}{=} q \cdot \frac{\pi}{D_0} \qquad \text{with} \qquad q = 1, 2, 3, \ldots \tag{2.41}$$

Due to the short cavity length and the large wavelength spacing of neighboring modes of about 80 nm we consider a fixed longitudinal wave number q and hence a fixed k_z as only one longitudinal mode with its transverse substructure reasonably overlaps with dye spectra and mirror reflection band (Fig. 1.1). The resulting offset of $\tilde{c}\hbar k_z = m_{\mathrm{ph}}\tilde{c}^2$ serves as a low energy cutoff inside a resonator leaving the excitation energy of the eigenmodes entirely to be stored inside the transverse momentum components. Eigenstates with energy E_i are not necessarily eigenfunctions of the momentum operator, hence the wave functions yield a probability distribution of momenta. Nevertheless, the root mean square $\int_{-\infty}^{\infty} k_r^2|\phi(k_r)|^2\,\mathrm{d}k_r$ reveals the average (squared) transverse vector of the modes as $\bar{k}_{r,i}^2 = 2m_{\mathrm{ph}}E_i/\hbar^2 = 2m_{\mathrm{ph}}(n_x + n_y)\Omega/\hbar$ for the harmonic oscillator or $\hbar k_{r,i}^2 = (n_x^2 + n_y)^2\pi^2/L^2$ for a box potential, which fulfills the classical energy-momentum relation. As shown in Fig. 2.4, the momentum wave function in a box strongly accumulates around the $\pm\hbar(k_x, k_y)$ peaks, while there are still large contributions in the low-k part in the harmonic oscillator. Physically this can be interpreted as such that a particle in a box propagates at constant speed and bouncing against the walls flips its direction. In the harmonic case, potential

and kinetic energy is periodically interchanged and hence there are non-negligible contributions for all momentum amplitudes $\hbar k_i < \sqrt{2m_{\mathrm{ph}}E_i}$.

The propagation angle θ of a light ray with respect to the optical axis is obtained via

$$\theta = \arctan\left(k_r/k_z\right) \quad . \tag{2.42}$$

The (maximum) divergence angle of a mode is approximately given by the ratio of transverse and longitudinal momentum at the potential minimum where the entire eigenenergy is stored in its kinetic component

$$\theta_i = \arctan\left(\frac{\sqrt{2m_{\mathrm{ph}}E_i}}{\hbar k_z}\right) = \arctan\left(\sqrt{\frac{2E_i}{m_{\mathrm{ph}}\tilde{c}^2}}\right) \tag{2.43}$$

which can be used to probe the setup for its capability to properly image high order modes, see for example sec. 3.4. However, refraction occurs at the interface between the dye, mirror glass substrate and the surrounding air, which bends the light away from the optical axis and the effective propagation angle increases by another factor of the dye medium refractive index $\tilde{n}$

$$\theta_{i,\mathrm{air}} = \arcsin(\tilde{n}\sin(\theta_i)) \tag{2.44}$$

$$\simeq \tilde{n}\theta_i \tag{2.45}$$

where the last step is valid for small θ. The refractive index of the substrate does indeed not matter here. Common objective lenses in our setups have a numerical aperture of NA $= 0.42$ and are thus capable to detect divergence angles of up to $\theta_{i,\mathrm{air}} < \arcsin(\mathrm{NA}) \approx 25^\circ$ which corresponds to transverse energies of about $3.5\,k_{\mathrm{B}}T$ or a wavelength range of $\Delta\lambda \approx 25\,\mathrm{nm}$ in our spectral working regime. A higher NA can be achieved as described in sec. 3.4.

2.4 Statistical Physics of the Photon Gas

The system eigenstates and -energies allow for a quantitative description of the low temperature behavior of the photon gas, especially regarding Bose-Einstein condensation (see sec. 1.1.1). In the following, all eigenenergies are given relative to the system ground state energy $E_0 = m_{\mathrm{ph}}\tilde{c}^2$. In other words, we solely consider the transverse energies $E_{n_x n_y}$.

2.4.1 Harmonic Potential

The excited state energies in the two dimensional harmonic oscillator are

$$E_{n_x,n_y} = \hbar\Omega(n_x + n_y) \tag{2.46}$$

if one also absorbs the zero point energy of $\hbar\Omega$ in the global energy offset. One finds that every energy level is associated with $\bar{g}(E) = E/\hbar\Omega + 1$ eigenfunctions, which we identify with a degeneracy that scales linear with energy. This scaling ($\alpha = 2$, see sec. 1.1.1) enables Bose-Einstein condensation in such a system [39]. We can calculate the critical particle number via (1.6) since the trapping frequency here usually fulfills the condition $\hbar\Omega \ll k_{\mathrm{B}}T$. At threshold we assume the ground state occupation still of order 1 and neglect it in the total particle number. For $\mu = 0$ we get the critical particle number

$$N_{\mathrm{c}} = 2\int_0^\infty \frac{E/\hbar\Omega + 1}{\exp(E/k_{\mathrm{B}}T) - 1}\,\mathrm{d}E \tag{2.47}$$

$$\approx \frac{\pi^2}{3}\left(\frac{k_{\mathrm{B}}T}{\hbar\Omega}\right)^2 \tag{2.48}$$

where a factor of 2 accounts for the polarization degeneracy of the photon gas and the +1 term in the numerator was omitted since on average $E/\hbar\Omega \gg 1$. The result is equivalent to a critical temperature of

$$T_\mathrm{c} = \frac{\sqrt{3}}{\pi}\frac{\hbar\Omega}{k_\mathrm{B}}\sqrt{N}, \tag{2.49}$$

an expression, which is more commonly used in ultracold quantum gas experiments. In our case, the phase transition is reached via introducing more particles to the system, which then raises the critical temperature to room temperature. Beyond $N > N_\mathrm{c}$, the total particle number is the sum over the occupation of the saturated excited states and the ground state, which absorbs every additional particle. For our trapping frequency $\Omega \approx 2\pi \times 40\,\mathrm{GHz}$ caused by the mirror curvature radius $\tilde{R} = 1\,\mathrm{m}$, we obtain a critical particle number of $N_\mathrm{c} \approx 82\,000$. The described behavior is commonly observed in our system, see [63].

2.4.2 Box Potential

Since the measurements presented in chapter 4 are exclusively performed with unity aspect ratio box potentials ($L \equiv L_x = L_y$), the excitable energies (2.34) are given by

$$E_{n_x n_y} = \frac{\pi^2\hbar^2}{2mL^2}(n_x^2 + n_y^2) \qquad \text{with} \qquad n_{x,y} = 1, 2, \ldots \quad . \tag{2.50}$$

Assuming boxes of sufficient size such that $\pi^2\hbar^2/2mL^2 \ll k_\mathrm{B}T$, the density of states is obtained as the number of allowed eigenstates N in the infinitesimal interval $E + \mathrm{d}E$. Every state occupies a k-space area of $A_k = (\Delta k)^2 = \pi^2/L^2$, following from the spacing $\Delta k = \pi/L$ implied by the box boundary conditions. As we exclusively use positive n_x, n_y, we integrate over only one quadrant with area $A = \pi k^2/4$. One gets

$$\tilde{g}(E) = \frac{\partial N}{\partial E} = \frac{\partial}{\partial E}\frac{A}{A_k} = \frac{\partial}{\partial E}\frac{\pi k^2/4}{\pi^2/L^2} \tag{2.51}$$

$$= \frac{mL^2}{2\pi\hbar^2} = \frac{1}{k_\mathrm{B}T}\frac{V}{\lambda_\mathrm{th}^2} = \text{const.} \tag{2.52}$$

where in the last step, the energy-momentum relation $k^2 = 2mE/\hbar^2$ was inserted. We find the degeneracy to be independent of the energy ($\alpha = 1$, cf. sec. 1.1.1). We know from (1.6) that condensation in the infinite system $L \to \infty$ should be suppressed at finite temperatures as the critical particle number diverges, which would be equivalent to a vanishing trapping frequency Ω in the harmonic oscillator. A comparison of the thermodynamic behavior of a harmonically trapped gas and a finite size homogeneously trapped gas is shown in Fig. 2.5a. The saturation behavior of the excited modes N_exc in a harmonic oscillator ($\Omega = 2\pi \times 40\,\mathrm{GHz}$) and a box potential ($L = 100\,\mu\mathrm{m}$) is visible upon increasing the total particle number N. In the harmonic oscillator, where the condition of criticality is robust in the thermodynamic limit $N, V \to \infty$, one sees a sharp saturation of the excited modes at the onset of condensation. In the box, however, the saturation happens slowly without a discontinuity. This behavior already hints at the absence of a phase transition in the thermodynamic limit, also due to the fact, that for $N, V \to \infty$ the critical particle number diverges and N_exc never saturates.

However, the ratio of ground state and excited state particles can take arbitrary large values. While thermal fluctuations destroy long-range order in the infinite system [95] one finds that condensation in the finite system is possible when the coherence length ξ exceeds the system size [51, 96]. The condition $L = \xi$ allows for to find an analytic expression for the critical particle number N_c. In the quantum degenerate limit, the largest contributions to the density profile and

the coherence of the system stem from the energetically low-lying states with wave number k, therefore one can expand the Bose-Einstein distribution $n(\boldsymbol{k})$ to first order

$$n(\boldsymbol{k}) = \left[\exp\left(\frac{\hbar^2|\boldsymbol{k}|^2/2m - \mu_0}{k_\mathrm{B}T}\right) - 1\right]^{-1} \tag{2.53}$$

$$\simeq \left[\frac{1}{k_\mathrm{B}T}\left(\frac{\pi^2\hbar^2}{2mL^2}(n_x^2 + n_y^2 - 2) - \mu\right)\right]^{-1} \tag{2.54}$$

$$\equiv \frac{4\pi}{\lambda_\mathrm{th}^2}\frac{1}{|\boldsymbol{k}|^2 + k_\mathrm{c}^2} \tag{2.55}$$

$$\text{with} \quad k_\mathrm{c} \equiv -\frac{2m}{\hbar^2}\mu - \frac{2\pi}{L^2} \tag{2.56}$$

where the -2 term in (2.54) is manually introduced to set an appropriate zero point energy. From arguments like in sec. 1.2.1 we find the coherence length in the Bose gas via a Fourier transform of the Lorentzian shaped $n(\boldsymbol{k})$ which yields an exponential decay:

$$g^{(1)}(r) \propto \exp(-k_\mathrm{c}r) \tag{2.57}$$

$$\equiv \exp(-r/\xi_\mathrm{c}) \tag{2.58}$$

We now require the coherence length at criticality $\xi_\mathrm{c} = k_\mathrm{c}^{-1}$ to reach the system size L, which yields an expression for the corresponding chemical potential μ_c

$$\xi_\mathrm{c} \stackrel{!}{=} L \tag{2.59}$$

$$\mu_\mathrm{c} = -k_\mathrm{B}T\,\frac{\lambda_\mathrm{th}^2}{L^2}\frac{1 + 2\pi^2}{4\pi} \quad . \tag{2.60}$$

After insertion into (1.35) we get

$$N_\mathrm{c,box}(L) = -\frac{L^2}{\lambda_\mathrm{th}^2}\log\left(1 - \exp\left(-\frac{\lambda_\mathrm{th}^2}{L^2}\frac{1 + 2\pi^2}{4\pi}\right)\right) \tag{2.61}$$

$$\simeq \frac{L^2}{\lambda_\mathrm{th}^2}\log\left(\frac{L^2}{\lambda_\mathrm{th}^2}\frac{4\pi}{1 + 2\pi^2}\right) \tag{2.62}$$

which for $L \gg \lambda_\mathrm{th}$ simplifies to an $L^2\log(L)$ scaling. We see that N_c scales logarithmically faster than the area L^2, hinting at the absence of condensation in arbitrary large systems. From $\lambda_\mathrm{th}^2 \propto T^{-1}$ follows the relation

$$\frac{N_\mathrm{c}}{N} = \frac{T}{T_\mathrm{c}}\frac{\log(T)}{\log(T_\mathrm{c})} \simeq \frac{T}{T_\mathrm{c}} \tag{2.63}$$

where the logarithmic correction is of order unity. As we work at a constant temperature $T \approx 300\,\mathrm{K}$, we will resort to expression based on N in further investigations such as the caloric properties of the gas along the critical point. The smooth onset of the saturation of the excited particle states suggests that we expect the caloric properties of the two dimensional homogeneously trapped gas are also smooth across the phase transition. Following sec. 1.3 we extract the internal energy U from the grand potential $\mathcal{G}$ via

$$U = \mathcal{G} - T\frac{\partial\mathcal{G}}{\partial T} - \mu\frac{\partial\mathcal{G}}{\partial\mu} \tag{2.64}$$

$$= \sum_i E_i\,\bar{n}_{\mu,T}(E_i) \quad \simeq \quad \int_0^\infty E\,n_{\mu,T}(E)\,\mathrm{d}E \tag{2.65}$$

$$= k_\mathrm{B}T\frac{V}{\lambda_\mathrm{th}^2}\,\mathrm{Li}_2\left(e^{\mu/k_\mathrm{B}T}\right) \tag{2.66}$$

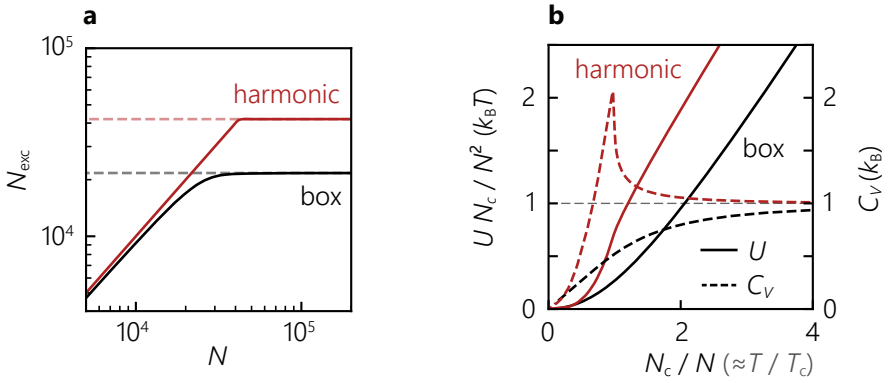

Fig. 2.5: a) Saturation of excited modes in a harmonically trapped 2D Bose gas compared to the homogeneous case in a finite size box. While the harmonically trapped gas shows a sharply damped saturation of excited modes corresponding to a well-defined phase transition, the photon gas in a box undergoes a smooth continuous transition. **b)** Internal energy and specific heat for both cases. The smooth crossover of C_V and U for a box potential hint at the absence of a second-order phase transition.

which corresponds to an energy weighted summation over the single particle occupations. As we have chosen to set the ground state energy as the zero point, its contribution vanishes. From the internal energy one can compute the isochoric (constant volume) heat capacity

$$C_V = \left(\frac{\partial U}{\partial T}\right)_V \tag{2.67}$$

$$\frac{C_V}{Nk_\mathrm{B}} = \frac{\partial(U\,/\,(Nk_\mathrm{B}T_\mathrm{c}))}{\partial(T/T_\mathrm{c})} \tag{2.68}$$

$$\simeq \frac{\partial(U\,N_\mathrm{c}/(N^2k_\mathrm{B}T))}{\partial(N_\mathrm{c}/N)} \quad . \tag{2.69}$$

As the expression $N(\mu)$, see (1.35), can not be solved for μ in all cases, the derivative has to be taken numerically. In the classical limit $|\mu| \gg k_\mathrm{B}T$ every photon contributes $(f/2)\,k_\mathrm{B} = 1\,k_\mathrm{B}$ to the heat capacity as understood from its $f = 2$ degrees of freedom while the function approaches zero for $\mu \to 0$ since the (macroscopically occupied) ground state does not contribute transverse internal energy to the system.

Internal energy and specific heat for a harmonic trap as well as for a box trap are shown in Fig. 2.5b. While the harmonically trapped gas experiences a cusp-like discontinuity (similar to the lambda transition in superfluids [61, 97]) at threshold, the uniform gas does not show such a discontinuity, hinting at the absence of a phase transition according to the Ehrenfest classification [42]. Note that in Fig. 2.5, the quantities of the harmonically trapped gas have been divided by 2 for better comparison. According measurements for the box trap are presented in sec. 4.5.

2.5 Grand Canonical Rate Equation Model

We introduce a rate equation model aiming to describe the spatial and spectral photon distribution inside the resonator. In the dye-cavity, electronic excitations of the dye molecules are interconverted to photonic excitations of resonator modes. The dye molecules in a liquid solution exhibit frequent collisions with solvent molecules and rapid molecular dipole dephasing (much faster than the Rabi frequency) that destroys any coherence between photons and molecules, preventing the formation of exciton-polaritons [41]. This weak-coupling regime allows for a great reduction of the problem complexity via the diagonal approximation, i.e. neglecting all (off-diagonal) coherence terms in the density matrix. A rate equation model of this kind has

proven itself as a simple yet powerful method for the modeling of spatial and temporal photon distributions [64, 98–101]. Useful theoretical descriptions can be found in [102–105]. In this thesis, the existing models from the references was extended by explicitly taking a variable photon loss into account as it plays a crucial role when quantitatively investigating the photon phase space density inside the cavity under real world conditions.

Starting from Einstein's rate equations we write the rates of absorption and emission per volume $R_{12,21}$ dependent on excited and ground state molecule density $\rho_{\uparrow,\downarrow}$, respectively, the spectral energy density $u_i(x)$ of the cavity modes with index i and the Einstein coefficients of stimulated absorption and emission $B_{12,21}$, respectively. We reduce $u_i(x,\omega) = \hbar\omega_i|\psi_i(x)|^2\delta(\omega-\omega_i)$ to $u_i(x) \equiv \int_0^\infty u_i(x,\omega)\,\mathrm{d}\omega = \hbar\omega_i|\psi_i(x)|^2$. From the Einstein model we write the absorption and emission rates $R_{12,21}$ per volume for each individual mode at position x as

$$R_{12,i}(x) = B_{12}(\omega_i)\,u_i(x)\,\rho_\downarrow(x)\,n_i \tag{2.70a}$$

$$R_{21,i}(x) = B_{21}(\omega_i)\,u_i(x)\,\rho_\uparrow(x)\,(n_i+1) \quad . \tag{2.70b}$$

The additional +1 term represents spontaneous emission, which equals the stimulated emission rate caused by a single photon [106]. After integration of (2.70a) and (2.70b) we introduce external pump and loss terms and arrives at expressions for individual cavity modes and local molecule excitation numbers

$$\partial_t\, n_i = \int_V \Big[B_{21}(\omega_i)\,u_i(x)\,\rho_\uparrow(x)\,(n_i+1) - B_{12}(\omega_i)\,u_i(x)\,\rho_\downarrow(x)\,n_i\Big]\mathrm{d}x - \Gamma_{\mathrm{cav},i}n_i \tag{2.71a}$$

$$\begin{aligned}\partial_t\,\rho_\uparrow(x) = {} & \sum_i \Big[B_{12}(\omega_i)\,u_i(x)\,\rho_\downarrow(x)\,n_i - B_{21}(\omega_i)\,u_i(x)\,\rho_\uparrow(x)\,(n_i+1)\Big] \\ & - \Gamma_{\mathrm{iso}}\,\rho_\uparrow(x) + R_\mathrm{p}(x)\end{aligned} \tag{2.71b}$$

$$\partial_t\,\rho_\downarrow(x) \overset{!}{=} -\partial_t\,\rho_\uparrow(x) \tag{2.71c}$$

where we integrate over the complete resonator volume V and sum over all cavity modes i as n_i is a global and $\rho_\uparrow$ is a local value. The terms containing B_{12}, B_{21} in (2.71a) and (2.71b) correspond to the same physical process. The decay term $\Gamma_{\mathrm{cav},i}$ accounts for transmission of trapped photons through the cavity mirrors while Γ_{iso} contains the (isotropic) spontaneous decay rates into unconfined modes, see Fig. 2.6. Photons in those free space modes are not a part of the paraxial light field and are treated as a loss channel. The effect of finite quantum yield $\eta < 1$ is included in Γ_{iso} due to its formal equivalence. $R_\mathrm{p}(x)$ is the local external pump excitation rate, which can be tuned in the experiment.

The entire expressions for n_i and $\rho_{\uparrow,\downarrow}$ typically have to be solved numerically. Since the simulation of the entire multimode system is computationally very costly, some approximations can be made to give further physical understanding and numerical simplifications as explained in the following.

2.5.1 Limit: Isolated Cavity

To discuss the steady state intracavity photon distributions n_i in the absence of photonic and molecular losses we for now assume $\Gamma_{\mathrm{iso}} = \Gamma_{\mathrm{cav}} = R_\mathrm{p} = 0$ and perfect quantum yield $\eta = 1$. The only remaining process is the photochemical reaction $\gamma + \downarrow \leftrightharpoons \uparrow$, connecting an excitation ($\uparrow$) and a ground state molecule ($\downarrow$) via a photon γ. The resulting conservation of the total excitation number requires the chemical potentials before and after a conversion process to be equal, $\mu_\gamma + \mu_\downarrow = \mu_\uparrow$. It it useful here to reformulate the Kennard-Stepanov relation (2.2) using Einstein coefficients instead of their typical absorbance and spectral fluorescence strength in their respective units. This way the unintuitive ω^3 factor vanishes and the relation becomes

$$\frac{B_{21}(\omega)}{B_{12}(\omega)} = \frac{w_\downarrow}{w_\uparrow}\exp\left(-\frac{\hbar(\omega-\omega_{\mathrm{ZPL}})}{k_\mathrm{B}T}\right) \tag{2.72}$$

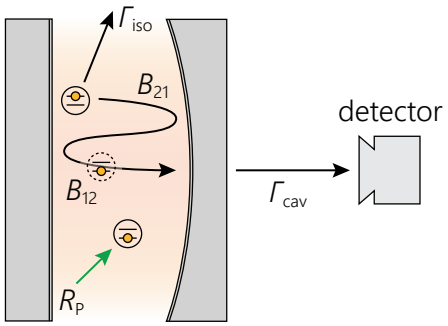

Fig. 2.6: Excitation conversion processes in the cavity. R_p is the external pump rate, $B_{12,21}$ are photon absorption and emission processes, Γ_{cav} is longitudinal mirror transmission and Γ_{iso} describes the chance of a molecule not to transfer its excitation to a cavity mode but release the photon into free space as understood from isotropic spontaneous emission.

where $w_{\uparrow,\downarrow} = \int_\epsilon \bar{g}_{\uparrow,\downarrow}(\epsilon)\exp(-\epsilon/k_BT)\mathrm{d}\epsilon$ are the statistical weights of the rovibronic substructure of the dye S_0 and S_1 states. Although one finds $w_\downarrow/w_\uparrow \approx 1$ for most dye species the factor is carried on in the following calculations steps for completeness [70]. Using statistical physics arguments one can show (see supplementary material of [102]) that the individual chemical potentials are linked to the dye excitation level and its zero phonon line ω_{ZPL} (see section 2.1),

$$\exp(\mu_\gamma/k_BT) = \exp(\mu_\uparrow/k_BT) \,/\, \exp(\mu_\downarrow/k_BT) \tag{2.73}$$

$$\exp(\mu_\gamma/k_BT) = \frac{w_\downarrow}{w_\uparrow}\frac{\rho_\uparrow}{\rho_\downarrow}\exp\left(-\frac{\hbar\omega_{ZPL}}{k_BT}\right) \quad . \tag{2.74}$$

We see that the experimentally tunable ratio $\rho_\uparrow/\rho_\downarrow$ sets the chemical potential. From here, the steady state population of a cavity mode is obtained by looking for a solution of (2.71a) with $\partial_t n_i = 0$. The individual rates balance out and by inserting (2.72) and (2.74) one then gets for the average occupation number $\bar{n}_i$ of a cavity state with energy $E_i = \hbar\omega_i$:

$$\bar{n}_i = \left(\frac{B_{12}(\omega_i)}{B_{21}(\omega_i)}\frac{\rho_\downarrow}{\rho_\uparrow} - 1\right)^{-1} \tag{2.75}$$

$$= \frac{1}{\exp((\hbar\omega_i - \mu_\gamma)/k_BT) - 1} = \frac{1}{\exp((E_i - \mu)/k_BT) - 1} \quad . \tag{2.76}$$

The expression is equivalent to the Bose-Einstein distribution. The resonator cutoff energy offset $m_{ph}\tilde{c}^2$ was subtracted from both the mode energy $\hbar\omega_i$ as well as the photon chemical potential, $\mu = \mu_\gamma - m_{ph}\tilde{c}^2$. The -1 term in the denominator arises due to the stimulated emission term in the rate equations. For exclusive spontaneous emission, i.e. for $\bar{n}_i \ll 1$, the cavity mode occupations scale Boltzmann-like realizing the classical limit. In this system, equilibrium fulfills detailed balance, as it is not realized by the absence of conversion processes but all processes are in equilibrium with their reverse counterpart. In this idealized setting of a perfectly closed system we see that the light spectrum is expected to acquire a thermal distribution by contact to the internally thermalized dye molecules.

2.5.2 Limit: Low Photon Numbers

The solutions of the differential equations (2.71a) and (2.71b) become highly nonlinear in the $\bar{n}_i > 1$ regime due to the self-enhancement of stimulated emission processes. For the phase space investigations explained in chapter 3 it is useful to simplify the model due to the experimentally realized limit of small photon numbers by weak optical pumping. Hence we first assume that

only a small fraction of molecules are in their excited state and we can assume a uniform ground state molecule density inside the resonator

$$\rho \equiv \rho_{\downarrow}(x) = \text{const.} \tag{2.77}$$

which renders the absorption time of a photon independent of its position but only its frequency ω_i. From now on, only the expression for $\rho_{\uparrow}$ is further considered in the calculations. We also neglect stimulated emission processes as we later distribute only around $\sum_i n_i \approx 100$ photons over more than 10^5 modes inside the resonator (see chapter 3) and thus $\bar{n}_i \ll 1$. Removing the affected terms yields

$$\partial_t n_i = \int_V \Big[B_{21}(\omega_i)\, u_i(x)\, \rho_{\uparrow}(x)\Big] \mathrm{d}x - \hbar\omega_i\, B_{12}(\omega_i)\, \rho\, n_i - \Gamma_{\text{cav},i} n_i \tag{2.78a}$$

$$\partial_t\, \rho_{\uparrow}(x) = \sum_i \Big[B_{12}(\omega_i)\, \rho\, u_i(x)\, n_i - B_{21}(\omega_i)\, u_i(x)\, \rho_{\uparrow}(x)\Big] - \Gamma_{\text{iso}}\, \rho_{\uparrow}(x) + R_{\text{p}}(x) \quad . \tag{2.78b}$$

Since we use an alternative definition of the spectral energy density u_i as we assume monochromatic light instead of a continuum of modes, the Einstein coefficients can be computed from the experimentally accessible dye spectra. By comparing the photon absorption term in (2.78a) to a generic exponential decay formula we get for the optical intensity I as it travels through a medium

$$I(t)/I_0 \equiv \exp(-\Gamma_{12} t) \tag{2.79}$$

$$\stackrel{!}{=} \exp(-\hbar\omega\, B_{12}(\omega)\, \rho t) \tag{2.80}$$

$$= \exp(-\log(10)\, \varepsilon \rho z) \tag{2.81}$$

where in a last step, the Lambert-Beer law of molar absorptivity was used. It relates the molar extinction coefficient ε of a medium (usually given in decadic base, hence the log(10) factor), concentration ρ and sample length z to the attenuation coefficient. Using $z = \tilde{c}t$ one gets by comparison

$$\Gamma_{12,i} = \log(10)\varepsilon(\omega_i)\tilde{c}\rho \tag{2.82}$$

for the absorption rate of a photon in mode i. Typical values are in the range 1 ps to 1 ns. From now on we make the substitution

$$\hat{B}_{12,21,i}(x) \equiv B_{12,21}(\omega_i)\, u_i(x) \tag{2.83}$$

$$= B_{12,21}(\omega_i)\, \hbar\omega_i\, |\psi(x)|^2 \tag{2.84}$$

where the energy density of a mode $u_i(x)$ was replaced by the spatial probability density function $\hbar\omega_i|\psi_i(x)|^2$. Rewriting (2.78a) and (2.78b) then yields

$$\partial_t n_i = \int_V \hat{B}_{21,i}(x)\, \rho_{\uparrow}(x)\, \mathrm{d}x - (\Gamma_{12,i} + \Gamma_{\text{cav},i})\, n_i \tag{2.85a}$$

$$\partial_t\, \rho_{\uparrow}(x) = \sum_i \Big(\hat{B}_{12,i}(x)\, \rho(x)\, n_i - \hat{B}_{21,i}(x)\, \rho_{\uparrow}(x)\Big) - \Gamma_{\text{iso}}\, \rho_{\uparrow}(x) + R_{\text{p}}(x) \tag{2.85b}$$

There are several approaches to solve the model. Those include e.g. finding the steady state in a set of coupled equations [105] or perform a physical time evolution with the Monte Carlo method, see section 2.5.4.

2.5.3 Limit: High Transverse Losses

Staying in the low photon number regime, we now investigate the cavity mode occupation in the case where fluorescence into free space modes is much more likely than emission into a cavity mode. The resonator mirrors offer high reflectance for paraxial beams but suffer from drastic reflectance drops even up to full transmission under incidence angles above around 25° (see Fig. 2.2 for the relevant spectrum from 550 nm to 590 nm). The photonic bandgap is hence only one dimensional, leaving the transverse emission channels presumably only moderately altered with respect to free space. In this section we investigate the limit where, after initial population of a mode, the following process is a photonic mirror transmission Γ_{cav} or, upon a potential reabsorption by the dye medium, a certain non-detected isotropic emission into free space perpendicular to the optical axis with rate Γ_{iso}. The number of molecule excitations caused by reabsorbed photons is then small compared to externally pumped excitations. As both terms containing $\hat{B}$ in (2.85b) can in this scenario be dropped out, the model reduces to

$$\partial_t n_i = \int_V \hat{B}_{21,i}\, \rho_\uparrow(x)\, \mathrm{d}x - (\Gamma_{12,i} + \Gamma_{\mathrm{cav}})\, n_i \tag{2.86}$$

$$\partial_t\, \rho_\uparrow(x) = -\Gamma_{\mathrm{iso}}\, \rho_\uparrow(x) + R_{\mathrm{p}}(x) \quad . \tag{2.87}$$

By integration we find the steady state of this model to be

$$\rho_\uparrow(x) = \frac{R_{\mathrm{p}}(x)}{\Gamma_{\mathrm{iso}}} \tag{2.88}$$

$$n_i = \frac{1}{\Gamma_{12,i} + \Gamma_{\mathrm{cav},i}} \int_V \hat{B}_{21,i}\, \rho_\uparrow(x)\, \mathrm{d}x \tag{2.89}$$

$$= \frac{\hbar\omega_i\, B_{21,i}}{\Gamma_{12,i} + \Gamma_{\mathrm{cav},i}} \int_V |\psi(x)|^2\, \rho_\uparrow(x)\, \mathrm{d}x \tag{2.90}$$

$$= \frac{\hbar\omega_i\, B_{21,i}}{\Gamma_{\mathrm{iso}}} \frac{1}{\Gamma_{12,i} + \Gamma_{\mathrm{cav},i}} \int_V |\psi(x)|^2\, R_{\mathrm{p}}(x)\, \mathrm{d}x \tag{2.91}$$

In the limit of dominating transverse losses Γ_{iso}, the molecular excitation $\rho_\uparrow(x)$ simply follows the pump beam profile. The mode occupation n_i follows a slightly more complex description, but leads to an equivalent conclusion. Since every excited molecule couples to every cavity mode (although in many cases with negligible amplitude) the resulting intensity distribution does not copy the pump profile but is nevertheless entirely determined by the latter. A statistical approach is not required as there is only negligible coupling between the modes. In the next paragraph we discuss the experimentally observable quantities and how they scale with the competing rates. One can again distinguish between two limiting cases given by the likelihood of at least one reabsorption during the resonator storage time.

If, however, the reabsorption time is much shorter than the cavity storage time, $\Gamma_{12,i} \gg \Gamma_{\mathrm{cav},i}$, the mirror transmission term can be neglected. In the spectral regime of $\lambda = 560...590\,\mathrm{nm}$ the ratio of emission and absorption scales proportionally to the Boltzmann factor $\hbar\omega_i B_{21,i} \,/\, \Gamma_{12,i} \propto \exp(-\hbar\omega/k_{\mathrm{B}}T)$ as verified by the relatively constant spectral temperature (Kennard-Stepanov relation, see Fig. 2.1) which then leads to

$$n_i \simeq \frac{\hbar\omega_i}{\Gamma_{\mathrm{iso}}} \frac{B_{21,i}}{\Gamma_{12,i}} \int_V |\psi(x)|^2\, R_{\mathrm{p}}(x)\, \mathrm{d}x \tag{2.92}$$

$$\approx n_{i,0} \exp\left(-\frac{\hbar\omega_i}{k_{\mathrm{B}}T}\right) \quad . \tag{2.93}$$

Here, $n_{i,0}$ is a scaling factor for the external pump induced occupation of mode i. It is generally not constant, however, the mode-pump overlap integral is, to a certain extent, an experimental

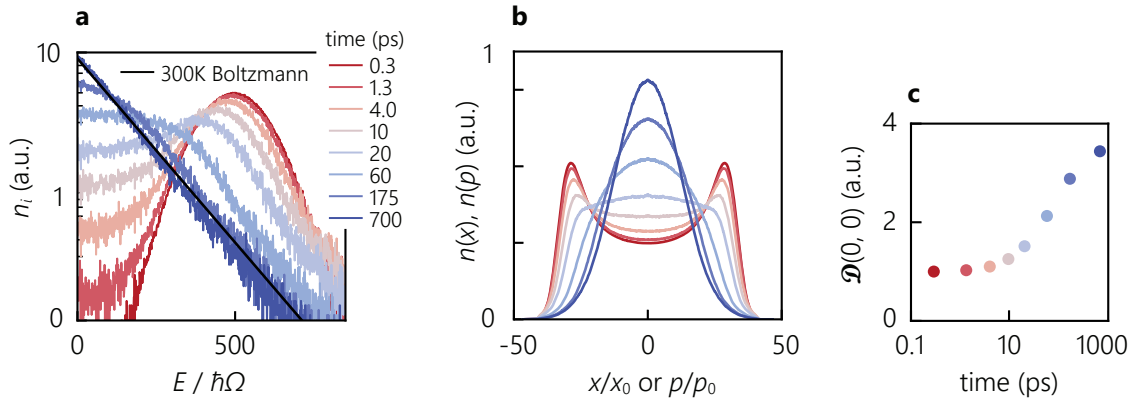

Fig. 2.7: Monte Carlo Simulation of a one-dimensional isolated photon gas, prepared in a highly non-equilibrium configuration. Curves or data points represent the system at different times. Simulations parameters: $q = 7$, $\lambda_c = 587\,\text{nm}$, $\Omega \approx 2\pi \times 40\,\text{GHz}$. **a)** Spectra converge towards a Boltzmann distribution at $T = 300\,\text{K}$. **b)** Spatial and momentum intensity distribution. Graph labels like in a). **c)** Temporal evolution of the central phase space density, normalized to its initial value at $t = 0$.

tuning parameter which allows for pumping each mode with equal strength. Within certain limits, the photon spectrum inside the resonator can then still scale Boltzmann-like caused by this inner filtering of the dye medium.

2.5.4 Monte Carlo Simulation

Due to the quantized photonic and molecular excitations in combination with known cavity eigenstates, this rate equation model can be time-evolved with a Monte-Carlo method [107, 108]. It is a technical approach since, instead of solving a large set of coupled equations, the underlying principle is that processes like pump excitation, photon absorption, photon emission and losses occur with a certain rate, i.e. a probability per time interval. On every step, a process is randomly drawn from all possible events, scaling with their occurring rate. After execution, all process rates are recalculated and the procedure is repeated until an exiting criterion is fulfilled, e.g. the pump source has excited N molecules or a simulation time of 100 ps has passed. As the implementation platform, the mathematically focused programming language "Julia" [109] was used.

As a benchmark, we simulate the time evolution of an isolated one-dimensional photon gas (i.e. no losses, cf. sec. 2.5.1) that is prepared in a highly non-equilibrium ("hot") configuration, i.e. a population of mainly high energetic states at time $t = 0$. Spatial, momentum and spectral distribution of the photon gas at different time stamps are shown in Fig. 2.7. In panel a) one can see how the initial spectral distribution continuously converges towards a Boltzmann distribution at $T = 300\,\text{K}$. The spectrum $n_i(E)$ is connected to the spatial and momentum distribution via $n(x, p) = \sum_i n_i |\psi(x, p)|^2$. In a harmonic oscillator potential, both (position and momentum) are equivalent when normalized to their characteristic scale x_0 or p_0, respectively, see sec. 2.3. The initial non-equilibrium spectra correspond to spatial and momentum distributions with overpronounced wings as seen in panel b). The clouds eventually transform to a Gaussian of width $\sigma \approx 90\,\mu\text{m}$ as expected at thermal equilibrium. The concentration towards low energetic states can be regarded as an effective cooling process. The mean central phase space density $\mathcal{D}(x = 0, p = 0)$ is extracted from spatial and momentum distributions as in (1.17) with numerical standard deviations. In panel c) one sees the that $\mathcal{D}(0, 0)$ increases as the photon accumulate in the trap center. The numerical simulation so far yields the expected results for the ideal system. The platform is further employed in sec. 3.2 with real experimental parameters including pump and loss rates.

CHAPTER 3

Experiments on Paraxial Light Concentration

This chapter deals with investigations of the central phase space density of the two-dimensional photon gas when its gradually enhancing its coupling to the dye environment. The approach refers to the transverse cooling proposal discussed in sec. 1.5. The two competing time scales are resonator lifetime τ_{cav} and photon reabsorption time $\tau_{\mathrm{abs}} = 1/\Gamma_{12}$. The latter varies by two orders of magnitude within the photon gas due to its broad spectral range. The resonator lifetime can be changed by varying the mirror distance and hence the cutoff wavelength or longitudinal mode number q. Those changes, however, are always accompanied by other experimental parameter variations such as trapping frequency (2.31), mirror transmission or pump laser absorption. A systematic way to conduct such an experiment is by varying the dye concentration in order to have a well controlled scaling of the photon reabsorption time while keeping the cavity aligment itself unchanged.

3.1 Experimental Setup

The setup is schematically depicted in Fig. 3.1. It comprises three major parts, namely the microcavity apparatus, the pump light sources (here laser and sunlight) and a detection part, where the cavity emission is analyzed by measuring its spatial, momentum and spectral distribution.

3.1.1 Dye-Filled Microcavity

The high-finesse cavity is the centerpiece of the experiment. It consists of two spherically curved dielectric mirrors (model: *CRD Optics* 901-0010-0550) with a radius of curvature of $\tilde{R} = 1\,\mathrm{m}$. Their theoretical transmission profile for a wide angular and wavelength range is shown in Fig. A.3. Under normal incidence $\theta \approx 0^\circ$, the mirror reflectance is above 99.99 % in the experimentally relevant range of $\lambda = 550\,\mathrm{nm}$ to 590 nm, as confirmed experimentally via cavity ring-down measurements [110]. The high reflectivity is reduced for beams travelling under a steep angle with respect to the optical axis, as discussed in sec. 3.4 The maximum photon storage time at a half wave number of $q = 7$ is of order 250 ps.

The ordered mirrors have 1” diameter and roughly 6 mm thickness. With these dimensions, the required small mirror separations for two dimensional photon gases are unreachable as the mirror edges collide, giving a minimum central separation of $D_0 = 2(\tilde{R} - \sqrt{\tilde{R}^2 - (0.5\text{”})^2}) \approx 150\,\mu\mathrm{m}$. Separations below 1 µm can be reached only if the diameter of at least one mirror is reduced to roughly 1 mm. The mirrors are initially cut into square pieces of 5 mm edge length. Afterwards, the substrate gets fixed in a rotating mount and the top side is ground into a round conical shape with grinding paper until the desired diameter is reached.

The pump light used to excite the dye solution is guided through one of the mirrors from the substrate backside at an incidence angle of roughly 42°, where the first transmission peak for

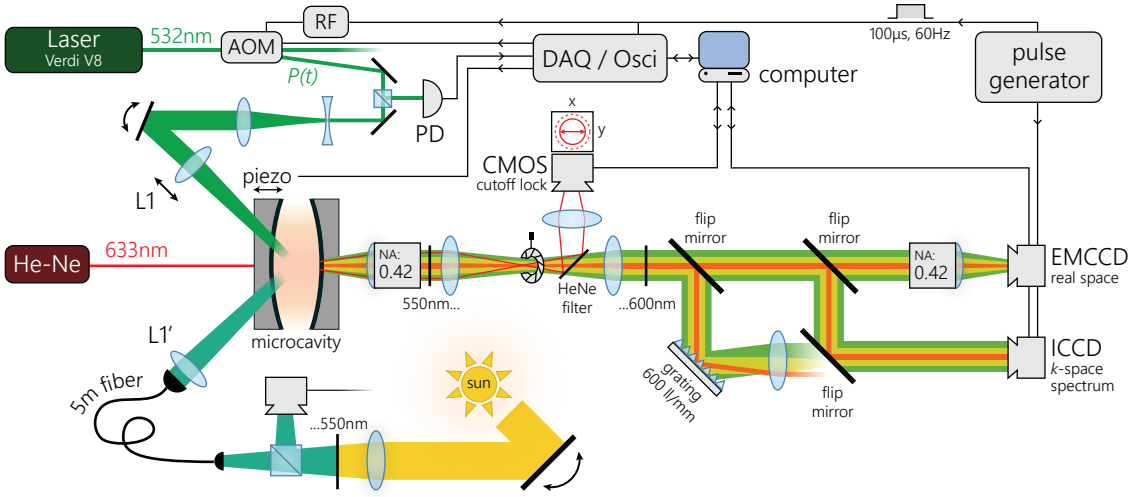

Fig. 3.1: Schematic view of the setup used for phase space investigations. The cavity is pumped by the green laser via a defocused pump spot. The cavity emission is in the analysis part of the setup guided onto different detectors via flip mirrors. Various devices are controlled or read out digitally. A He-Ne-laser beam is used for cavity stabilization. Instead of laser light one can also guide sunlight into the cavity via fiber coupling.

$\lambda = 532\,\mathrm{nm}$ light is found (see Fig. 2.2). To guide the beam, the mirrors are glued on top of an extra 1" glass substrate where four additional right angle prisms are added to enable a straight optical path with minimal refraction from the outside towards the cavity center, see Fig. 3.2b. For gluing, a UV-sensitive optical adhesive (type: *Thorlabs* NOA61) is used which gets initially cured by a UV lamp and afterwards by long-term weak sunlight exposure. Mirror pieces that are not used for backside-pumping are mounted into custom-made 1" aluminum adapters, shown in Fig. 3.2a.

The final 1" optics are inserted into regular mirror/optics mounts and 2" holders are employed with adapter plates for better optical access. The mounts are placed on top of micrometer positioning stages, so that each mirror is rotatable and translatable in x and y direction. One mirror is placed on a z-translatable stage with manual translation via a fine-thread screw as well as an integrated piezoelectric stack (model: *Radiant Dyes* RD-KRU-FGS-25-01 with piezodrive). The latter allows for fine adjustment of the stage in z direction and hence the mirror separation D_0 with nanometer precision; the required voltage can be set both manually (potentiometer) as well as with a computer-controlled voltage supply (variable offset voltage) within a range of 150 V. For this purpose, a computer-controlled multi-functional data acquisition and voltage output device (DAQ, model: *National Instruments* USB-6003) is integrated into the setup.

Although the cavity mirror mounts are locked in place on a breadboard which is mechanically stabilized via rubber feet, the cavity cutoff wavelength $\lambda_c = 2\tilde{n}D_0/q$ is subject to vibrations in the 1 Hz range and long term drifts due to e.g. temperature changes or air convection, which is actively compensated for with the piezo element. The mirror separation is also monitored by illuminating it with a helium-neon laser beam ($\lambda_{\mathrm{HeNe}} = 632.8\,\mathrm{nm}$) as it operates in a moderately reflecting regime of the mirrors ($R \approx 1\,\%$) and shows negligible absorption by the dye medium. Due to the spherical curvature of the mirrors, an interference pattern known as Newton rings emerges whose radius changes with the mirror distance. The light is deflected from the main beam path via a dichroic mirror and imaged on a CMOS camera, where the ring radius is extracted via a computer software and the piezo voltage adjusted via a feedback loop. Due to the inertia of the whole cavity setup, the control bandwidth is limited to frequencies below 1 Hz which is usually sufficient to stabilize the cutoff wavelength down to 1 nm precision over long times.

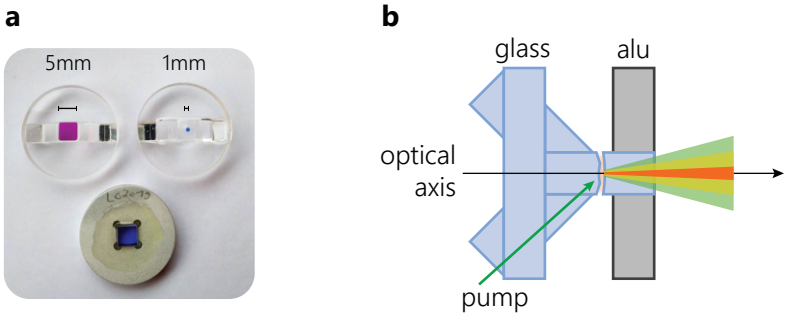

Fig. 3.2: a) Front view of cavity mirrors glued onto glass substrates (top) or clamped into aluminum mount (bottom). In the latter, residual gaps are sealed with epoxy resin. **b)** Side view of the cavity mirror arrangement.

The rhodamine 6G dye (see sec. 2.1) is dissolved in ethylene glycol that gets dropped between the two mirrors. The solvent has a sufficiently high viscosity to stick between the mirrors via adhesion and evaporates slowly over several days. For the experiments, different concentrations are systematically prepared by diluting an initial sample by adding well-defined proportions of solvent (see sec. 3.3.1).

3.1.2 Laser and Sunlight as Pump Sources

In the initial phase of the experiment, the dye molecules inside the resonator are optically excited with a beam derived from a diode pumped solid state laser (model: *Coherent* Verdi V8) operating at a wavelength of $\lambda_p = 532\,\text{nm}$, which is close to the dye absorption maximum. The laser provides a Gaussian TEM_{00} mode with a beam quality of $M^2 < 1.1$ and a power stability of 1 % [111]. The pump beam powers are kept far below the condensation threshold power to mimic continuous sunlight exposure. However, the pump beam is chopped to 100 µs pulses at a repetition rate of 60 Hz to increase the signal to noise ratio of the cavity emission detection while keeping the average power constant at around 10 µW as the dye bleaches during operation (see sec. 2.1), which has to be strictly avoided since the phase space measurements rely on absolute powers normalized to the incoming pump beam power. For such low pump powers, molecule diffusion is sufficiently fast to counteract the bleaching. The pump beam is temporally modulated by two subsequent acousto optical modulators (AOM), whose driver electronics are gated by a digital delay generator (model: *Stanford Research Systems* DG645) and an arbitrary function generator (model: *Tektronix* AFG3252), which both provide the same gating signal. The second AOM serves the purpose of better suppression of residual pump light during the dark times. The pump power is monitored with a photodiode after branching off parts of the light by a 70:30 (T:R) beam splitter. The signal voltage is determined by an oscilloscope (model: *Tektronix* DPO2024B, 200 MHz bandwidth), which is read out by the computer software. If necessary, the control voltage of the second AOM driver is adjusted via the DAQ device to maintain a constant pump power. Since the laser does not reliably provide such low pump powers and the AOM electronics become too noisy at low voltage levels, the laser head emits several hundred milliwatts of power, which are attenuated by neutral density filters to keep the power more stable. Inside the cavity, the pump spot is intentionally slightly defocused by displacement of lens L1 (see Fig. 3.1) and has a width of 180(20) µm fwhm to induce the desired initial mode occupation (see also sec. 2.5).

In a second stage of the experiment, the laser pump source was replaced by sunlight to demonstrate potential solar light concentration. For this porpose, a 2” broadband mirror was used in combination with a 2” lens focusing the light into an optical multimode fiber of core diameter 200 µm. To counteract earth’s rotation, the mirror is mounted onto two motorized stages (angular resolution: 0.01°), which are controlled via a computer controlled feedback loop. Part of the

light is guided onto a camera to track the movement of the sun. Without readjustment, the sun moves out of focus in roughly one minute. Light with wavelengths above 550 nm is filtered out as it does not reasonably contribute to the absorbed power but disturbs the measurement. The light path is after a certain position superimposed with the pump laser path and finally imaged into the cavity. With a suited spherical aperture and working slightly out of focus, a comparable pump beam spot size of 180 µm fwhm can be created, analogous to the laser light pump spot. Although the fiber receives several milliwatts of sunlight power – three orders of magnitude above the laser pump powers – the power absorbed by the dye compares to the laser beam absorption because the extinction coefficient of rhodamine 6G drops fast outside the central absorption region of 520 nm to 540 nm and the cavity mirrors vary in their transmission.

3.1.3 Analysis Setup

Light detection Properties of the photon gas inside the resonator are extracted from its transmitted part and are analyzed spatially, spectrally and in momentum space. After leaving the resonator, the light is captured by a long working distance apochromatic microscope objective (*Mitutoyo* 20X plane APO) with an effective focal length of $f = 1\,\mathrm{cm}$ (working distance: 2 cm) and a numerical aperture of NA $= 0.42$. The maximum detectable divergence angle is 25°. A 550 nm longpass filter (*Thorlabs* FELH0550) is placed directly after the objective lens to block scattered pump light. The emission is then focused again where in the intermediate image plane a spherical iris is placed for alignment and spatial filtering purposes, followed by another collimation. In-between, the helium-neon laser light is coupled out of the beam path and another removable 600 nm cutoff shortpass filter (*Thorlabs* FESH600) is placed in the path which blocks residual helium neon laser light and the red-wing rhodamine emission which is not significantly altered by the cavity due to the high transmission in this spectral regime and hence is expected to behave similar to isotropic spontaneous emission.

Real and Momentum Space The spatial distribution is obtained by real space imaging; the optical path is a symmetric chain of confocally arranged lenses with focal lengths $\{1, 10, 15, 15, 10, 1\}$ cm, which creates a one-to-one image of the photon gas on the camera sensor. Unity magnification was chosen as the signal for low dye concentrations tends to be very small with only ≈ 10 photons per pixel. The light can also be guided onto an ICCD camera, where the slightly different lens configuration images the angular distribution (momentum space, see sec. 1.6) onto the camera sensor; the lens arrangements is $\{1, 10, 15, 15, 20, 7.5\}$ cm. Both cameras are single photon sensitive and capable of single-pulse-resolved image acquisitions which are digitally averaged (≈ 10 images) during the process, see also sec. 3.1.3.

Spectrum The spectral distribution is measured by guiding the light onto a diffraction grating (*Thorlabs* GR50-0650) with 600 grooves/mm via a flip mirror. The grating in combination with the following lens spectrally disperses the incoming light such that the spectral distribution can be extracted via a vertical integration of the camera signal. The pixel to wavelength calibration was performed using a commercial spectrometer. The self-build spectrometer has superior sensitivity and does not contain an entrance slit. Due to the harmonic oscillator dispersion relation of the photon gas the mode energy is strongly related to the propagation path in real and momentum space (see sec. 2.3.3); an entrance slit would cause overpronounced filtering of higher order modes as they lie far outside in both phase space coordinates. A trade-off is that the resolution is reduced since the spatial information of the modes is completely restored in the image plane. Due to the small mode spacing of $\Omega \approx 2\pi \times 40\,\mathrm{GHz}$ many neighboring modes overlap in the spectral image; the effect enhances for higher mode orders since the mode diameter scales square root like with energy. However, as the spectrum mainly serves the purpose of determining the longitudinal mode number q and the cutoff wavelength with 1 nm precision, the mentioned

drawback is of minor significance. Due to the finite numerical aperture of the objective lens the apparatus can only reliably detect energies up to $3.5\,k_\mathrm{B}T$ (see sec. 2.3.3). Since every harmonic oscillator wave function has contributions inside the detectable range only parts get cut off, see also sec. 2.3.1. All lenses in the analysis part are achromatic doublets (model family: *Thorlabs* AC508-...-A-ML, 2" diameter except for lens after the cavity objective lens).

High Sensitivity Cameras

Since the observables in this experiment are purely photonic, state of the art detectors are used to maximize data quality. We employ two types of cameras which are able to detect intensities down to the single photon level, namely an EMCCD or an ICCD camera, both of which are explained in the following.

EMCCD Electron multiplying CCD cameras (EMCCD) offer excellent performance for spatially resolved light detection on a single photon level. The used model is iXon Ultra A-DU897-UCS-BV from Andor Technologies, which offers a peak detection quantum efficiency of 97 % in the relevant wavelength range. The $(16\,\mu\mathrm{m})^2$ sized pixels and are aligned on a 512 times 512 grid. Although single impinging photons still only generate a single electron-hole pair in the pixel well, the readout electronics include a low noise electron multiplication process with variable gain settings [112]. During a shifting process in a semi-conductor register, the signal electrons have chance to release further electrons from the bulk via so-called impact ionization (creating additional electron-hole pairs in the conduction band) scaling with the kinetic energy gained by the applied shifting voltage. Since this process happens prior to the analog to digital conversion, even single photoelectrons produce a sufficient signal to noise ratio to allow for reliable photon counting. The sensor is cooled (usually to around $-40\,^\circ\mathrm{C}$) to reduce spontaneous excitation of thermal electrons which are indistinguishable from regular photoelectrons. The sensor exposure time can not go below several milliseconds due to the limited readout speed, hence the cavity emission during a pump pulse of 500 ns length is always fully temporally integrated.

ICCD An intensified CCD camera is a detector with nanosecond time resolution, where the incoming light releases electrons from a photocathode, which are accelerated towards a micro channel plate where, similar to impact ionization, incoming electrons are multiplied depending on the anode voltage. Afterwards, the amplified electron beam hits a phosphor screen whose resulting light emission is imaged on a camera. The intensifier can be switched on an off in nanoseconds. The detection quantum efficiency of order 60 % and limited spatial resolution due to e.g. the diameter of a micro channel ($\approx$ 10 µm on the camera sensor) result in a slightly lower sensitivity and resolution compared to EMCCD cameras. The used model is a "C9546-02-71, 2MCP, P43" image intensifier in combination with an "ORCA Flash 4.0" CMOS camera, both manufactured by the company Hamamatsu.

3.2 Light Concentration Measurement Scheme

The phase space density of the photon gas inside the resonator is inferred from its spatial and momentum distributions. We start by discussing the experimental parameter space and how to interpret the data.

After excitation of the dye molecules inside the resonator volume by the pump laser beam, spontaneous emission at position x will populate a resonator mode ψ_i with energy $\hbar\omega_i$. The corresponding rate for each mode scales with the spatial overlap $|\langle x|\psi_i\rangle|^2 = |\psi_i(x)|^2$ and the dye emission strength $\hat{B}_{21,i}(\omega_i)$, cf. sec. 2.5. A molecule at position x couples by photon absorption and emission to all modes with energy $E_i > m\Omega^2x^2/2$ as those have a reasonable amplitude in

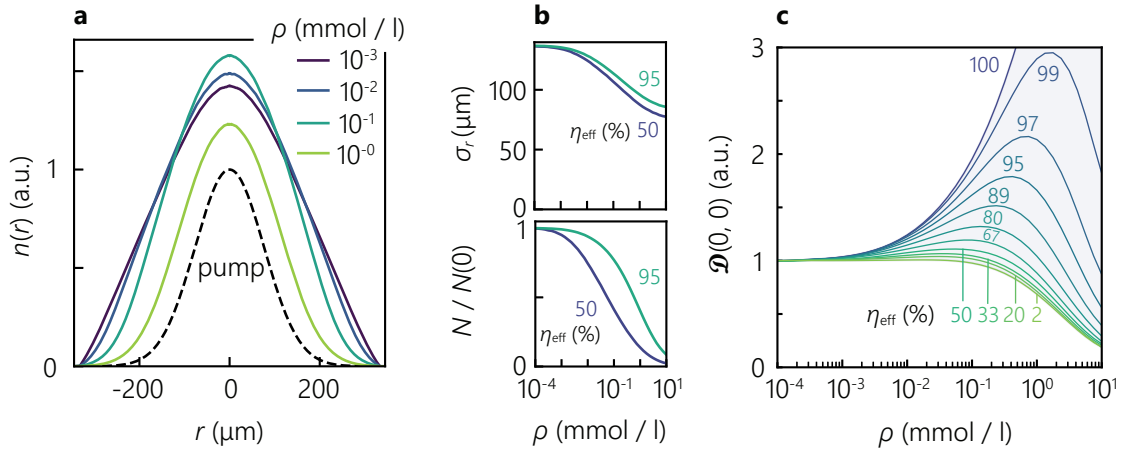

Fig. 3.3: Numeric exploration of the photon gas at different dye concentrations for given initial parameters. **a)** Radial intensity profiles for different dye concentrations and $\eta_{\text{eff}} = 95\,\%$. The dashed line shows the pump excitation profile. **b)** Extracted cloud widths and total photon number normalized to $N(\rho = 10^{-4}\text{mmol/l})$, calculated for different effective quantum yields η_{eff}. **c)** Normalized central phase space density increase for various η_{eff} as a function of the dye concentration ρ.

their energetically allowed region (neglecting transverse wave nodes). In contrast, coupling to lower energetic modes is negligible as $|\psi_i(x)|^2 \approx 0$. Therefore, the initial spontaneously emitted photon cloud is broader than the pump excitation profile, see also the theory curves in Fig. 3.3a. Moreover, the pump beam width can now be chosen such that the initial photon cloud is broader than the thermal equilibrium width

$$\sigma_r(T) = \sqrt{k_{\text{B}}T/m\Omega^2} \tag{3.1}$$

$$\overset{T=300\,\text{K}}{\approx} 92\,\mu\text{m} \tag{3.2}$$

or correspondingly $\Delta r_{\text{fwhm}} = 2\sqrt{2\log(2)}\,\sigma_r \approx 215\,\mu\text{m}$, where m is the photon mass and Ω is the trapping frequency. If the cavity is filled with a very dilute dye solution, e.g. $\rho = 10^{-2}$ mmol/l, a reabsorption of the cavity photons during the resonator lifetime is unlikely; the photon gas will remain in its initial configuration until the light leaves the cavity via mirror transmission. When the experiment is repeated using a higher dye concentration, the photons get reabsorbed during the storage time; reabsorption of photons in higher energy modes is stronger as the absorption rate roughly scales like $\Gamma_{12}(\omega) \propto \exp(\hbar\omega/k_{\text{B}}T)$ in the spectral regime around $\lambda \approx 580\,\text{nm}$. For strong reabsorption and reemission rates one expects the photon cloud, independent of its initial configuration, to transition into the thermal equilibrium state, which in the harmonic trap is a Gaussian of width $\sigma_r(300\,\text{K})$, see also sec. 2.5.4. During thermalization, the photons are expected to accumulate around the transverse cavity center and equivalently, propagate closer to the optical axis at lower transverse momenta. The redistribution of photons towards the trap minimum leads to an increase of the central phase space density as compared to the initial configuration.

Notably, each reabsorption process has a nonzero chance for photon losses. The major channels arise from the finite fluorescence quantum yield ($\eta_{\text{R6G}} \approx 95\,\%$) and unconfined spontaneous emission under large angles with respect to the optical axis as the mirror reflection profile is high only around normal incidence (see Fig. 2.2) and does not significantly alter the free photon density within this solid angle. While the non-unity quantum yield in our context is an unavoidable loss channel, the ratio of transversally emitted (and hence for our purpose lost) photons to the paraxial ones (captured by the resonator) is not known per se. The predominantly one-dimensional band gap of the cavity still reduces the solid angle of unmodified free space emission and a Purcell enhancement [113] of fluorescence into the centrally located resonator modes has

not been thoroughly investigated for the present system [72]. Therefore, although its value is unknown, we introduce an effective quantum yield η_{eff} that includes both loss channels. The emission rate of an excited molecule at position x into any resonator mode is the sum over all individual contributions with the Einstein coefficient for emission $\hat{B}_{21,i}(x) = B_{21,i}\,\hbar\omega\,|\psi_i(x)|^2$ that already includes the mode function $\psi_i(x)$. As in the low photon number limit only the *ratio* of emission into and out of the cavity is relevant, we calculate η_{eff} as

$$R_{\text{cav}}(x) = \alpha \sum_i \hat{B}_{21,i}(x) \tag{3.3}$$

$$\eta_{\text{eff}} = \frac{R_{\text{cav}}(x)}{R_{\text{cav}}(x) + \Gamma_{\text{iso}}} \tag{3.4}$$

where the ratio can be scaled by a factor α to account for its yet unknown value. The finite free space fluorescence quantum yield $\eta \approx 95\,\%$ is also included in Γ_{iso} as it is also formally described as a transition rate (sec. 2.1.3). It turns out that the spatial dependence of $R_{\text{cav}}(x)$ can be omitted in the central region of the cavity.

The impact of losses on the phase space evolution can be investigated with a Monte-Carlo simulation, sec. 2.5.4. The pump spot width is set to 180 µm fwhm and the cutoff wavelength to $\lambda_c = 587$ nm. The system gets time evolved until a certain number of molecules were excited by the pump beam and no photonic or molecular excitations remain inside the cavity. The central phase space density is, similar to as planned in the experiment, calculated from the accumulated photon cloud via (1.17)

$$\mathcal{D}(\mathbf{0},\mathbf{0}) = \frac{1}{4\pi^2}\frac{N}{\sigma_r^2\sigma_p^2} \quad . \tag{3.5}$$

where σ_{r,p_r} are the standard deviations of the respective distributions. Alternatively, if the density profile in some cases does not compare well to a Gaussian function, σ_{r,p_r} can be identified with the root mean square of the distribution, $\sigma_r = \sqrt{\langle r^2\rangle - \langle r\rangle^2}$. The results of a simulation for $\eta_{\text{eff}} \approx 95\,\%$ are depicted in Fig. 3.3. In panel a), several radial intensity profiles that form during the resonator lifetime are shown for different dye concentrations. For $\rho = 10^{-3}$ mmol/l, the cloud basically remains in its initial configuration, which is broader than the pumping profile (dashed line). As the dye concentration is increased one can observe the expected reshaping of the cloud as it gets narrower and the intensity increases at $r = 0$. When the width has converged to the thermal equilibrium value of $\sigma_r(300\,\text{K})$, every additional reabsorption process does (on average) not further compress the phase space distribution but only continues to induce photon loss, hence there is an ideal amount of reabsorption processes to maximize the phase space density. Next, the simulation is carried out for different η_{eff} where σ_r and photon number N are extracted from the profiles; Two exemplary curves are shown in panel b) for $\eta_{\text{eff}} = \{50, 95\}\,\%$. In theory, σ_r and σ_{p_r} are identical up to a conversion factor, hence only σ_r is shown. The behavior of σ_r is very similar in both cases as it converges to the expected $\sigma_r \approx 90\,\mu$m for the high quantum yield $\eta_{\text{eff}} = 95\,\%$ whereas it drops slightly earlier for $\eta_{\text{eff}} = 50\,\%$ and converges to a value slightly below the thermal width; this is understood from faster photon loss of higher energetic modes, which significantly reduces the cloud width. Similar behavior is visible for the photon number N, which is shown normalized to its initial value $N(\rho = 10^{-4}\text{mmol/l})$. Even for rather high effective quantum yield, N decays to $\approx 25\,\%$ for typical dye concentrations of 1 mmol/l typically used in the experiment. For $\eta_{\text{eff}} = 50\,\%$, the drop occurs already at one magnitude smaller concentrations and is significantly steeper. One finds the behavior of σ_r and N to not differ a lot for $\eta_{\text{eff}} < 50\,\%$ anymore (not shown). Finally, we calculate the relative phase space density in the trap center for varying η_{eff} shown in panel c). If the only loss channel was the finite fluorescence quantum yield corresponding to $\eta_{\text{eff}} = 95\,\%$, the maximum phase space compression factor would be around 2 instead of around 6 in the ideal case $\eta_{\text{eff}} = 100\,\%$ (curve not fully shown). If the effective quantum

yield from undirected spontaneous decay rises above $\eta_{\text{eff}} = 50\,\%$, $\mathcal{D}(\mathbf{0}, \mathbf{0})$ increases no more than 20 %, while for an almost certainly lossy reabsorption process $\eta_{\text{eff}} < 10\,\%$, it does naturally not increase with ρ, but only exhibits a reduction. In this regime the curves look almost identical.

3.3 Experiment

3.3.1 Preparation

The goal of this part of the experimental work is to probe the spatial, momentum and qualitatively the spectral profile of the photon gas at different dye concentrations to examine the effect of increased reabsorption on the photon gas, transferring it from its initial configuration (dictated by the pump beam) into the thermal steady state (dictated by the Kennard-Stepanov law (2.2)). Differently concentrated dye solution samples are prepared by repeated dilution of a highly concentrated initial sample ($\rho = 3\,\text{mmol/l}$) with additional solvent using a milligram sensitive scale. Since the dye concentration can not be reliably changed during a running experiment, each data point is obtained after reassembling the cavity. The total intensity values are normalized to the absorbed pump power where a proportional scaling of the power with the dye concentration is assumed as the absorbance is $\lesssim 1\,\%$ (short sample approximation). The actual amount of absorbed pump light is inaccessible within the required precision, which is uncritical as the relevant quantity is the relative absorbance of different solutions. The uncertainty of the concentration ratios are estimated to be of order 1 %. The molar extinction of the $\rho = 0.01\,\text{mmol/l}$ solution in a cuvette can be measured in situ using the $\lambda = 532\,\text{nm}$ pump laser and confirms the textbook value of $\varepsilon(532\,\text{nm}) \approx 114\,000\,\text{cm}^{-1}\,\text{L}\,\text{mol}^{-1}$ within a 5 % uncertainty. The pump beam diameter inside the resonator was prepared to 180(20) µm fwhm prior to operation by removing one cavity mirror and coating the remaining mirror with a low-concentrated dye film. The occurring fluorescence profile then resembles the pump excitation profile at the otherwise not directly accessible position inside the cavity. The ellipticity of the Gaussian pump beam due to its incidence under an angle of 42(1)° with respect to the optical axis can be partially compensated for by tilting a lens in the beam path (not shown in figure).

A major difficulty during data acquisition is dye residue on the mirror substrate, which tends to accumulate inside tiny gaps and produce background fluorescence from places outside the resonator. Additionally, the dye residue can potentially contaminate the low dye concentration samples as some molecules are dissolved again and diffuse into the resonator volume. To prevent this, the mirror on the analysis side of the setup is mounted inside a custom made aluminum mount (see Fig. 3.2) and the gaps are filled with two component glue (manufacturer: UHU) based on epoxy resin. After curing, it resists the used solvents (ethylene glycol or acetone) and reliably seals this part of the cavity.

Measurement Procedure Since the cavity is disassembled and set up again for every dye concentration data point, it is challenging to reproduce the same experimental conditions in every run, but there are methods expedite the process. Although the mirror surrounding is sealed with epoxy resin, cleaning of the mirrors, especially removing the previously used dye solution with acetone soaked lens tissues has to be done more rigorously than usual. When the mirrors are inserted back into their mounts, only the smallest required amount of dye solution is dropped between the mirrors to avoid residuals outside the mirror region. Moreover, the mirrors are initially aligned with respect to the optical axis via backreflection of the helium neon laser beam. Their separation is reduced, first with the manual translation stage and the final micrometers with the integrated piezo actuator. Upon pumping the cavity, the same half wave number q can be set every time by comparing the cavity cutoff wavelength λ_c with the newton ring radius of the helium neon laser interference. Since both wavelengths are distinct, the combination of the two quantities allows to identify q. This is essentially crucial as a varying cavity length implies a

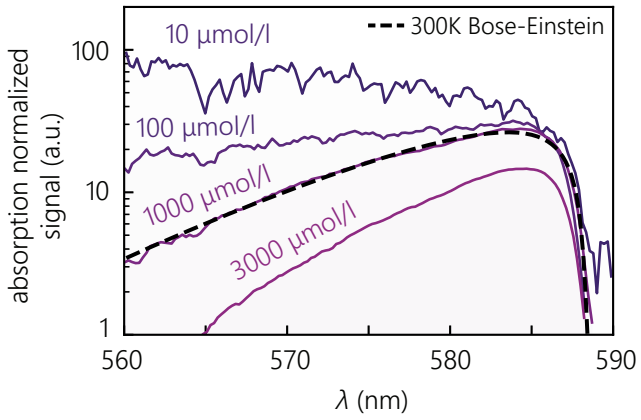

Fig. 3.4: Cavity emission spectra for different dye concentrations ρ. The data is corrected for mirror transmission and normalized to the absorbed power assuming proportional scaling with ρ.

different trapping frequency and changes the pump beam absorbance due to the different dye film thickness. After alignment and feedback locking of the cutoff wavelength, real and momentum space images of the photon gas along with spectra are recorded.

3.3.2 Resonator Emission Data

Spectral Distribution

We begin our discussion of the dye concentration-dependent resonator emission by examining several photon gas spectra which are shown in Fig. 3.4. All curves are normalized to the absorbed pump light, which is assumed to scale proportional with the dye concentration ρ. Additionally, to convert the measured signal to mean intensities inside the resonator, the data is rescaled with the wavelength dependent transmission of the mirrors, see Fig. 2.2. For low dye concentrations like $\rho = 10\,\mu\text{mol/l}$, where photon reabsorption during the resonator lifetime is still unlikely due to the long absorption times compared to the resonator storage time ($\Gamma_{12} \ll \Gamma_{\text{cav}}$), the spectral modes show an almost uniform occupation with higher energy modes (small wavelength) being strongest – a distribution far from thermal equilibrium. Due to the low pump beam absorption, the signal-to-noise ratio is comparatively low. Upon increasing ρ one observes a systematic change in the slope of the spectral tail. This is expected as the dye absorption rate in this spectral regime increases exponentially with decreasing wavelength. At the in other dye-microcavity experiments typical concentration of $\rho = 1\,\text{mmol}$ the spectrum agrees with a Boltzmann distribution, calculated for a temperature of 300 K. The regime of $\Gamma_{12} \gg \Gamma_{\text{cav}}$ is entered for even higher concentrations where the slope of the distribution still changes slightly but is also accompanied by a global decline in the signal. Note that the obtained spectral information is directly connected to the spatial and momentum profiles as higher energetic modes contribute in the outer regions of the trap.

Spatial and Momentum Distribution

The central phase space density $\mathcal{D}(\mathbf{0}, \mathbf{0})$ of the photon ensemble is extracted from the spatial and momentum space profiles, which are both inferred from the cavity emission. Exemplary raw data ($\rho = 1\,\text{mmol/l}$) for a laser pumped cavity is shown in Fig. 3.5. In panel a) one sees that both profiles are spherically symmetric and of roughly Gaussian shape as seen in the cut profiles shown in the bottom half of the figure in arbitrary linear units, which where extracted at the position of the dashed line. The emission angle refers to the quantity as entered into the objective lens, after refraction at the outer face of the mirror substrate, see sec. 2.3.3. In

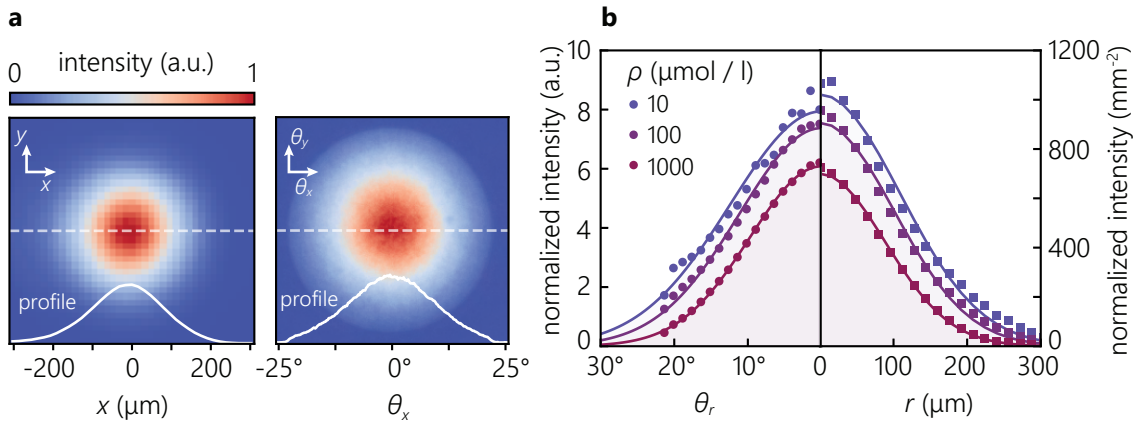

Fig. 3.5: Spatial and momentum distribution. **a)** Cavity emission in real and momentum space with a cut profile from the position of the dashed line (arbitrary units, $\rho = 1\,\mathrm{mmol/l}$). **b)** Absorption-normalized, radially averaged real (right) and momentum space profiles (left) recorded at different dye concentrations.

the momentum space picture one can see that the finite aperture of the objective lens cuts off emission angles above roughly 23° which is consistent with the maximum expected collected emission angle resulting from the numerical aperture NA = 0.42.

Exemplary radially averaged profiles are shown in panel b) for three exemplary dye concentrations, here obtained from the laser-pumped cavity. Since the absorbed power scales proportionally with the dye concentration and the experiment is operated with constant pump power to avoid bleaching effects, the data is normalized to the dye concentration for a reasonable comparison. The concentration dependent shape qualitatively reproduces the behavior shown in Fig. 3.3a. Both, spatial and momentum component, show the same behavior as expected from their equivalence in the harmonic oscillator. Agreements with Gaussian fit functions is given, from which σ_r and σ_θ (with $\theta^2 = \theta_r^2 = \theta_x^2 + \theta_y^2$) can be extracted. Slight variations in the intensity are typical for these experiments, since at low dye concentrations the signals are very weak. For the following analysis, the experiment was repeated several times. However, the reduction of the cloud width does here not go along with an increase of the central intensity, indicating that the system is subject to significant photon loss, cf. sec. 3.2.

3.3.3 Phase Space Density

From the obtained profiles the behavior of the central phase space density as a function of the dye concentration is extracted. However, the momentum space cutoff introduced by the finite microscope aperture requires a brief discussion of its implication for the measured spatial distribution. The finite aperture acts as a low pass filter of spatial frequencies; its effect on the spatial wave function is illustrated in Fig. 3.6a. In the trap center, where the momentum of a classical particle is maximized, the wave function oscillates the fastest. If outer, large momenta are clipped, the spatial wave functions are filtered predominantly in their central high-frequency region, which can be confirmed in the experiment by e.g. momentum clipping using an iris in the Fourier plane. Therefore, the observed spatial cloud contains less photons and appears slightly broader than its unfiltered counterpart. To accent for this, we introduce a correction factor for

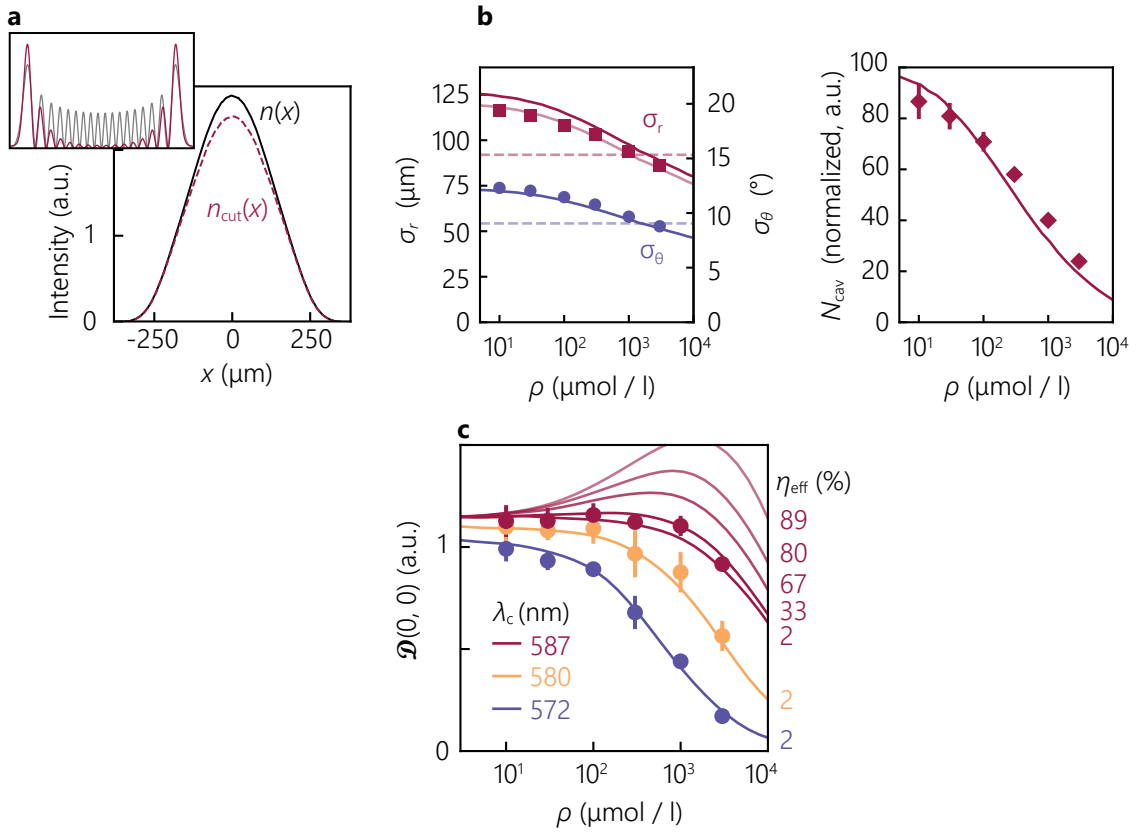

Fig. 3.6: a) Effect of finite aperture on the spatial intensity distribution. High frequency filtering in momentum space causes the central intensity to decline (inset: single mode density example, same axes). **b)** Extracted data for real space width σ_r, momentum space width σ_θ and normalized remaining cavity photon number N for various dye concentrations at $\lambda_c = 587\,\mathrm{nm}$. Solid lines are numerics for $\eta_{\mathrm{eff}} \approx 2\,\%$, cf. sec. 3.2. Dashed lines are predictions for $T = 300\,\mathrm{K}$. **c)** Extracted central phase space densities from the data in b) with theory curves for different η_{eff} taken from Fig. 3.3.

the photon number N and spatial width σ_r as

$$N \approx N_{\mathrm{exp}} \left(1 - \exp\left(-\frac{1}{2}\frac{\theta_{\mathrm{max}}^2}{\sigma_\theta^2}\right)\right)^{-1} \tag{3.6}$$

$$\sigma_r \approx \sigma_{r,\mathrm{fit}} \left(1 + \exp\left(\frac{\sigma_\theta - 190\,\mu\mathrm{m}}{20\,\mu\mathrm{m}}\right)\right)^{-1} \tag{3.7}$$

where the correction for N is analytic as the momentum space profile can be extrapolated as a Gaussian while the correction for σ_r is empirically obtained from numerical simulations. Since the intensity distribution here is an incoherent superposition of single mode densities one has to apply the Fourier filter to each individual wave function prior to summation, which is cumbersome analytically. The correction factor for N reaches values up to $\approx 20\,\%$ whereas the σ_r correction is below 5 %.

Figure 3.6b shows exemplary measured cloud widths for a cutoff wavelength of $\lambda_c = 587\,\mathrm{nm}$ and absorption normalized output photon numbers N_{cav}. The corresponding calculated central phase space densities are shown in panel c) for three different cutoff wavelengths $\lambda_c = \{572, 580, 587\}\,\mathrm{nm}$. The shown values are averaged over three measurement series (5 data points for the three lowest ρ values); the statistical errors of the extracted σ values are smaller than the data point size. After applying the correction factors to the data, the phase space density does not significantly increase here and eventually drops at higher dye concentrations. Comparing with estimations shown in Fig. 3.3, such behavior is expected for low effective quantum yields. For

comparison, several theory curves with different η_{eff} from Fig. 3.3c are shown for $\lambda_c = 587\,\text{nm}$ (red). The predictions for $\eta_{\text{eff}} < 33\,\%$ are all very similar, hence the data suggests within the experimental uncertainty that we are operating in this low effective quantum yield regime. The remaining theory curves for the other cutoff wavelengths are both for $\eta_{\text{eff}} = 2\,\%$ but also here several curves match within the experimental uncertainty (not shown). The dye concentration ρ has to be slightly scaled to match the data (same factor for all curves, cf. sec. 2.2.2). The momentum widths σ_θ are reproduced by the theory curve, whereas the spatial widths σ_r systematically lie below the expected values; a 5 % downscaled theory curve is shown for comparison. This is unexpected as both should be fully correlated in a harmonic oscillator environment. Towards smaller clouds spatial and momentum widths tend to agree better. This could be a consequence of momentum space extrapolation, which includes infinitely large transverse momenta beyond the resolvable region. Given the lower reflectivity of the mirrors for non-paraxial incidence angles of $\theta \gtrsim 25^\circ$, the mirrors might not provide a confinement anymore beyond the resolvable angular range. Additionally, due to the mirror curvature, the mechanical mirror separation in the outer parts of the cavity eventually drops below a single half wave node and a proper resonance condition (see sec. A.1) can not anymore be fulfilled. A further investigation has been pursued by imaging the cavity emission with a higher numerical aperture as described in sec. 3.4.

Apart from varying the cavity cutoff wavelength and thus the spectral working regime of the dye, several further tests were performed such as replacing the dye medium with perylene diimide solved in acetone, varying pump beam sizes from 50 µm to 300 µm or using different cavity mirror coatings. In none of these cases, a significant phase space density increase could be observed. For the mirrors, a dielectric coating was designed in cooperation with the LASEROPTIK GmbH company, aiming for better suppression of isotropic fluorescence; the transmission profile is shown in Fig. A.3. While the stop band of these mirrors covers the experimentally relevant spectral region over a wide angular range, the high transmission of p-polarized light around the Brewster angle [69] of here around 60° is unavoidable for Fresnel reflection based mirrors.

3.4 Transverse Losses and High NA Imaging

The observed absence of a phase space density increase motivates further investigation of the actual loss probability of a photon per emission process, theoretically and experimentally. The total emission rate into the resonator volume can be estimated by employing the Einstein coefficient, which quantify the coupling of a single molecule to a cavity mode via absorption and emission of a photon. The absorption rate in (2.85b) measures per volume, hence integrating over a unit volume yields a molecule number M and a single photon absorption rate $R_{\text{abs},i} = \hat{B}_{12,i} M$. The molar extinction coefficient ε in (2.82) measures per molecule density and can be converted to a concentration independent cross section σ via Avogadro's constant N_A. By comparing their respective absorption formulae we get $\varepsilon \rho \tilde{c} = \sigma \tilde{c} M/V$. For the volume V, we identify the (local) effective mode volume $V_{\text{eff}}(x) = q\lambda_c/(2\tilde{n})|\psi(x)|^{-2}$ [114–116]. After changing the units of ρ from mol per liter to particles M per m^3, one can compute the Einstein coefficients via

$$\hat{B}_{12,i} = \frac{\sigma(\omega_i)\tilde{c}}{V_{\text{eff},i}} = 10^3 \log(10) \frac{\varepsilon(\omega_i)}{N_A} \frac{\tilde{c}}{V_{\text{eff},i}} \qquad \text{and} \tag{3.8}$$

$$\hat{B}_{21,i} = \hat{B}_{12,i} \exp\left(-\frac{\hbar(\omega_i - \omega_{\text{ZPL}})}{k_B T}\right) \tag{3.9}$$

where $\hat{B}_{21,i}$ is obtained via the Kennard-Stepanov relation (2.72). As an example, one finds for the emission rate of a molecule at the harmonic trap center ($r = 0$) into the TEM_{00} ground mode $\hat{B}_{21,00}(r = 0) \approx 12\,\text{kHz}$. To obtain the capture efficiency of the complete cavity one has to sum over all bound states in the resonator. Given that the mirrors are only highly reflective up to an

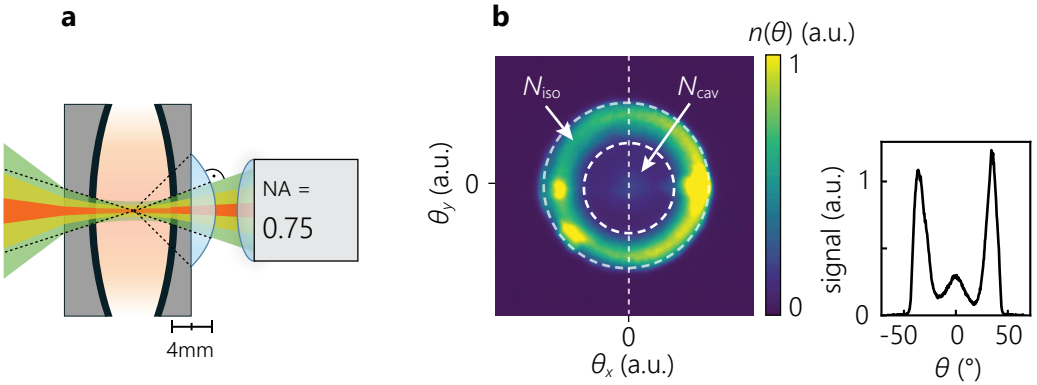

Fig. 3.7: High NA imaging of the resonator emission. **a)** Working principle of the hemisphere lens: Light originating from the center of the sphere is not refracted since it crosses the surface under normal incidence as compared to the left side. **b)** Cavity fluorescence in momentum space. Inner ring shows the captured momentum range with medium NA optics. The outer ring denotes the maximum detectable angle ($\theta_{\mathrm{max}} \approx 48^{\circ}$) of the setup shown in a). The cut profile from the vertical line position allows for a better comparison of inner and outer part of the signal.

incidence angle of around 25°, we sum over modes with energy $E_i < 1000\hbar\Omega$ according to (2.43). Contributions of higher energetic modes decline in the cavity center due to their increasing mode volume, however, the mode degeneracy $g(E) \propto E/\hbar\Omega$ in combination with the increasing fluorescence strength towards higher energies $\hat{B}_{21}$ roughly compensates for this; accordingly, the emission rate into the cavity per energy level is approximately constant within the central region of the resonator. A full numeric evaluation then yields for the total emission rate into the resonator

$$\sum_{E_i<1000\hbar\Omega} \hat{B}_{21,i}(x=0) \approx 7\,\mathrm{MHz} \quad . \tag{3.10}$$

Comparing this value to the free spontaneous decay rate of rhodamine $\Gamma_{\mathrm{spont}} = 1/4\,\mathrm{ns} = 250\,\mathrm{MHz}$ one finds the emission rate into the cavity to be much smaller, corresponding to $\eta_{\mathrm{eff}} \approx 3\,\%$; A comparable result has been obtained in ref. [105]. For an intuitive comparison, one gets in a geometrical picture for the solid angle of the reflection cone with apex angle 25° a fraction $\tilde{\Omega}/4\pi = 2\sin^2(\theta/2) \approx 10\,\%$ [117], where the factor of 2 accounts for two-mirror symmetry of the cavity.

To experimentally determine the transverse photon loss fraction changing the imaging setup allows for the detection of larger emission angles. For this purpose, a solid immersion lens [118, 119] (SIL, supplier: Edmund Optics) is employed in combination with a microscope objective (model: *Mitutoyo* 50x M plane APO) of numerical aperture NA = 0.75 and 5 mm working distance. The working principle is shown in Fig. 3.7a. The SIL is a glass hemisphere, which is positioned such that the photon gas lies within its spherical center. This arrangement suppresses refraction of the outgoing light away from the optical axis at the substrate surface[1] and thus increases the detectable angular range by a factor corresponding to the refractive index of the medium $\tilde{n}$. To deploy this configuration in the optical microcavity setup, a mirror substrate is ground and polished down to 2 mm thickness and the SIL is then glued onto its backside using optical adhesive. Given the total thickness of 4 mm, the microscope objective can be placed close enough for proper imaging. The maximum detectable emission angle is $\theta_{\mathrm{max}} = \arcsin(0.75) \approx 48^{\circ}$. The obtained momentum space distribution together with a vertical line cut using a dilute dye sample ($\rho = 0.01\,\mathrm{mmol/l}$) is shown in Fig. 3.7b, indicating that only a small fraction of fluorescence

[1] The refractive index of the dye solvent (ethylene glycol, 1.44), mirror substrate (quarz, 1.46) and lens (N-BK7, 1.52) still slightly differ, which is neglected for simplicity.

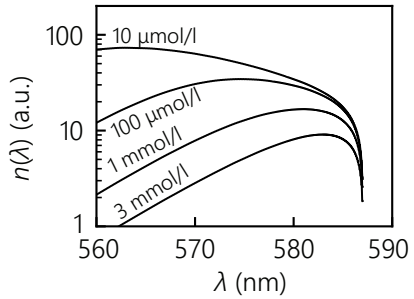

Fig. 3.8: Semi-analytically obtained spectra for $\eta_{\text{eff}} \to 0$, calculated with (2.91) after precalculation of the required coefficients.

photons couple to the cavity modes, the latter are visible as a dim cloud in the central region of the image. The doughnut shaped signal is unconfined fluorescence that passes through the mirrors. In this angular range $\theta \gtrsim 25^\circ$ the mirror transmission for p-polarized light rises up to $\approx 100\,\%$. The photons accordingly spend several femtoseconds inside the dye medium, which lies far below the dye absorption times of order picoseconds and nanoseconds regime causing rapid photon losses in this solid angle. The bright spot on the right (with a weak reflection on the left) arises from pump beam light, as it also propagates within the detectable angular range.

The capture efficiency of the cavity can be quantified by comparing the emitted photon number from the cavity N_{cav} (see 3.7b) with the absorbed pump power (from a comparable measurement). For this measurement a low dye concentration of 0.01 mmol/l is chosen to avoid reabsorption by the dye during the resonator storage time. From the molar extinction coefficient of rhodamine 6G the pump beam absorbance becomes

$$P_{\text{abs}}/P_0 = 10^{-\varepsilon\rho L_{\text{dye}}} \tag{3.11}$$

$$\approx 0.025\,\% \tag{3.12}$$

where $L_{\text{dye}} = (q - q_0)\lambda_c/2\sqrt{2}$ is the dye film thickness between the mirrors. Here, $q - q_0$ is an experimental correction for the mechanical mirror separation (see sec. 2.2.2) and the factor $\sqrt{2}$ accounts for the diagonal crossing of the medium. The integrated signal emitted from one resonator side can be compared to the pump beam signal itself when directing it onto the camera sensor (using a neutral density filter). One then finds the fraction of detected photons with respect to absorbed photons to be

$$\frac{N_{\text{cav}}}{N_{\text{abs}}} \approx 0.02(1) \tag{3.13}$$

which already takes into account correction factors for the loss from finite quantum yield, partial transmission of the pump beam towards the dye medium and that the photons leave the cavity on both sides. The uncertainty of N_{abs} in this measurement is very large, but even with a relative error of several hundred percent the capture efficiency of the cavity would remain a single-digit percentage.

The large loss probability would correspond to the regime in sec. 2.5.3. From (2.91) one can analytically obtain spectra for different dye concentrations as shown in Fig. 3.8. Their apparent similarity with the experimentally obtained spectra shown in Fig. 3.4 gives further evidence that the dye-microcavity system in the limit of small photon numbers operates at large transverse losses, predominantly caused by high mirror transmission under large incidence angles as compared to e.g. isotropic scattering on the surface.

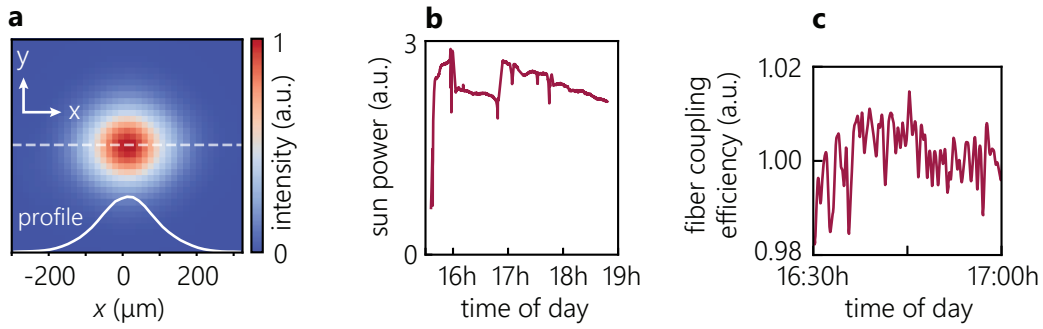

Fig. 3.9: Pumping the cavity with sunlight. **a)** Spatial image of the thermalized photon cloud emitted from the microcavity. **b)** Captured sunlight power, which decreases as the sun sets in the afternoon. Short term variations arise due to changing atmosphere transmission caused by e.g. clouds. **c)** Fiber coupling efficiency. It is stable within 1 % accuracy, realized by feedback controlled mirror adjustment to counteract earth's rotation.

3.5 Sunlight Pumping

To investigate the potential real world application of a solar light concentrator, the pump laser was replaced by actual sunlight, see sec. 3.1.2 for the fiber coupling apparatus based on a motorized mirror. The sunlight spectrum is filtered to $\lambda_{\text{pump}} < 550\,\text{nm}$ as the dye absorption is negligible at longer wavelengths and to avoid spectral overlap of the pump light with dye fluorescence. The sunlight pump spot was adjusted to reproduce the shape of the laser pump spot with fwhm 180 µm. The observed spatial emission profile as seen in Fig. 3.9a is comparable to the laser pumped case, which is a direct consequence of Kasha's rule, cf. sec. 2.1.

The measurements start in the afternoon due to the orientation of the building. The power of the captured sunlight fluctuates on a timescale of seconds and minutes due to e.g. passing clouds, see Fig. 3.9b. The long term temporal decrease happens due to the continuous sun set, where the optical path length through the atmosphere and correspondingly Rayleigh scattering are gradually increased [120]. Spectral red shift of the pump light due to the cross section scaling $\propto \omega^4$ turns out to be negligible during the given time period. For a stationary setup, the fiber coupled sunlight vanishes within one minute due to the changing incidence angle of the sun. Automated readjustment of the mirror keeps the coupling efficiency (power before the fiber divided by power after the fiber) on a constant level with a temporal jitter of order 1 %, see Fig. 3.9c. With the tracking apparatus it was possible to operate the experiment comparable to the weakly laser pumped system. To achieve a detectable cavity emission signal at low dye concentrations like $\rho \leq 0.1\,\text{mmol/l}$, the experiment has to be carried out on a cloudless day, preferably during the summer period.

3.6 Discussion

So far, a phase space compression inside the here presented dye-microcavity system based on repeated absorption and emission could not be demonstrated. The theoretical and experimental findings suggest that a spontaneous emission process, which follows upon a reabsorption process and is required to redistribute the high energetic photons towards the trap center, is accompanied by losses which ultimately prevents photons from accumulating in the low energy states.

Despite this circumstance, the rate equation model in sec. 2.5.3 suggests that under continuous pumping, the observation of a thermal Boltzmann distribution in the photon spectrum at otherwise typical concentrations around $\rho \approx 1\,\text{mmol/l}$ does not contradict the previously reported findings. For adequate experimental settings, mainly the combination with the spectral

emission profile $\Gamma_{12}(\omega)$ of fluorescence following pump irradiation with the reabsorption rate $\Gamma_{12} \propto \exp(\hbar\omega/k_{\mathrm{B}}T)$ (and hence the induced losses) project the initial photon cloud on a 300 K Boltzmann distribution. However, this does not go along with a redistribution of the mode excitations but with a selection of modes. Moreover, the time-resolved measurements in [65] are carried out in a stimulated emission dominated regime, which greatly enhances the cavity capturing efficiency, re-establishing the possibilities for redistribution. Perspectives to increase the confinement capabilities of the resonator in the spontaneous emission regime are discussed in chapter 5.

Concerning the potential use as a solar light concentrator, the apparatus so far supports the incoupling of sunlight. On sunny days, the absorbed power inside the resonator is of the same order as compared to the laser power chosen to stay below the noticeable bleaching threshold. As expected, the obtained density profiles look similar with respect to the laser pumped case.

CHAPTER 4

Experiments on Homogeneously Trapped Photon Gases

This chapter deals with the experimental implementation of high quality flat-bottom potentials for light and measurements on uniform photon gases, in particular its response to weak potential gradients.

Trapping photons in a homogeneous potential introduces additional requirements to the experimental setup. While spherical mirrors for harmonic traps can be ordered from stock, the rectangular outlines of a box structure have to be imprinted in a custom process. In this thesis they are created by locally elevating the surface of a mirror, effectively creating repulsive potential walls and for a finite-size homogeneous confinement. The enclosed region where the photon gas is stored remains untouched, which is an important advantage over other techniques such as CO_2 laser milling [21], because additionally induced surface roughness can render sensitive measurements of the ground mode unfeasible. In earlier works, this circumstance was the main obstacle that hindered investigations in this new direction.

In the beginning of this chapter, the basic properties of a photon gas in a box are investigated, namely spatial, momentum and spectral distribution. Comparing its caloric properties such as internal energy and the closely related specific heat, the behavior across the phase transition confirms the absence of a discontinuity as expected for a two-dimensional uniform gas. By controlled introduction of a linear potential gradient, experimentally realized by sensitive tilting of one of the cavity mirrors, one can extract the equation of state (EoS) $n = n(\mu, T)$ and the isothermal compressibility κ_T of the system. The theoretical predictions have to account for a finite trap depth for our experimental box implementation.

4.1 Potential Creation

Nanometer precise structuring of a mirror surface has recently opened entirely new possibilities for the investigation of two-dimensional photon gases [25, 59, 60, 121]. Since commercial mirror substrates are only available with planar or spherically curved surfaces, the creation of tailored local surface topographies is a powerful tool for investigating photon gases in highly non-trivial potential landscapes [122]. The here used structuring method was developed in our research group in previous works [123–126].

A dielectric mirror is a stack of thin layers (thickness of order $\lambda/4n \approx 100\,\mathrm{nm}$, n is the refractive index) made of alternating materials, where mechanical stress occurs at each material interface due to the atomic crystal structure mismatch [127, 128]. The stress is enhanced by the production process of the mirrors: The material is typically deposited via ion beam sputtering [129] where ions (e.g. argon) are accelerated onto a solid material target consisting of the desired coating material. On impact, surface atoms are sputtered off the bulk and condense on the mirror

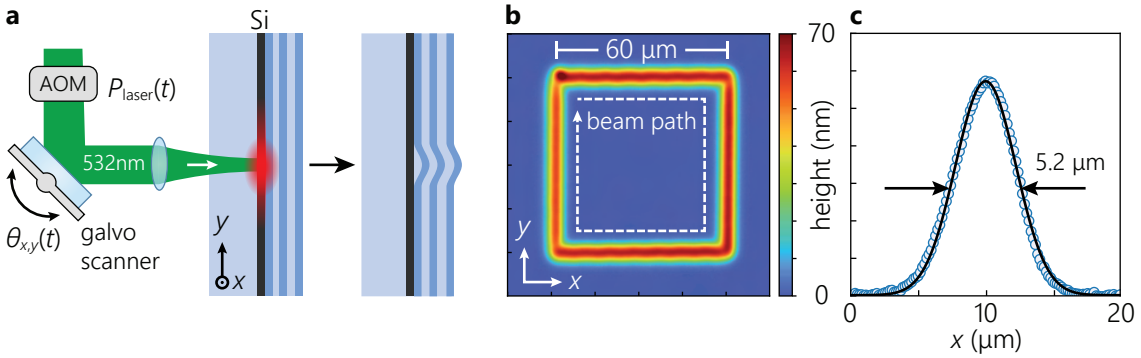

Fig. 4.1: a) Principle of mirror structuring by delamination. A laser beam ($\lambda = 532\,\mathrm{nm}$) is irradiated from the substrate side and focused onto the silicon layer (black) where part of it gets absorbed and the impact region heats up (red glow). Upon release of the induced thermal stress the layer stack lifts up permanently. To reach different lateral positions of the surface, the laser beam is steered by a two-dimensional galvo scanner whose relative tilt angle (θ_x, θ_y) is translated to a position (x, y) on the silicon layer via a lens. The power $P(t)$ is controlled by an acousto-optic modulator. **b)** Exemplary height profile of a square structure, created by steering the laser beam along the depicted path. The height axes are valid for b) and c). **c)** Height profile cut through the left structure edge depicted in b) with a Gaussian fit.

substrate in a highly controlled way. The process is performed at temperatures of order 100 °C [130]. Afterwards, the coating is tempered to ambient conditions which further increases the stress between the layers due to their different thermal expansion coefficient, which can result in slightly curved mirror surfaces with radii of curvature being of order 100 m [130].

The above mentioned behavior can be systematically exploited to create permanent mirror surface structures by locally inducing material stress in a well-controlled way [131]. Here we use a focused laser beam (diameter $\approx 1\,\mu\mathrm{m}$ fwhm) to locally introduce heat, see Fig. 4.1a. Since the dielectric layers of the cavity mirrors show negligible absorption in the visible or infrared wavelength regime (where most high beam quality laser sources are available), they contain a 30 nm thick silicon layer between dielectric coating and glass substrate, which absorbs around 30 % of the incoming light. The locally increasing temperature causes a thermal expansion mismatch between the dielectric layers, ultimately leading to a permanent elevation of the mirror surface. Presently, this "delamination" mechanism is understood from the layers close to the substrate detaching from one another and resulting in a lift of the surface during the process [132].

4.1.1 Microstructuring Setup

The setup scheme used for performing controlled delamination is shown in Fig. 4.1a and is realized in a different apparatus. As a light source, a continuous-wave solid state laser (Model: Verdi G12, $\lambda = 532\,\mathrm{nm}$, Manufacturer: Coherent) is employed to benefit from its high quality $M^2 < 1.1$ beam profile and power stability [111]. While the laser head runs at constant output power, the writing beam power $P_{\mathrm{laser}}(t)$ is temporally modulated via an acousto-optic modulator. A set of two orthogonally rotatable mirrors (galvo scanner, manufacturer: Thorlabs) is used to steer the laser beam over the mirror sample. A convex lens transforms the resulting propagation angles $(\theta_x(t), \theta_y(t))$ into positions $(x(t), y(t))$ on the sample plane while preserving the longitudinal focus position (Fourier transform, see sec. 1.6). The focus diameter roughly measures 1 µm. Galvo scanner and acousto-optic modulator driver are controlled via custom computer software.

The light reaches the silicon layer from the backside. For the given Si layer thickness, one observes a deformation of the mirror surface above a threshold power of around 25 mW. The resulting surface elevation increases with the deposited thermal energy, e.g. by increasing the laser power or illumination time [59]. When the elevation exceeds heights around 60 nm, further

energy deposition results in a threshold-like degradation of the reflective properties, verified by a strong increase of the mirror transmission which renders tens of micrometers of the surrounding surface unusable for our experiments [123]. Simple outlines are created by linearly steering the laser beam over the surface in the desired pattern as illustrated for a square pattern in Fig. 4.1b. Other methods are decomposing every target topography in point-like patterns or iterative writing [60].

The height profiles are measured via white-light interferometry using a so-called Mirau interferometer. It operates like a Michelson interferometer where the mirror sample is placed at the end of one arm. By moving the sample in z direction, the interference signal in the output path can be employed to determine the position dependent phase shift between neighboring pixels $\Delta\varphi(x, y) = k\Delta D(x, y)$ and hence straight forwardly compute the two-dimensional height profile of a reflecting surface in a single scan, see ref. [59] for details of this setup.

4.1.2 Properties of Delaminated Regions

The delamination process is intrinsically limited in its transverse spatial resolution. The induced surface deformation turns out to be of Gaussian shape as visible in Fig. 4.1b and c. Its intrinsic width of $\sigma = 2.2(1)\,\mu\text{m}$ ($\approx 5\,\mu\text{m}$ fwhm) significantly exceeds the heating beam diameter. It corresponds to a 10 % to 90 % rise length of

$$\ell_{\text{rise}} = \sqrt{2}\sigma\left(\sqrt{-\log(0.1)} - \sqrt{-\log(0.9)}\right) = 3.7(2)\,\mu\text{m} \quad . \tag{4.1}$$

The finite spatial resolution of the imaging apparatus with $\sigma_{\text{res}} \approx 0.3\,\mu\text{m}$ merely alters the experimental result by around 1 % as seen from $\sigma^2_{\text{real}} = \sigma^2_{\text{fit}} - \sigma^2_{\text{res}}$ for Gaussian distributions.

As a final note we discuss the consequence of the structuring treatment for the mirror reflectivity. For this purpose, a cavity ring down measurement was carried out in [60, 126] with the resonator mode being located on a large delaminated area of a certain height. The measurements revealed that for $\Delta D \lesssim 15\,\text{nm}$ there was no observed impact on the reflectivity while a sample with $\Delta D = 18\,\text{nm}$ showed an increased loss $1 - R$ of 200 % with respect to lower heights. Higher structures have not been investigated in this context.

4.1.3 Box Potential Structures

Since the locally induced surface elevation $\Delta D(x, y)$ acts as a repulsive potential (see sec. 2.3), a box potential is created by structuring the region of the potential border, leaving the actual box region unstructured. We know from sec. 2.3 that the photon potential is connected to the height profile in first order approximation via

$$V(x, y) = m_{\text{ph}}\tilde{c}^2\frac{\Delta D(x, y)}{D_0} = 4\pi\hbar\frac{c_0\tilde{n}}{\lambda_c^2}\frac{\Delta D(x, y)}{q} \tag{4.2}$$

where the last term solely depends on experimentally accessible variables. The final height profiles of different sized box potentials are shown in Fig. 4.2a. In all following measurements we employ quadratic boxes ($L \equiv L_x = L_y$). To suppress photon loss via tunneling through the potential barrier [121, 124], a thick potential border is created by steering the laser beam over the mirror surface in square shaped paths of different edge length, starting with the innermost loop. The observed drop in elevation height towards the outer regions as seen in Fig. 4.2b is an intrinsic effect of the delamination process when the paths overlap and the heating beam power is constant throughout the process. Although higher potential barriers are technically possible (50 nm with the used mirrors, 200 nm (corresponding to $\approx 10k_{\text{B}}T$) were realized with a thicker Si layer) we find that elevation heights above 25 nm do not allow for photon trapping anymore, see sec. 4.4. Thus, the experimentally caused slight asymmetry in the shown boxes is of only minor

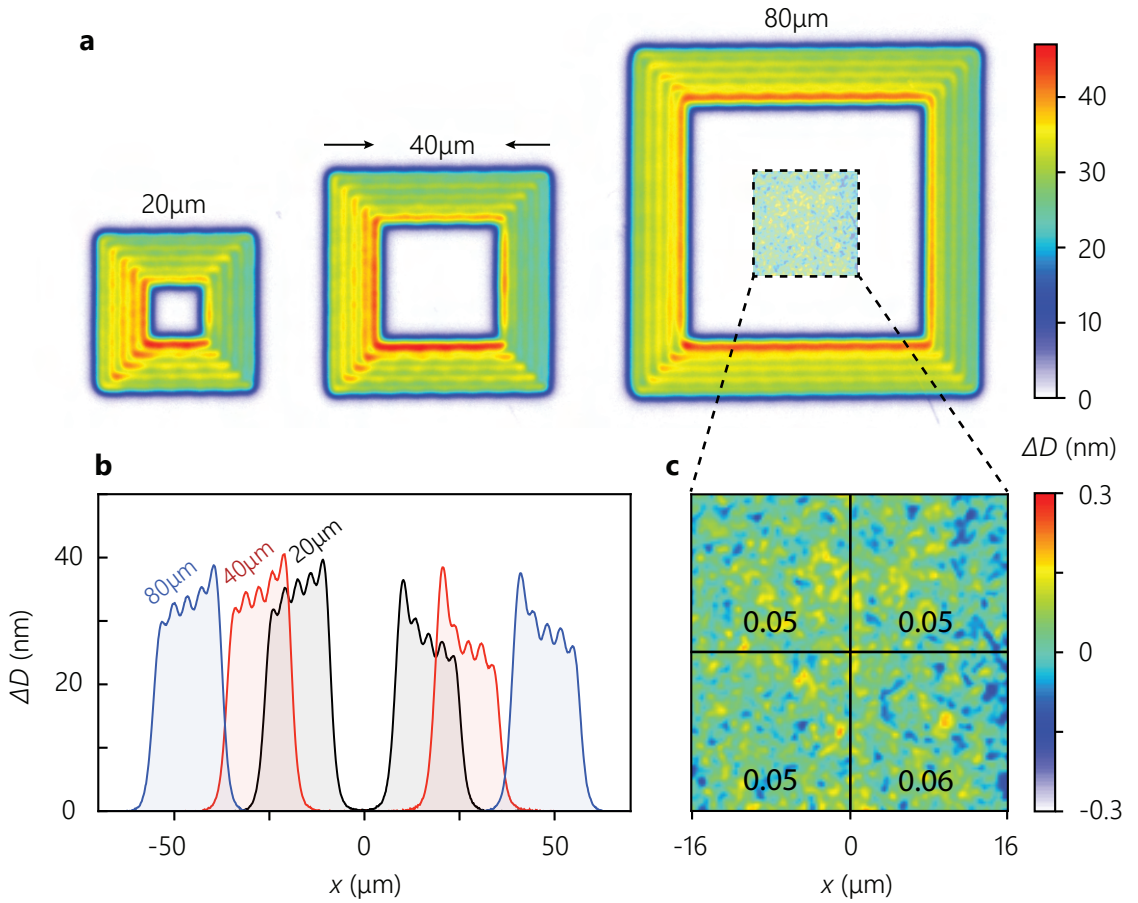

Fig. 4.2: Mirror surface structures. **a)** Height profiles of delaminated box potentials with different edge lengths L. **b)** Horizontal cuts through the data in a). **c)** Surface roughness of the unstructured trapping region. Subregions are labeled with their local surface roughness (rms value in nanometers).

significance. Since the surface quality (roughness and reflectivity) of the delaminated regions tends to suffer from stronger buckling, the border height is raised slightly further above what is still effective. Due to the intrinsic finite rise length of the delamination process, the potential shape begins to adopt harmonic character for small box sizes with $L \to \ell_{\mathrm{rise}}$ visible in the line cut for the $L = 20\,\mu\mathrm{m}$ box in Fig. 4.2b. Due to ℓ_{rise} the effective box size in the bottom region tends to be around 4 µm smaller than its design size (sec. 4.3.1).

Up to this point only the characteristics of the potential border have been discussed. Prior to surface structuring, the availability of state-of-the-art superpolished mirror substrates and coating specifications also plays a crucial role. The photon gas mainly occupies this non-delaminated region, where the surface roughness affects the reflectivity via scattering and the eigenenergies similar to a weakly disordered potential when the noise features vary on smaller length scales than the mode function. The surface topography of an untreated mirror surface is shown in Fig. 4.2c (different color scale). The roughness is defined as the rms of the local surface height profile [133]

$$\delta D = \sqrt{\langle (\Delta D)^2 \rangle - \langle \Delta D \rangle^2} = 0.05(1)\,\mathrm{nm} = 0.5(1)\,\text{Å} \tag{4.3}$$

which on the resolvable length scale of 1 µm is of the same order as the Bohr radius $a_o \approx 0.53$ Å. The height uncertainty of 0.1 Å is estimated by comparing subsequent recordings of the same region. When comparing the disorder potential generated by this surface roughness to the ground

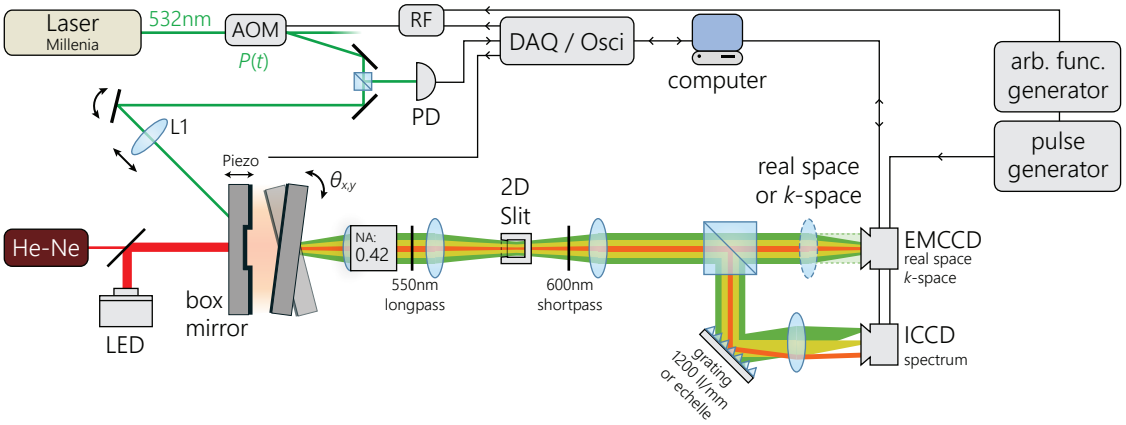

Fig. 4.3: Experimental setup for the investigation of homogeneously trapped photon gases. A tiltable cavity is optically pumped by a green laser and the resulting cavity emission is analyzed in real space, momentum space and spectrally resolved.

mode energy in a box one can estimate for experimental parameters $q = 7$ and $\lambda_c = 583\,\mathrm{nm}$ that

$$V_{\mathrm{noise}} \approx 2\pi\hbar \times 12.5\,\mathrm{GHz} \stackrel{!}{=} \frac{\pi^2\hbar^2}{m_{\mathrm{ph}}L^2} = E_{11} \tag{4.4}$$

which for $L \gtrsim 40\,\mu\mathrm{m}$ exceeds the ground state energy in the box; from here on a significant distortion of the spatial mode distribution is expected. A corresponding behavior is experimentally confirmed, see sec. 4.3.2.

4.2 Experimental Setup

The experimental setup for the investigation of homogeneously trapped photon gases is schematically depicted in Fig. 4.3. Its basic operation principle is similar to the one presented in chapter 3 (Fig. 3.1), with modifications explained in the following.

4.2.1 Cavity Mirror Holders

Subnanometer precise alignment of the cavity mirrors plays a crucial role when working with flat mirrors and homogeneous potentials. While for spherical mirrors the potential is insensitive to the exact mirror alignment with just the potential minimum location being shifted, the situation drastically changes for flat potential environments, where a tiny deviation from perfectly parallel mirrors causes a beam walk-off. In a box with 40 µm side length the ground state energy is $E_{11} \approx 2\pi\hbar \times 13\,\mathrm{GHz}$. Analogous to the surface noise potential, the state gets significantly perturbed if the mirror distance varies by more than 50 pm on the given length scale. As manual alignment via fine-thread screws is unfeasible during operation, both cavity mirrors are equipped with either piezo actuator stacks or piezo driven screws allowing for sub-nanometer alignment capabilities as depicted in Fig. 4.4a. The left mirror mount is a 2” high-stability (stainless steel, model: *Thorlabs* Polaris K2S2P) mirror mount with integrated piezoelectric adjusters (continuous range: 17 µm or 280 µrad). The latter are operated with a voltage of 0 V to 150 V which are supplied by a manually and externally controllable four channel voltage amplifier. The right mirror is a regular 2” mirror mount (model: *Radiant Dyes* MXI-2-3030) where the provided fine-thread screws were replaced by piezo driven screws ("piezo mikes", model: *Physikinstrumente* N-470.210 with E-870.4G driver), which move forward in discrete steps of $d_{\mathrm{mike}} = 20\,\mathrm{nm}$ length. After performing N_{steps} piezo mike

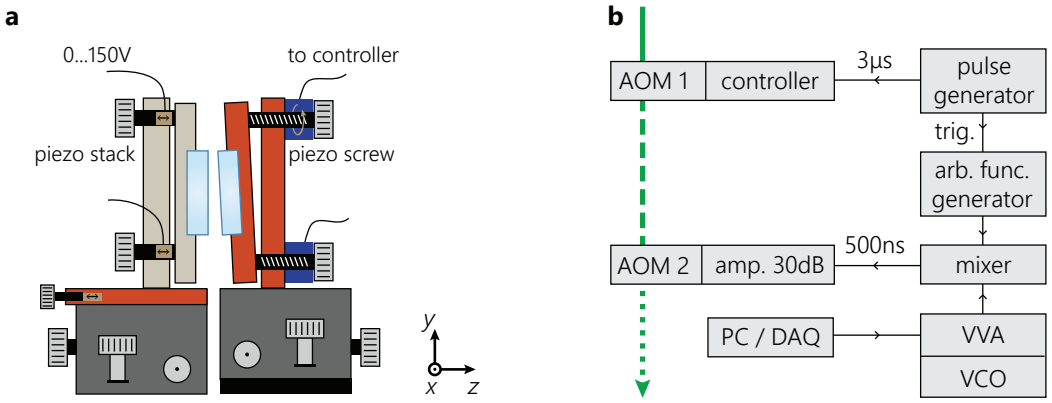

Fig. 4.4: a) Piezo-aligned cavity mirror holders fixed on 3D translation stages, left side with additional piezo assisted fine adjustment. Both mirrors are mounted on 2" mirror mounts, each adjustable manually and with piezo technology. Left: Continuous piezo stack; Right: Discrete step piezo screws. **b)** RF electronics for the two AOMs and pump laser beam chopping scheme.

steps, the resulting tilt angle α_{tilt} of the mirror translates into a separation difference ΔD_{tilt} at the box edges of

$$\Delta D_{\text{tilt}} \simeq \alpha_{\text{tilt}} L = \frac{N_{\text{steps}} d_{\text{mike}}}{L_{\text{mount}}} L \tag{4.5}$$

where L_{mount} is the separation of screw threading and mirror mount pivot point. For $L = 40\,\mu\text{m}$ boxes we get $\Delta D_{\text{tilt}} \approx 13\,\text{pm}$ per step which lies below the previously mentioned upper limit. It turns out that the discrete piezo actuators typically offer sufficient alignment precision.

In this series of measurements, the cavity cutoff wavelength can not be stabilized by helium neon laser interference as the mirrors don't have spherical geometry and thus no Newton ring pattern forms. Instead, the cutoff wavelength lock is achieved by monitoring of the cavity emission spectrum (cutoff wavelength) and feedback adjustment of the piezo voltage.

Illumination of the cavity with an LED ($\lambda_{\text{center}} \approx 620\,\text{nm}$) allows for alignment of the mirrors such that the position of the desired delaminated structure can be moved onto the optical axis into the field of view of the imaging path.

4.2.2 Pump Source and Pulse Pattern

The pump light source is a diode pumped solid state laser (model: *Spectra Physics* Millenia eV 15) at $\lambda_{\text{p}} = 532\,\text{nm}$ with a maximum output power of 15 W, power stability of ±1 % and <0.04 % rms noise [134]. In the following measurements, the dye-photon system is driven above condensation threshold, where momentary pump beam powers of around 100 mW are necessary. If not otherwise mentioned, the pump spot size is slightly larger than the currently investigated box size. Due to bleaching effects, the dye can not be pumped continuously at this power as it would degrade in a matter of milliseconds. Therefore, two AOMs are employed to chop the continuous wave laser emission into 500 ns pulses, which is much longer than the maximum cavity storage time of 250 ps and hence provide quasi continuous conditions. The radio frequency (RF) electronics used for temporal pump beam modulation are schematically depicted in Fig. 4.4b. The first AOM with dedicated driver electronics (model: *Gooch Housego* I-M110-2C10B6-3-GH26 with A35110-S-1/50-P4K7U driver) is directly gated by the pulse generator and chops out a 3 µs window from the continuous wave pump laser beam. The second AOM is driven by separate RF components. To begin with, a voltage controlled oscillator (VCO) creates a fundamental 110 MHz sine wave. A voltage variable attenuator (VVA) attenuates the signal according to an applied voltage of 0 V to 5 V from the PC/DAQ. An arbitrary function generator (AFG, model: *Tektronix*

AFG3252, 240 MHz bandwidth) is simultaneously triggered by the pulse generator to output a rising 500 ns long rectangular pulse to compensate for residual intra-pulse photobleaching effects. Both the attenuated continuous VCO wave and the AFG signal are fed into a frequency mixer, which multiplies the continuous RF wave with the linear ramp envelope signal. After amplification, the signal is fed to the second AOM which cuts out the desired pump pulse pattern from the initial 3 µs window. The repetition rate is 30 Hz.

The pump spot diameter inside the cavity is adjusted via displacement of lens L1 to be slightly larger than the currently investigated box potential whereas the position can be manually fine-tuned using the adjuster screws on the final mirror mount with micrometer precision.

4.2.3 Analysis Part

The concept of the analysis part is almost identical to the one in chapter 3 (Fig. 3.1) with major differences mostly in the optical paths. In the first image plane a rectangular slit with four independently adjustable edges is used. It turns out that it is necessary to restrict the region of interest to closely match the photon cloud as residual dye fluorescence from the surrounding area, which does not originate from the investigated potential, scatters into the box region. Spatial image and momentum space (k-space) are both imaged onto the EMCCD. The detected space is switched by flipping the corresponding lenses with focal lengths chosen such that both image planes coincide at the camera sensor.

Due to the smaller observed spectral range, a grating with 1200 grooves / millimeter is used for higher angular dispersion (model: *Thorlabs* GR50-1205). The ICCD camera serves as a suitable detector here. The grating can be replaced by an echelle grating (model: *Thorlabs* GE2550-3263) which is optimized for high diffraction orders allowing for a resolution down to the GHz regime despite their low groove density (316 grooves / mm). To block scattered pump light and free fluorescence in the red wing of the dye emission spectrum, the spectral region is limited to $550\,\mathrm{nm} < \lambda_{\mathrm{out}} < 600\,\mathrm{nm}$ with edge pass filters.

The experiment control for camera settings, pump beam power, piezo screws, cutoff wavelength lock and data acquisition uses self-written software. Raw data is here typically present in the form of camera images.

4.2.4 Photon Number Calibration

The following measurements rely on measurements of absolute intracavity photon densities, hence it is necessary to calibrate the setup, including the cavity mirror and objective transmittance and to deduce a camera-signal-to-photon conversion factor.

We employ the EMCCD camera, see sec. 3.1.3 for the working principle. The well reproducible acquisition settings allow for a one-time calibration which can be used throughout the project. Typical settings are pre-amp gain 3, horizontal shift speed 10 MHz, EM gain 20. For the measurement we directly illuminate the camera with a chopped 50 ms pump laser pulse at constant power, which contains a well-defined photon number. The laser beam path is merged with the imaging path right before the 2D slit and the power (measured with photodiode) is corrected for losses by optical elements in the path. The integrated camera signal count is divided by the photon number in the laser pulse $N_{\mathrm{calib}} = \int_0^\tau P(t)/\hbar\omega \,\mathrm{d}t$, which for the given camera settings yields a sensitivity of

$$\tilde{\eta}_{\mathrm{cam}} = 4.41(31)\frac{\mathrm{counts}}{\mathrm{photon}} \tag{4.6}$$

It is close to the value that can be obtained from the manufacturer calibration data using the product of EM gain G and sensor quantum efficiency η divided by the electron to voltage conversion

factor of the analog to digital converter η_{ADC} [135]

$$\tilde{\eta}_{\mathrm{cam,datasheet}} = \frac{G\eta}{\eta_{\mathrm{ADC}}} = \frac{20 \times 0.97}{4.84} = 4.01 \quad . \tag{4.7}$$

There is no information available regarding the uncertainty of the data sheet values.

Conversion from the pixel count C_{px} to the actual photon density in the cavity n requires further quantitative values from the experiment. The cavity region which is imaged onto a single pixel area $A_{\mathrm{px}} = (16\,\mu\mathrm{m})^2$ is given by the magnification M of the imaging setup. Further, the ratio between cavity round trip time $\tau_{\mathrm{round}} = 2D_0/\tilde{c} = q\lambda_c/c$ and pump pulse length τ_{pulse} convert the integrated signal into a momentary value. Finally, with the transmission T_{opt} of the optical setup (here cavity mirror, objective lens and longpass filter as other components are already included in $\tilde{\eta}_{\mathrm{cam}}$) one can compute the intracavity photon density at the position of a certain pixel via

$$n = \frac{M}{A_{\mathrm{px}}} \frac{C_{\mathrm{px}}}{\tilde{\eta}_{\mathrm{cam}}} \frac{20}{G} \frac{\tau_{\mathrm{round}}}{\tau_{\mathrm{pulse}}} \frac{1}{T_{\mathrm{opt}}} \tag{4.8}$$

$$N = \int_{\mathrm{ROI}} n(x,y)\,\mathrm{d}x\,\mathrm{d}y = \sum_{\mathrm{ROI}} n_{\mathrm{px}}\,A_{\mathrm{px}} \tag{4.9}$$

where in the last step the total photon number N in a certain region of interest (ROI) is obtained by summation of the pixel values. Since $\tilde{\eta}_{\mathrm{cam}}$ was measured for $G = 20$, $\tilde{\eta}_{\mathrm{cam}}$ can be scaled for other gain settings.

The major contribution to T_{opt} comes from the resonator mirror transmittance T. In the regime of $T \lesssim 10^{-5}$ the actual transmission of a dielectric layer stack often shows deviations from their theoretical value, typically towards lower transmission. This can be attributed to the accumulation of scattering and absorption losses that occur on every material interface as typically 30 or more dielectric layers are required to realize such low transmission. This circumstance is difficult to quantify in calculations (and hence often ignored) as the material properties differ in every coating run. The camera-facing mirror here is the "LO2019" custom mirror (see Fig. A.3), which employs 74 layers. Experimentally we find for the transmission $T_{\mathrm{LO2019}}(\lambda = 583\,\mathrm{nm}) = 1.2(3) \times 10^{-6}$.

4.3 Emission Characteristics

We start by probing the basic characteristics of the optical quantum gas trapped in a box potential. This includes the mode structure and the stationary properties of the photon gas such as spatial and momentum profiles as well as the corresponding spectral distributions for pump beam powers below and above condensation threshold.

4.3.1 Energy Levels

First, we probe the eigenenergies of a $L = 40\,\mu\mathrm{m}$ box potential. By recalling

$$E_{n_x,n_y} = \frac{\pi^2\hbar^2}{2mL^2}(n_x^2 + n_y^2) \qquad \text{with} \qquad n_{x,y} = 1, 2, \ldots \tag{4.10}$$

we expect energies to be integer multiples of $\pi^2\hbar^2/2mL^2 \approx 2\pi\hbar \times 6.5\,\mathrm{GHz}$. Due to the quadratic scaling with the mode number the first excited mode lies around $E_{21,12} - E_{11} \approx 2\pi\hbar \times 20\,\mathrm{GHz}$ above the ground state energy E_{11}, which gives an estimate of the required spectrometer resolution to detect individual modes. To create a measurable signal, the pump beam size is reduced below the box size and the intensity is cranked up such that multiple modes surpass the lasing threshold. By steering the pump spot across the box, different transverse modes are excited due to the varying

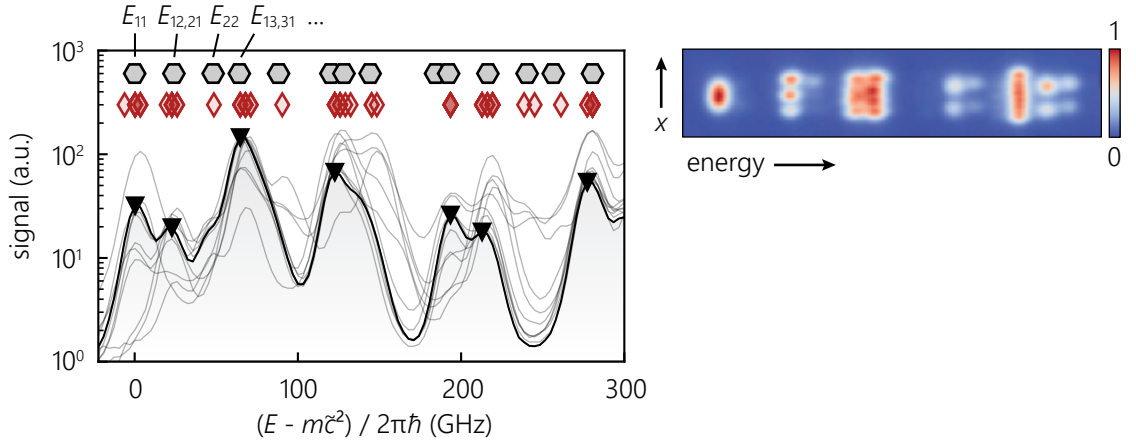

Fig. 4.5: High resolution spectrum of the transverse mode structure in a $L = 40\,\mu\text{m}$ box potential. Each thin graph shows an individual spectrum with different occupied modes. Black triangles mark identified peaks. Red diamonds show resonance frequencies for different subsequent recordings (gray). They well match theory values for a $L_{\text{eff}} = 36.4\,\mu\text{m}$ box (gray hexagons). The image on the right shows an exemplary single shot raw data. Spatial information is contained in the vertical dimension of the plot, which reveals the increasing number of wave nodes. The extent in the horizontal region is attributed to the finite resolution of the grating spectrometer.

spatial overlap of excited molecules and the mode functions allowing for a rough investigation of the mode structure. To obtain a spectrum, an experimental difficulty has be overcome: The cavity cutoff wavelength is varying from shot to shot, which leads to frequency jitter of the spectral signal. Averaging (or long integration) of multiple subsequent images is hence not feasible as it blurs the spectrum. Instead, a series of short-exposure spectra is recorded and each individual spectrum is shifted along its frequency axis until it best matches the previous spectra, which allows to calibrate the energy scale and overlay the signals.

The data along with identified resonances are shown in Fig. 4.5. We find a resolution of $\delta\nu \approx 16\,\text{GHz}$ from the peak half width, thus most neighboring modes can be resolved. Each peak represents a certain mode which can be identified either manually or by a simple peak finding algorithm. From multiple spectra with varying excited modes (shown as thin graphs in the background), one can collect all found resonances which are depicted as red diamonds above the spectral trace. Gray hexagons indicate theoretical positions for a box with a side length of $L_{\text{eff}} = 36.4\,\mu\text{m}$ which reproduce the experimentally found values. The smaller effective box size arises from the finite slope of the box walls, see sec. 4.1. In the raw data image one can see that higher energy modes indeed exhibit an increasing number of wave nodes. All modes appear as a vertical bar since the real space slit was closed tightly to increase resolution. Analogous results have been obtained for an $L = 20\,\mu\text{m}$ sized box [136].

We see that the eigenenergies of the structured potentials agree well with theoretical predictions.

4.3.2 Spatial Profile

A homogeneous trapping potential is most clearly pronounced in the spatial distribution of a uniform photon gas inside the cavity. In theory, the density profile $n(x)$ is a summation over the individual contributions of the system eigenmodes $\psi_i(x, y)$ weighted by the Bose-Einstein distribution function $\bar{n}_{\mu,T}(E_i)$ as

$$n(x, y) = \sum_i |\psi_i(x, y)|^2 \, \bar{n}_{\mu,T}(E_i) \quad . \tag{4.11}$$

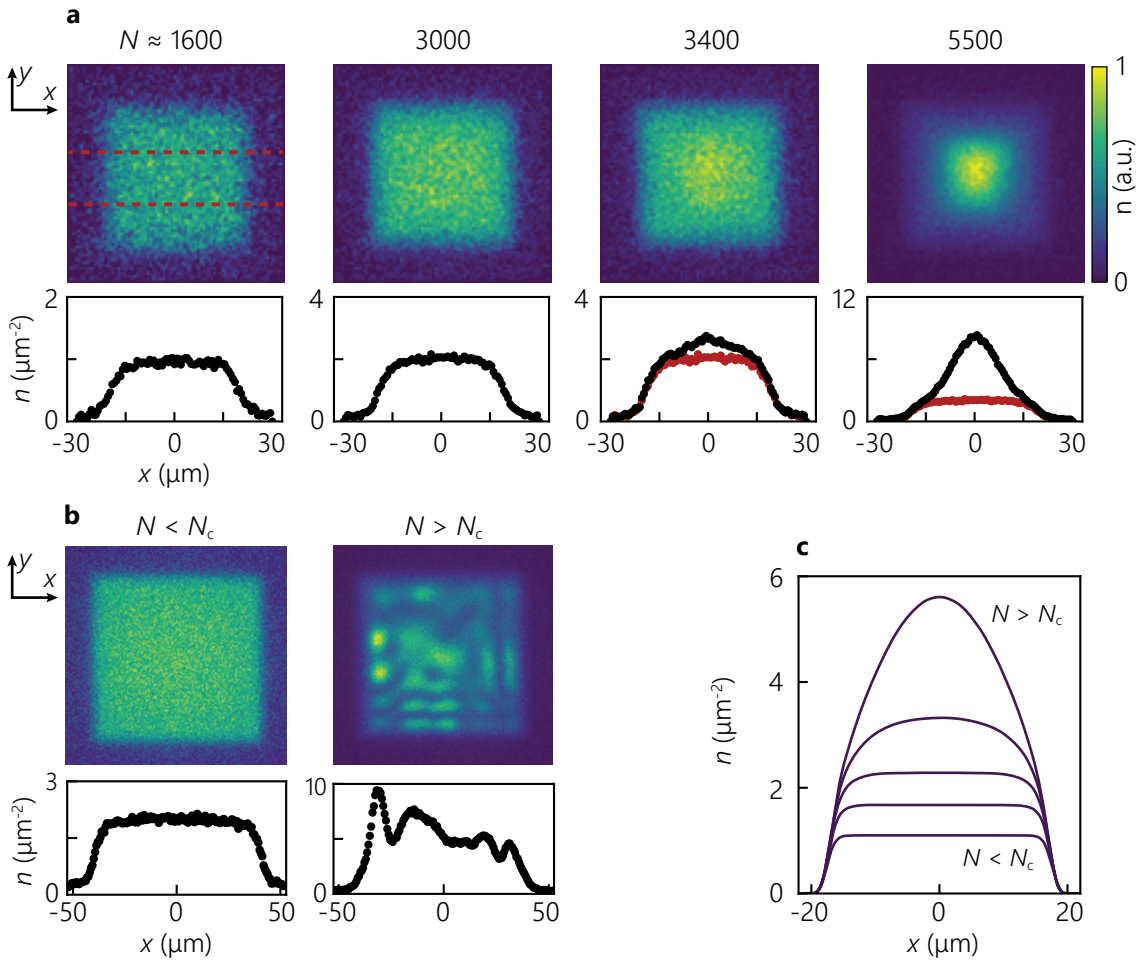

Fig. 4.6: a) Spatial density profiles emitted from a box potential structure ($L = 40\,\mu\text{m}$) at different intracavity photon numbers with their partially averaged line profile (region indicated by red dashed lines) cut shown below. A transition from uniform to inhomogeneous density profiles is visible as BEC sets in. The profiles in the two rightmost line profiles are the $N = 3000$ profile for visual comparison. **b)** Spatial surface density profiles in a box with $L = 80\,\mu\text{m}$ below and above threshold. The chaotic instead of the sinusoidal shape of the ground mode is attributed to the mirror surface roughness. **c)** Theoretical density cuts at different total particle numbers, computed for a box with $L = 40\,\mu\text{m}$ with soft edges (see sec. 4.1) and finite trap depth of $V_{\text{max}} = 1.4\,k_{\text{B}}T$ (see sec. 4.4).

Theoretical profiles are shown in Fig. 4.6c for a box with side length $L = 40\,\mu\text{m}$ for different total photon numbers N. Below threshold ($N < N_{\text{c}}$), the density distribution is expected to be uniform. However, upon emerging quantum degeneracy for $N \gtrsim N_{\text{c}}$, a central peak starts to emerge because the low energetic modes, especially the sinusoidal ground mode, give dominant contributions in the central region. To give realistic input to the computation (sec. 2.3.2), the potentials have finite height like the experimental profiles (Fig. 4.2) and the edges are smoothened via convolution with a Gaussian of width $\sigma \approx 1.3\,\mu\text{m}$, which quite well resembles the height profiles measured by Mirau-interferometry.

Experimentally, we observe the spatial density profile of the dye-microcavity emission from the box region ($L = 40\,\mu\text{m}$) for different pump beam powers and hence varying intracavity photon numbers; The false color images along with averaged horizontal cuts through the density profile are shown in Fig. 4.6a. The profiles match the expectations of a thermalized photon gas in the box. For low pumping powers, i.e. $N \ll N_{\text{c}} \approx 3500$ photons, the density profile is uniform as verified in the line profile (bottom). Deviations from uniformity start to emerge if the photon

number reaches N_c. For comparison, the $N = 3000$ line profile (red) is plotted next to the higher N profiles as well for better direct visual comparison. In the condensed regime $N \gg N_c$ the sinusoidal box ground mode dominates the density profile with the uniform background still visible. Most measurements are here restricted to boxes with a maximum of $L = 40\,\mu\text{m}$ design side length since the potential bias of the surface roughness severely disturbs the ground state wave function in larger systems, see Fig. 4.6b. Here, the gas is also uniform below threshold. Above N_c, however, it becomes random, owing to the perturbed shape of the lowest lying states. Nevertheless, 80 µm sized boxes are still useful for the determination of the equation of state (sec. 4.7), as the ground state energy of a tilted box lies energetically higher due to the stronger confinement of a corresponding potential with the linear gradient.

Threshold Behavior

Contrary to a harmonically trapped quantum gas, the critical particle number N_c is not well-defined thermodynamically in the homogeneous environment. However, using coherence arguments one may derive an analytic expression (see sec. 2.4.2)

$$N_{c,box}(L) \simeq \frac{L^2}{\lambda_{th}^2} \log\left(\frac{L^2}{\lambda_{th}^2}\frac{4\pi}{1+2\pi^2}\right) \tag{4.12}$$

$$\propto L^2 \log(L) \quad . \tag{4.13}$$

Exemplary numeric values for $L = \{36, 40\}\,\mu\text{m}$ and $\lambda_{th} \approx 1.47\,\mu\text{m}$ are $N_{c,box} \approx \{3500, 4500\}$, indicating that slight variations of the effective box size have immediate effect on the expected critical photon number.

With the current experimental setup a measurement of the transverse coherence length is not possible, hence we use as a figure of merrit the inhomogeneity of the spatial surface density profile that arises from the sinusoidal shape of the ground mode. The degree of inhomogeneity can be quantified by the ratio of central density n_0 and total particle number N. The data is obtained from images as shown in Fig. 4.6 and plotted in Fig. 4.7a. As expected for $N < N_c$, where the photon gas is spatially uniform, the ratio is constant since the density is approximately given by $\bar{n} \approx N/L^2$. Around the threshold region, the graph ratio increases and slowly approaches the limit value of 4, as expected from the squared amplitude of the ground mode wave function $|\psi_{11}(x,y)|^2 = 4L^{-2}\cos^2(k_x x)\cos^2(k_y y)$ which dominates the spatial profile for $N \gg N_c$ as compared to the uniform gas yielding a normalized density of 1. As indicated in the figure, the threshold region around N_c is obtained by determination of the rising point which here is around $N = 3100(300)$ in accordance with the value obtained from (2.62) for a box with effective size $L = 36\,\mu\text{m}$. As discussed in section 4.4 a slightly lower value is actually expected since the trapping potential does not contain modes with arbitrary high momentum. An adjusted formula (omitting states with $E_i > V_{max}$) typical yields a critical particle number roughly 10 % below. The solid theory curve in the plot already contains the finite trap depth. Experimentally we are limited to a certain maximum occupation of the ground mode as for even higher pump powers, laser-like amplification of additional excited modes sets in ([105, 137]), which distorts the density profile and causes the data points to drop again at large N. Further measurements are always operated below this onset point of around $N \approx 10\,000$ photons.

As a sidenote, the here used theory does not take a polarization degeneracy factor of 2 into account. As a first argument, the agreement of the data and fully polarized theory hints at this behavior. In fact, our measurements confirm that for $N \ll N_c$ the photon cloud is unpolarized, whereas the ground mode is always fully polarized as soon as the system condenses which supports the decision to here leave out the additional degeneracy factor. Earlier works did not report about this behavior [22, 122], however, their employed cavity mirror transmission and hence the intracavity photon number were typically not corrected for the influence of the dye medium

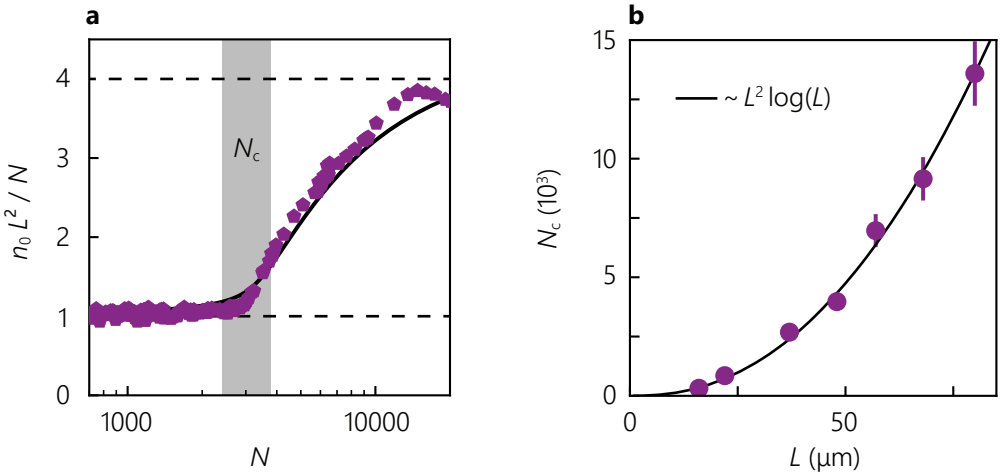

Fig. 4.7: Threshold behavior. **a)** Central density n_0 divided by total photon number N, normalized to box area L^2. The critical photon number for condensation N_c is determined from the onset region where the ground mode starts to dominate the intensity profile. The solid line is a numerical prediction including finite trap depth. **b)** Scaling of N_c with the box size L. A fit function $f(L) \propto L^2 \log(L)$ (solid line) agrees with the expected scaling.

($T_{dye} \approx \tilde{n} T_{air}$, see sec. A.1), which would then also yield N_c values close to the predictions for non polarization degenerate systems. The polarization axis of the mode was found to be horizontal and aligned with the pump beam polarization (also observed in [138], see also [139]) which might induce fluorescence polarization [70]. The latter occurs when the molecular dipoles diffuse on time scales longer than the fluorescence time which is greatly reduced in a stimulated emission dominated regime.

Scaling with Box Size We now investigate N_c as a function of the box side length L. Following the quantum prediction (2.62) one expects a scaling $N_c \propto L^2 \log(L)$. A numeric approach based on spatial profiles with theory curves as in Fig. 4.7 and consecutive determination of the threshold region yields the same scaling.

Although the intensity profile above condensation threshold is strongly distorted in boxes with $L \gtrsim 50\,\mu m$ (Fig. 4.6b) one can nevertheless try a similar method as the one used for smaller sized boxes. Instead of the geometric center of the box one can either define n_0 as the mean density in an extended central region of the box or manually define the position of the first arising density peak as the position of n_0. It turns out both methods yield comparable results. For all boxes their effective size is determined by probing the width of their flat density profile below threshold. The critical photon numbers are determined for boxes of design size $L = \{20, 30, \ldots, 80\}\,\mu m$ and are shown in Fig. 4.7b. A function fit of $f(L) = C \cdot L^2 \log(L)$ to the data points (solid line) agrees with the experimental data, when C is chosen as a free parameter. Note, that due to the perturbation of the lowest modes by the roughness induced disorder potential, the data has to be taken with care.

4.3.3 Momentum Distribution

The transition from the classical to the condensed regime can also be observed in k-space. For this purpose, the lenses before the detector can be rearranged (flippable optics) to projects the momentum space onto the detector, see sec. 1.6. The acquired data for various photon numbers is shown in Fig. 4.8a. Contrary to the spatial distribution, which follows the box potential outline, the k-space distribution typically shows the same features which are only slightly modified by the trapping potential as the motional degrees of freedom remain unchanged.

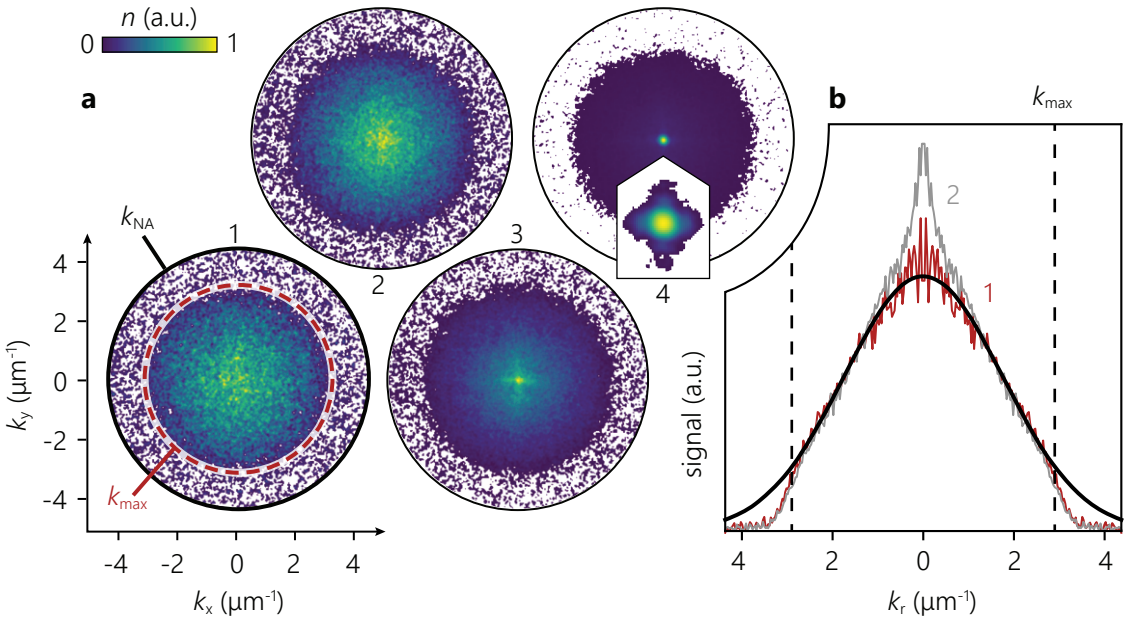

Fig. 4.8: Momentum space. **a)** Images in k-space for $N_{1,2,3,4} \approx \{0.5, 0.75, 1, 1.25\} \times N_c$ around the threshold particle number N_c in a $L = 40\,\mu\text{m}$ box. Each colormap is adjusted to the individual intensity. The transition from a purely Gaussian (see b)) to a bimodal distribution is visible. The inset shows a contrast enhanced image of the ground mode (sinc-function) with its first side wings. The limit $k_{max} = (2mV_{max})^{1/2}/\hbar$ (cf. sec. 4.4) indicates the finite trap depth and k_{NA} the maximum detectable amplitude of $|\boldsymbol{k}|$. **b)** Radially averaged k-distribution (red) with occupation like in panel 1 on a) with a Gaussian fit (black). The k-axis is mirrored around 0 for better visibility. For comparison, a trace from panel 2 is shown (gray) where degeneracy starts to emerge. Dashed lines mark the trap depth limit.

In the classical regime we expect a radially symmetric momentum distribution with Boltzmann scaling

$$n(\boldsymbol{k}) \propto \exp\left(-\frac{\hbar^2|\boldsymbol{k}|^2}{2m\,k_B T}\right) \tag{4.14}$$

where the scaling is identical for the individual components due to $k_r^2 \equiv |\boldsymbol{k}|^2 = k_x^2 + k_y^2$. Indeed, the classical expectation is confirmed as seen in Fig. 4.8b, where the radially averaged k_r-distribution is shown. Function fits of (4.14) (solid black line) onto the wings of multiple traces like in the shown data confirms the Gaussian character and yield

$$T = 306(19)\,\text{K} \tag{4.15}$$

where the error is the standard deviations of multiple obtained fitting parameters. The increased noise around $k_r = 0$ arises from the low number of points in the radial averaging process. For comparison, a distribution corresponding to panel 2 is shown (downscaled by factor 1.5) in gray where quantum degeneracy in the low momentum states begins to emerge. For higher photon numbers, a peak around $k_x, k_y = 0$ emerges, which corresponds to the sinc(k) shaped resonator ground mode, see (2.36).

Notably, the photon gas experiences a high momentum cutoff at $|\boldsymbol{k}| > k_{max} \approx 2.9(2)\,\mu\text{m}^{-1}$, which is here attributed to an experimental limitation of the trap depth. The observed upper limit lies within the resolvable angular range k_{NA}, hence we assume the limitation to be an intrinsic property of the structured mirrors; the circumstance is further discussed in sec. 4.4.

The data so far confirms the expected momentum space behavior across the phase transition. Further spectral measurements regarding the caloric properties are presented in sec. 4.5.

Ground Mode Uncertainty

The ground state intensity is a squared sine (x-space) or sinc (k-space) function, respectively, which are similar to Gaussian functions until their first minima. The latter show minimal position-momentum-uncertainty in the form $\sigma_x\sigma_k = \frac{1}{2}$ where $\sigma_{x,p}$ are the corresponding standard deviations. Using (2.32) and (2.36) one gets for the expected uncertainty of a given mode of order n

$$\sigma_x\sigma_k = \frac{1}{\sqrt{12}}\sqrt{\pi^2 n^2 - 6} \tag{4.16}$$

$$\overset{n=1}{\approx} 0.57 \tag{4.17}$$

which, for the ground state ($n = 1$), is slightly above the Heisenberg limit. From the acquired traces for the respective highest photon number as seen in Fig. 4.6 and Fig. 4.8 we find that Gaussian fits are nevertheless well-suited to determine the uncertainties in x and k. We get

$$\sigma_x\sigma_k = 0.7(1) \tag{4.18}$$

which is slightly above the theoretical value. A deviation towards larger values is plausible due to the finite resolution capabilities of the imaging apparatus and non-perfect subtraction of the thermal floor when extracting the ground mode. Still, the finding continues to confirm the well-defined mode structure in the box potential.

4.3.4 Spectral Distribution

We measure the energy distribution $n(E)$ in-situ in a $L = 40\,\mu\text{m}$ box with a diffraction grating, as obtaining the spectra from momentum space images raises signal-to-noise issues at low photon numbers. The spectral resolution is of order $\delta\lambda \approx 1\,\text{nm}$.

To record the data, the light is guided onto the diffraction grating which is placed in the momentum Fourier plane of a lens. The dispersed light is then imaged on a camera with another lens, which then effectively measures in real space with every mode being shifted according to its wavelength. It is here important to close the rectangular slit such that only the box emission passes through the aperture, as otherwise residual fluorescence of excited dye molecules outside of the box region disturb the measurement. Exemplary cavity emission spectra recorded at different total photon numbers N are shown in Fig. 4.9. Below threshold, the occupation is Boltzmann-like and follows an exponential behavior indicated by the black bar. As N approaches N_c from below, quantum degeneracy emerges in the low energetic modes, as manifested in their overpronounced occupation until above N_c, a spectral peak from the macroscopically occupied ground mode emerges accompanied by a small degeneracy of the low lying excited modes while the thermal tail of the spectrum shows signs of saturation. The agreement of experimental and theoretical spectra (inset, for same N/N_c) allows in further studies to assume Bose-Einstein like occupation of modes.

As the spectra are integrated over a full pump pulse, the data has to be corrected for the wavelength-dependent mirror transmission to obtain the circulating power inside the resonator. In the finite size box potential landscape, the energy can be mapped onto a specific emission angle through the mirror coating. Hence, following the calculations from sec. A.1, one can precompute a suited transmission profile taking into account wavelength and emission angle. The measured spectra are then corrected by this factor.

Due to the high-k cutoff in the trap as already hinted at in section 4.3.3, the spectra are only shown until the trap depth limit. A more elaborated measurement to characterize V_max is presented in the following section 4.4.

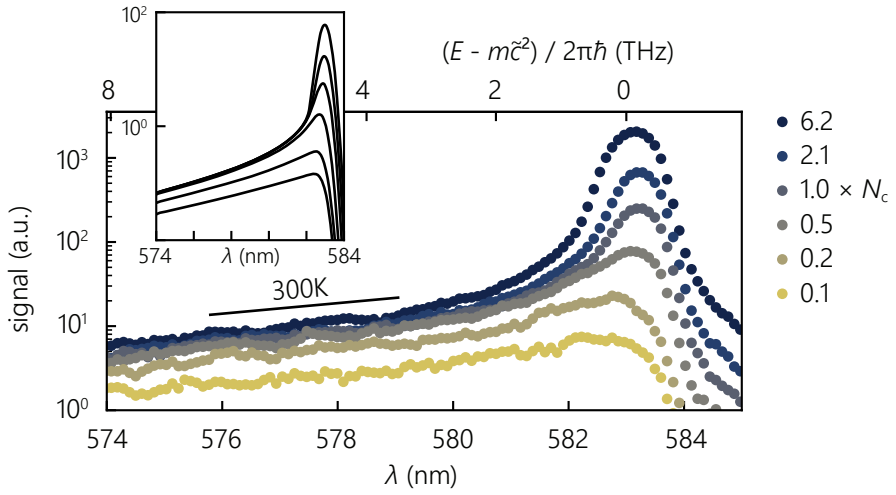

Fig. 4.9: Spectral distribution of the photon gas for different circulating powers in the resonator, normalized on the critical photon number N_c. Black solid line section hints at the slope of a thermal exponential decay for $T = 300\,\mathrm{K}$. The inset shows theory spectra for the same N/N_c which are blurred to simulate finite resolution.

4.4 Finite Trap Depth

The abrupt high-k cutoff around $k_r \approx 2.9(2)\,\mu\mathrm{m}^{-1}$ shown in Fig. 4.8 goes along with a drop in the spectral distribution measured with the diffraction grating. This truncation effect has been observed in all investigated structures during this work which should in principle, inferred from their mechanical elevation height of the barrier, provide a deeper trap. With the here used 30 nm thick silicon layer, delamination heights of up to 60 nm are possible [59, 124, 125]. The elevation height translates into a maximum trap depth like

$$V_{\mathrm{max}} = 4\pi\hbar \frac{c_0 \tilde{n}}{\lambda_c^2} \frac{\Delta D_{\mathrm{max}}}{q} \tag{4.19}$$

which for $q = 7, \lambda_c \approx 580\,\mathrm{nm}$ predicts a theoretical maximum trap depth of $V_{\mathrm{max}} \approx 3.5\,k_B T$. Next, we vary q and determine the spectral width of the emission to systematically probe the trap depth. Experimentally, the system is prepared at $q \approx 7$ or 8 and a spectrum is acquired. By decreasing the applied voltage of the piezo crystal in the translation stage, the cavity mirrors are moved apart until, after a translation of $\lambda_c/2\tilde{n}$, the same cavity cutoff wavelength is set with $q \to q + 1$; from here, the process is repeated and a spectrum is recorded for each setting. In this way, spectra can be recorded with different trap depth using the same microfabricated mirror sample, yielding one mechanical box depth. The experimentally determined trap depth from the spectra versus the longitudinal mode number q are shown in Fig. 4.10 for three different mechanical box depths ΔD_{max}. In the amplitude normalized spectra, a change of the spectral width is apparent. The criterion for the high energy cutoff (*not* the cutoff wavelength λ_c, dashed line) is chosen as the point where the amplitude drops below a certain percentage of its maximum value (black dots). The spectra in panel a) were obtained in a 35 nm deep structure, which for $q \leq 11$ qualitatively look identical as all cutoffs coincide in the same region. In fact, as long as the spectral width is below a certain value, one can confirm the expected $1/q$ behavior of the trap depth (solid black lines). For the 15 nm deep potential, the spectral width follows the expected behavior as it never reaches the otherwise observed maximum value. The transition is most apparent for the 35 nm and 51 nm high structures. While the trap depth follows the $1/q$ scaling at large q, they saturate at a value of $V_{\mathrm{max}} = 1.4(2)\,k_B T$. The uncertainty is estimated from the not well-defined definition of the trap depth, as there is no visible hard high energy cutoff in

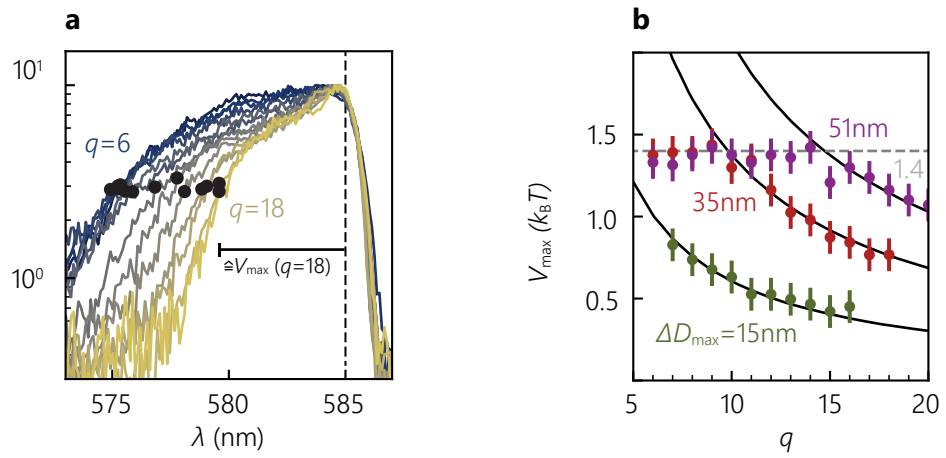

Fig. 4.10: Determination of the trap depth $V_{\max}$. **a)** Spectrum of the cavity emission from inside a 35 nm high box structure. The trap depth is determined as the energy separation between the cutoff wavelength (dashed line) and the threshold intensity of the spectrum (black dots) on the wavelength scale. **b)** Determined trap depths from the spectra in a) for different physical box structure heights. Horizontal dashed line at $1.4\,k_BT$.

the spectra. Additionally, there seems to be a smooth transition of the light originating from the box and residual fluorescence from the potential border (delaminated region, see Fig. 4.2). Most of the straylight can be blocked with the rectangular aperture, but the blocking region can also have a small impact of order $0.1\,k_BT$ onto the measured trap depths. The $V_{\max}$ value is chosen to stay consistent with the already shown high-k cutoff in Fig. 4.8 and observations made in the following sections. The here determined trap depth of $V_{\max} = 1.4\,k_BT$ has to be accounted for in the theoretical expectations of all following measurements as it has direct consequences on thermodynamic quantities and spatial profiles.

Contrary to experiments with ultracold atomic gases, where the cloud is cooled by controlled lowering of the trap depth allowing the most energetic particle to escape ("evaporative cooling", [140]), the truncated trap here has no visible effect on the remaining part of the spectrum as the temperature is set by the dye molecular heat bath.

Possible Explanation The origin of the potential depth saturation despite rising structure height is presently, as of this writing, not fully understood. As inferred from the correct q-scaling, the structures appear to be physically intact up to their full height. The trap depth is found to be independent of the cutoff wavelength λ_c, hence occurring local transmission maxima in a certain spectral region can be ruled out as a cause. In previous works, the mirrors have been thoroughly investigated with respect to their reflective and transmissive properties in their raw form as well as in their delaminated regions [59, 110, 125, 126]. Below their physical desintegration threshold, there is yet no evidence that a diminishment of their reflectance in this region could explain a hard cutoff in the light trapping capabilities. A trapping potential comprised of two opposing delaminated mirrors does also saturate at the same observed limit, which indicates that the limiting cause is not to be found in the structures themselves. However, the delaminated regions remain to be investigated at their edges (slope regions), which thus remain as a trap depth quenching candidate. As in those regions the material stresses are probably the highest and their impact on the optical properties (e.g. refractive index) could be severe. Recalling that a momentum cutoff corresponds to a maximum allowed propagation angle inside the resonator, light propagating at larger angles might be subject to an additional yet unidentified loss channel. Further quantitative investigations have not been performed.

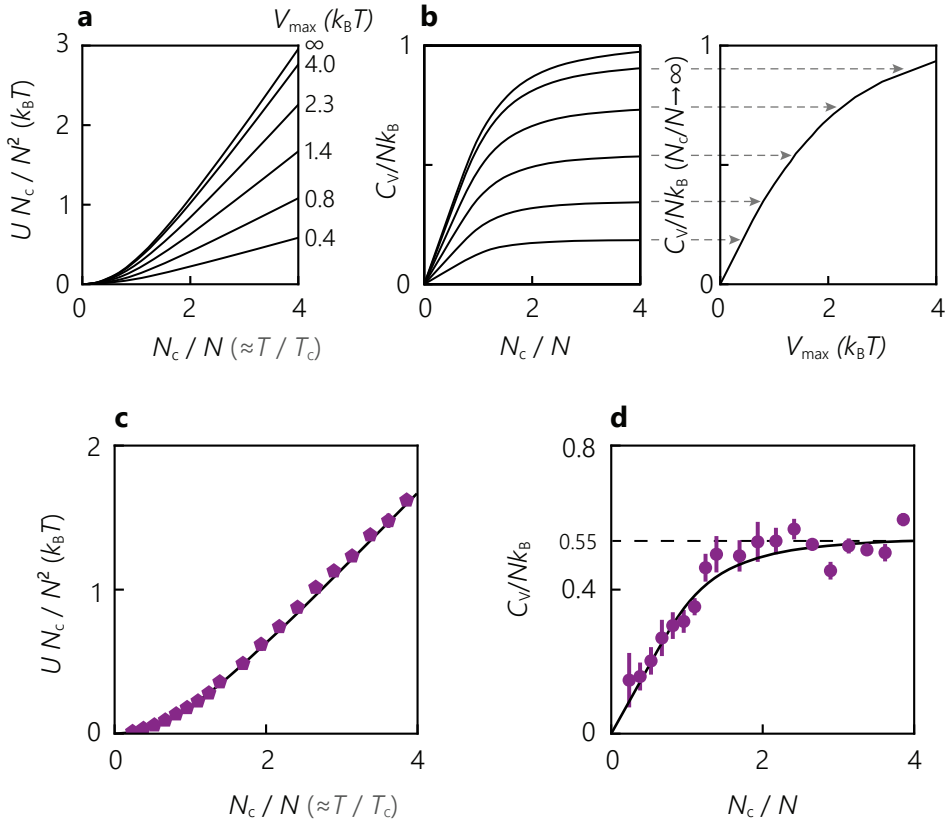

Fig. 4.11: Calorimetry of the two-dimensional homogeneous photon gas in a finite depth trap. **a)** Numerical predictions for the internal energy per particle versus normalized inverse particle number. The finite trap depth significantly alters the temperature behavior. **b)** Derivative of the internal energy expression, resembling to the specific heat, which is similarly affected by the finite trap depth. Graph labels from top to bottom as in a). The high-(N_c/N) limits is shown in the right panel. **c)** The internal energy U transitions from a quadratic scaling ($N > N_c$) to a linear scaling ($N \ll N_c$) without a discontinuity. The same also holds for the derivative in **d)**. The specific heat approaches zero in the condensed regime and saturates at a value of $0.55\,k_B T$ (dashed line) in the classical phase due to the finite potential depth. The solid lines are finite depth numeric predictions.

4.5 Calorimetry

The photon gas spectra given in sec. 4.3.4 enable the investigation of the caloric properties of the homogeneously trapped photon gas across the phase transition. Similar measurements in the dye-microcavity system have previously been carried out for harmonic traps [61]. We measure the internal energy and compute its derivative as a function of the (threshold normalized) particle number, which yields a quantity closely related to the specific heat, see sec. 2.4.2. Other than in the harmonic case we don't expect any discontinuities in both quantities as the finite two-dimensionally trapped Bose gas is not predicted undergo a second order phase transition upon turning into a condensate. To be consistent with experimentally acquired values, we take the normalized inverse particle number N_c/N as an order parameter, which is related to the reduced temperature T/T_c typically used in quantum gas experiments apart from small logarithmic corrections (see sec. 2.4.2). The two-dimensionally trapped homogeneous Bose gas with its kinetic components $p_{x,y}$ only has $f = 2$ degrees of freedom. In the classical regime, the internal energy U is hence given by $U = \frac{f}{2} N k_B T = N k_B T$, which scales linear with the particle number N. As we cool down the system or, in our case, increase N at constant T, additional particles eventually populate the ground state after surpassing BEC threshold, which does not contribute

to the internal energy, which hence ultimately saturates – the energy per particle approaches zero. The internal energy computes from the single particle state energies E_i as

$$U = \sum_i \bar{n}_{\mu,T}(E_i)\, E_i \tag{4.20}$$

where, due to the finite trap depth, $\bar{n}_{\mu,T}(E_i > V_{\max}) = 0$. For better understanding of the experimental results, numerically obtained values of energy per particle in units of $k_B T_c \simeq k_B T N/N_c$ are plotted against N_c/N for different trap depths as shown in Fig. 4.11a/b together with the corresponding derivative. A normalization of this kind gives the specific heat per particle. In the classical regime ($N \ll N_c$ or $T \gg T_c$), the internal energy U graph grows linearly with N_c/N. In the condensed regime, where the energy per particle approaches zero as the ground state does not contribute to the internal energy, the curve shows quadratic behavior as only the residual energy U_{sat} of the now quasi-saturated excited modes remains, $UN_c/N^2 \simeq U_{\text{sat}}(N_c/N)^2/N_c$. The influence of the finite trap depth is visible as it decreases the internal energy in the system, see Fig. 4.11a. While a trap with $V_{\max} = 4\,k_B T$ can still be regarded as nearly equivalent to the infinitely deep potential, the here present $V_{\max} = 1.4\,k_B T$ decreases the internal energy per particle in the classical regime $N_c/N \lesssim 1$ by a factor of ≈ 2.

Moreover, we investigate the derivative of U (panel b), which is related to the specific heat per particle

$$C_V = \frac{\partial U}{\partial T} \tag{4.21}$$

$$\frac{C_V}{N k_B} \simeq \frac{\partial (U N_c/(N^2 k_B T))}{\partial (N_c/N)} \quad . \tag{4.22}$$

The saturated internal energy in the condensed region causes a linear slope. The curve then flattens until it, without any discontinuities, approaches a plateau that represents the heat contribution of a single particle in an ideal classical gas. The plateau value again strongly depends on the trap depth: In the infinite 2D gas, a single particle would contribute one k_B of heat as expected for its two kinetic degrees of freedom. This value is reduced as high momenta are inaccessible by the gas particles. Its high-temperature limit is shown in the right panel of Fig. 4.11b showing how the classical heat capacity changes with the trap depth.

Experimentally, the internal energy is obtained by evaluating spectra such as the ones shown in Fig. 4.9. The Bose-Einstein distribution used in (4.20) is then replaced by the measured values $n_{\text{exp}}(E)$ and the signal is integrated following

$$U_{\text{exp}} = \int_{E_c}^{E_c + V_{\max}} n_{\text{exp}}(E) \times (E - E_c)\, \mathrm{d}E \quad . \tag{4.23}$$

The wavelength axis is accordingly converted into an energy axis that is shifted such that the low-energy cutoff E_c is set to zero, $E(\lambda) - E_c = 2\pi\hbar c_0(\lambda^{-1} - \lambda_c^{-1})$. The photon gas is prepared in a $L = 40\,\mu\text{m}$ box at a cutoff wavelength of $\lambda_c = 583\,\text{nm}$. By varying the pump power and continuous spectrum acquisition we record 250 spectra for photon numbers N between 0.1 and $5N_c$. The cavity is here intentionally not stabilized with the attached piezo crystal since it turned out that during the data acquisition period ($\approx 90\,\text{s}$) the cutoff wavelength is sufficiently stable (with rare manual corrections) as the feedback loop tends to overshoot due to the changing spectral profile at different photon numbers. After extracting U, the photon number is fitted by setting one trace to contain $N = N_c$ photons like in Fig. 4.9. The derivation of the internal energy is performed numerically and both data sets are binned. The obtained caloric quantities are shown in Fig. 4.11c/d and in good agreement with finite-depth predictions. According to the prediction, the specific heat does not show a discontinuity near N_c and saturates at the expected value of $0.55\,k_B$. We hence find the homogeneous photon gas to undergo the expected crossover from a thermal to a condensed state.

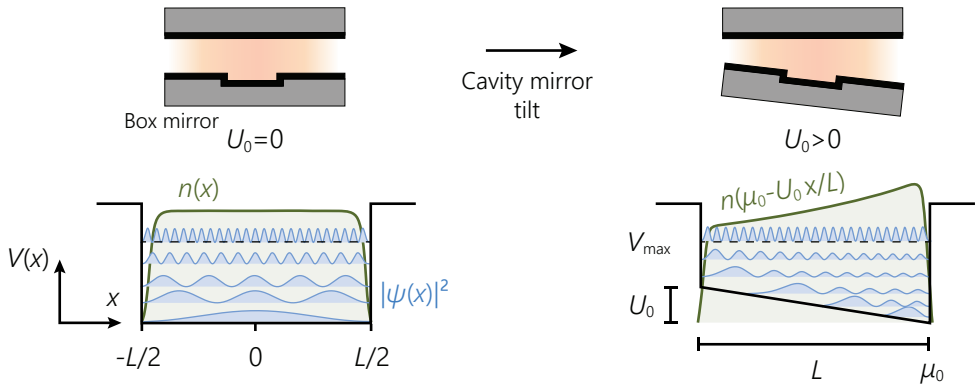

Fig. 4.12: Potential outline and wave functions for a tilted and untilted box. A tilted cavity mirror results in a linear potential gradient $U(x) = U_0/Lx$ that changes the local density of states, perturbing the steady state photon density $n(x)$ to become spatially inhomogeneous.

4.6 Box Potential with Linear Gradient

To probe the density response of a photon gas to external, well-controlled perturbations, the homogeneous trapping potential can be by superimposed with a linear potential gradient, realizing a weak constant force along e.g. x. The experimental concept is shown in Fig. 4.12. One of the cavity mirrors can be tilted in discrete steps with the piezo driven adjustment screws that tilt the cavity by 0.3 µrad per step, which corresponds to a potential difference of $\Delta U/k_\mathrm{B} \approx 0.2\,\mathrm{K}$ over a $L = 40\,\mu\mathrm{m}$ box. The difference ΔU scales linearly with L, see (4.5). The mechanical mirror tilt is temporarily static compared the resonator storage time ($\approx 200\,\mathrm{ps}$) or pump pulse length (500 ns) and is set prior to photon injection into the cavity. Response functions, such as κ_T are extracted from the changing steady state conditions of the resonator.

We reduce the problem to a single dimension x and transform the surface density to a line density via

$$\bar{n}(x) = \int_{-\infty}^{\infty} n(x,y)\,\mathrm{d}y \tag{4.24}$$

$$= n(x,y)\,L \tag{4.25}$$

where we assume that for sufficiently low densities below condensation, $n(x,y)$ is nearly uniform and the integral yields a factor L. We start with a substitution, where the x-axis will be transformed into a local chemical potential μ-axis with the local density approximation. We denote U_0 as the total potential energy difference over the box side length L and define

$$\mu \equiv \mu_0 - U_0\frac{x}{L} \tag{4.26a}$$

$$\mathrm{d}\mu = -\frac{U_0}{L}\,\mathrm{d}x \tag{4.26b}$$

which is used in the following to describe $n(x)$, (cf. sec. 1.3.1).

4.6.1 Expected Density Profile in a Tilted Box

The tilted box potential provides a calibrated energy scale, because the mirror is plane and both tilt and box size are well-measurable or known. Thermodynamic information is gained from spatial density profiles, where the position-dependent photon density reveals its response to the modified potential. In the infinite uniform system the surface density is expected to follow the

relation

$$N = \frac{mL^2}{2\pi\hbar^2} \int_0^\infty \bar{n}_{\mu,T}(E)\,\mathrm{d}E \tag{4.27}$$

$$n_\infty(\mu) = -\lambda_{\mathrm{th}}^{-2}\,\log(1-\exp(\mu/k_\mathrm{B}T)) \tag{4.28}$$

which is constant for a flat potential but here, where the potential energy is substituted by a local chemical potential $\mu(x)$, the equation describes the expected local surface density.

The before-mentioned finite trap depth in sec. 4.4 here has a more complex impact on the density profile. Due to the cavity tilt, the photon energy at the left edge of the box where $V(x) = U_0$ (see Fig. 4.12), the allowed energies have both a lower as well as an upper cutoff, rendering (4.28) inapplicable here as the mapping of local chemical potential to the corresponding photon density is biased. In analogy to (4.27) we make a new ansatz for the local surface density profile like

$$n(x) = \frac{m_\mathrm{ph}}{2\pi\hbar^2} \int_{V(x)}^{V_\mathrm{max}} \bar{n}_{\mu,T}(E)\,\mathrm{d}E \tag{4.29}$$

which is a reasonable approach as wave functions with $E_i < V(x)$ have no significant contribution to the local density, see Fig. 4.12. For $E_i > V(x)$, the wave functions start to behave similar to plane waves and the formalism of homogeneous systems can be applied again. Alternatively, one could also introduce a position dependency in the density of states $\bar{g}(x)$, which vanishes for energies $E < V(x)$ and keep the integral boundaries as before. From this circumstance we conclude that the slope of the density is actually not significantly affected by the finite trap depth, but rather an offset is subtracted from the unaffected density profile as seen in Fig. 4.14b where numerically computed density profiles are shown for fixed $U_0/k_\mathrm{B} = 50\,\mathrm{K}$, $\mu_0 = -3\,k_\mathrm{B}T$, but varying trap depths. The uniform reduction has higher impact in regions of lower density, i.e. the *relative* gradient $n^{-1}\partial n/\partial x$ is affected. Aiming for an analytic correction, we compare the densities at the box edges $n(\pm L/2)$ for each finite and infinite trap depth:

$$\mathcal{A}(V_\mathrm{max}, U_0, \mu) = \frac{1 - n_\mathrm{exp}(-L/2)\,/\,n_\mathrm{exp}(L/2)}{1 - n_\infty(-L/2)\,/\,n_\infty(L/2)} \tag{4.30a}$$

$$= \frac{1 - \left(\int_{U_0}^{V_\mathrm{max}} n_{\mu,T}(E)\,\mathrm{d}E\right) \Big/ \left(\int_0^{V_\mathrm{max}} n_{\mu,T}(E)\,\mathrm{d}E\right)}{1 - \left(\int_{U_0}^{\infty} n_{\mu,T}(E)\,\mathrm{d}E\right) \Big/ \left(\int_0^{\infty} n_{\mu,T}(E)\,\mathrm{d}E\right)} \quad . \tag{4.30b}$$

Far in the classical regime, where the Boltzmann-distribution serves a good approximation of the quantum statistics, the equation evaluates to

$$\mathcal{A}(V_\mathrm{max}) = (1 - \exp(-V_\mathrm{max}/k_\mathrm{B}T))^{-1} \tag{4.31}$$

$$\approx 1.33 \tag{4.32}$$

where the numeric value is calculated for our experimental trap depth of $V_\mathrm{max} = 1.4\,k_\mathrm{B}T$. When inserting a Bose-Einstein distribution to cover the quantum degenerate regime and above, the expression of $\mathcal{A}$ still has an analytic (yet complicated) solution. One finds $\mathcal{A}(V_\mathrm{max}, \mu = 0) = 1$ and both expressions deviate by less than one percent around $-\mu \gtrsim 4k_\mathrm{B}T$. When neglecting boundary effects, (4.30b) is in principle valid for $L \to 0$ and we can carry on the varying slope as a squeezed μ-axis like

$$n_\mathrm{tilt}(\mu) \simeq -\lambda_{\mathrm{th}}^{-2}\log(1-\exp(\mathcal{A}\mu/k_\mathrm{B}T)) \tag{4.33}$$

$$= n_\infty(\mathcal{A}\mu) \tag{4.34}$$

which has the same form as the unperturbed function but with $\mathcal{A}$ as a scaling factor. For comparison, the density of an untilted box with a truncated trap becomes

$$n_{\mathrm{trunc}}(\mu) = \mathcal{A}^{-1} n_{\infty}(\mu) \tag{4.35}$$

in the classical regime due to the finite integral boundaries.

Linear Approximation In the classical regime of $-\mu \gtrsim k_{\mathrm{B}}T$, the exponential term in the EoS (4.28) is much smaller than unity and we can thus make a first order Taylor expansion of the logarithm as $-\log(1-x) \simeq x$ to obtain the classical equation for the local density

$$n_{\mathrm{C}}(\mu) \simeq \lambda_{\mathrm{th}}^{-2} \exp(\mu/k_{\mathrm{B}}T) \quad . \tag{4.36}$$

Given the coordinate transformation (4.26a), which transforms the chemical potential as $\mu(x) = \mu_0 - V(x)$, (4.36) resembles a classical Boltzmann-distribution for the potential energy degree of freedom. Here, the shape is still an exponential density curve along a linear potential gradient, but for small box tilts $U_0 \ll k_{\mathrm{B}}T$ the given expression can be further approximated by a linear function since the observed region of μ is much smaller than the decay constant $k_{\mathrm{B}}T$. To properly discuss experimental data, we make the generalized ansatz of a linear density gradient

$$n_{\mathrm{exp}}(\mu) \equiv n(\mu_0) + (\mu - \mu_0) \left.\frac{\partial n}{\partial \mu}\right|_{\mu_0} \quad . \tag{4.37}$$

which can be applied to a density gradient of any slope. Applications are the experimental reconstruction of the equation of state $n(\mu)$ from experimental data or determining the compressibility of the photon gas, as discussed in the following sections.

4.6.2 Experimental Density Profiles

The density gradient is observed experimentally in mechanically tilted box potentials, see Fig. 4.13 for a box with side length $L = 80\,\mu\mathrm{m}$ and tilt energy $U_0/k_{\mathrm{B}} = 43(5)\,\mathrm{K}$ for different photon numbers. The experimental profiles are shown in red with theoretical traces (calculated for Gaussian convolved step functions superimposed by a linear function, similar to in sec. 4.3.2) below for comparison. The latter were picked to match the average photon density. The two-dimensional density distributions are also shown along with each profile where the density gradient is clearly visible in the color variation. In the case of the two lowest intensity profiles (left) one finds the density gradients of experimental and theoretical profiles $\partial n/\partial \mu$ to match over a broad range. Above threshold, one again finds a macroscopic occupation of the ground mode, which is now located in the potential minimum at the box edge. The wave nodes in y-direction are attributed to the mirror surface roughness as discussed in sec. 4.3.2. In panel 3, where the system is slightly above condensation threshold, the experimental profile is a linear gradient superimposed by a ground mode peak as compared to the theoretically expected steep exponential slope as low energy states are roughly equally degenerate. Due to their spatial overlap, the modes partially share the same dye reservoir which could here lead to mode competition [105, 137]. In the deeply condensed regime (panel 4) this effect is less pronounced, hence the impact on the equation of state measurement is minor, see sec. 4.7. The offset at the edges stems from residual fluorescence of excited dye molecules outside of the box region.

Conclusively, the concept of inducing a potential gradient by tilting a cavity mirror so far yields experimental density distributions that agree with theoretical expectations. This paves the way for a measurement the equation of state (sec. 4.7) and the compressibility of the photon gas (sec. 4.8), which will be discussed in the following.

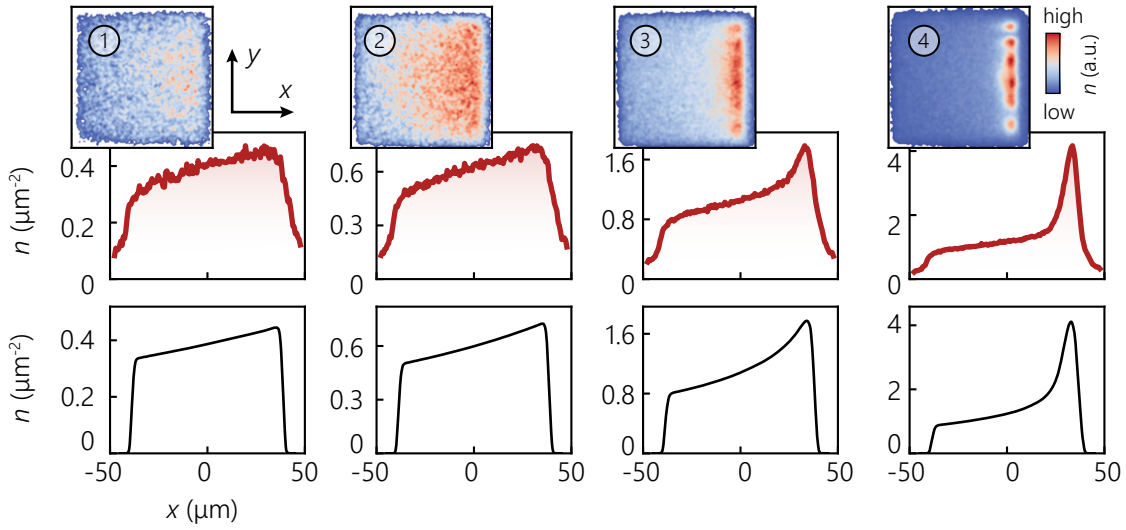

Fig. 4.13: Experimental (red) and theoretical (black, below) density profiles in a tilted box potential with side length $L = 80\,\mu\text{m}$ and $U_0/k_\text{B} = 43\,\text{K}$ for increased photon numbers from left to right. A density gradient towards the potential minimum is visible. The insets show the 2D density profiles where the color mapping is restricted to a certain range to increase visibility of the density gradient.

4.7 Equation of State Reconstruction

While it is straight forward to calculate the equation of state $n(\mu)$, its measurement is challenging as the chemical potential μ is not in-situ accessible and has to be inferred from the experimentally prepared potential. Since the equation of state (EoS) in the form $n(\mu)$ is a monotonous function, one could in principle invert it to $\mu(n)$ and infer the chemical potential from the photon density in the box. The caveat is, that this is exactly the relation to verify here. Experimentally, μ can be controlled in two ways, either by variation of the pump beam power (and hence the photon number) or by employing the potential gradient inferred from the mirror tilt angle. While the photon number yields a chemical potential offset μ_0, the spatially varying density $n(x)$ can be mapped onto the calibrated potential $V(x)$ which yields the EoS in the limit of the local density approximation $\mu = \mu_0 - V(x)$, cf. sec. 1.3.1. Correct conversion of the discrete piezo screw steps into tilt energy (4.5) has been confirmed within an estimated 20 % uncertainty by comparing the position dependent mode energies inside the cavity at the box edges.

Since U_0 is much smaller than the thermal energy scale $k_\text{B}T$, a single density profile does not cover a sufficiently large energy range to reconstruct a large range of the equation of state in one take. Thus, the following method involves a density profile combination process ("stitching") where the box is kept at a fixed tilt angle and the chemical potential offset μ_0 is varied by ramping down the pump beam power. With an appropriate numerically verified overlapping criterion the EoS can be reconstructed.

4.7.1 Measuring the EoS with a Stitching Method

The equation of state $n(\mu) = -\lambda_\text{th}^{-2}\,\log(1 - e^{\mathcal{A}\mu/k_\text{B}T})$ of a photon gas in a tilted box derived in sec. 4.6.1 can be measured by spatially combining several density profiles at a point of common chemical potential, i.e. same density, effectively extending the investigated chemical potential range. In a first step, the density response with respect to a changed chemical potential and the validity of a stitching criterion is investigated numerically. If not otherwise mentioned, the following references to the figure panels are all regarding Fig. 4.14.

As the tilted box potential is a tool to measure properties of the uniform finite-size photon gas,

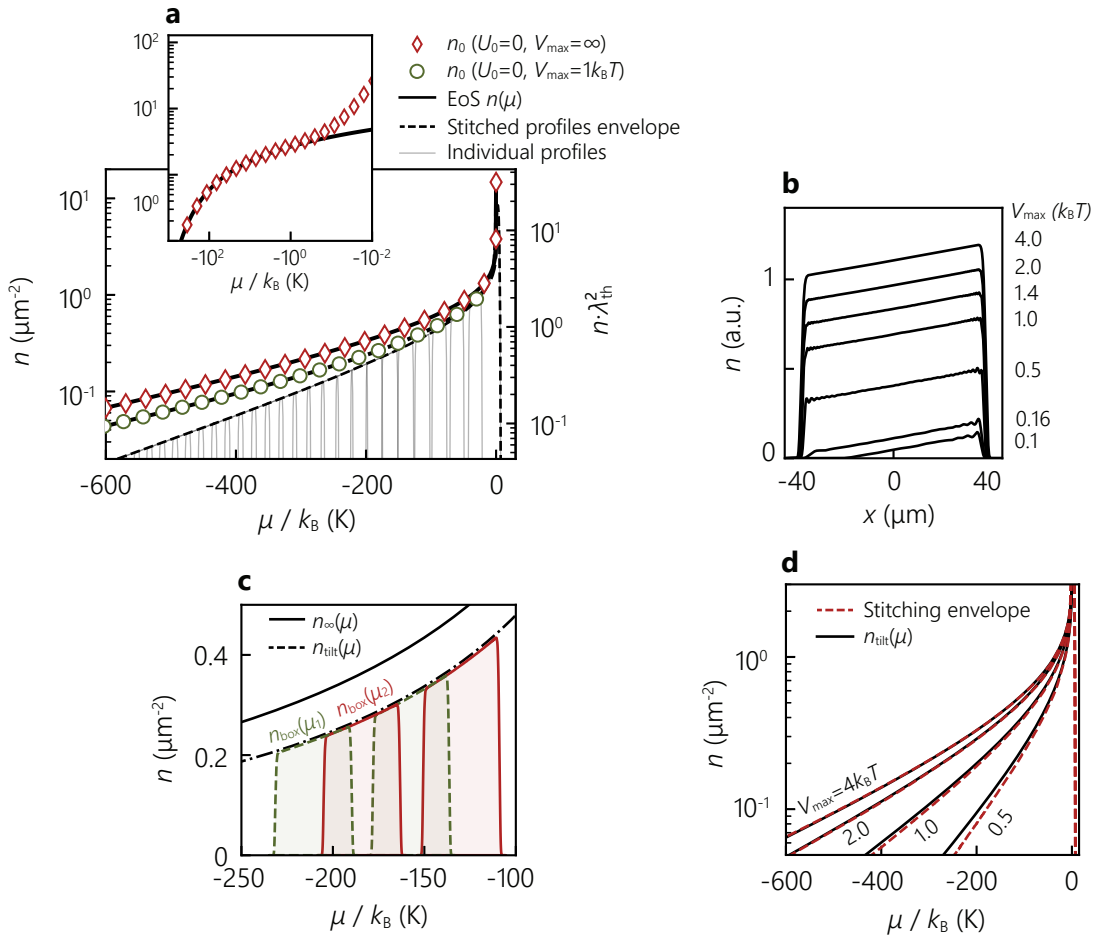

Fig. 4.14: Numerical investigation of the EoS reconstruction method. **a)** Density profiles as a function of the chemical potential in the infinite system ($U_0 = 0$), a box with truncated trap depth ($V_{\max} = 1\,k_BT$) and a tilted box, also with finite trap depth. In the untilted case, the central density n_0 inside the box is well described by the analytic expressions (solid lines). In the condensed phase $\mu \ll k_BT$, the EoS becomes invalid (inset) since the spatial distribution of the dominating ground mode is Heisenberg limited and does not carry thermodynamic information. The EoS in the tilted box is shown as an analytic expression (dashed) along with stitched individual profiles like in c) for a larger range and a trap depth of $V_{\max} = 1\,k_BT$. **b)** Density profiles at constant chemical potential μ_0 for different trap depths. While the slope is mostly unaffected, a uniform reduction of the density is visible. The relative deviation is stronger in the high-μ region (left). **c)** Expected density profiles for different μ (red, green) in a finite-depth tilted box compared to the infinite system EoS $n_\infty(\mu)$ (solid) and its modified analytic form for the tilted box $n_{tilt}(\mu)$ (dash dotted). The profiles indeed match the corresponding EoS $n_{tilt}(\mu)$. A larger μ-range can be covered by stitching different profiles ($U_0/k_B = 43\,\mathrm{K}$) at their points of overlapping density distribution. **d)** EoS $n_{tilt}(\mu)$ for different trap depths (solid, black) along with the envelope of stitched profiles (red, dashed). The latter reproduce the analytic counterpart within experimental accuracy. For trap depths $V_{\max} \gtrsim 4\,k_BT$ no reasonable difference to $V_{\max} \to \infty$ is visible.

we first probe if the analytic solutions hold in the present system. Several density profiles for a non-tilted box ($U_0 = 0$, $V_{\mathrm{max}} \to \infty$) are computed and the central density n_0 is compared with the infinite system EoS. The obtained values are plotted as red diamonds in panel a). In the classical regime we see a perfect agreement with the theoretical prediction (solid). However, as soon as the condensed phase is reached for $|\mu| \lesssim 10^{-1}\, k_{\mathrm{B}}T$ (logarithmic plot in inset panel) the validity of this description ceases to be valid as it was derived for the infinite homogeneous system. The discrepancy in this regime occurs since the integral over the density of states in (4.27) does not account for a macroscopically occupied ground mode. In any case, its intensity distribution has larger extent than $\lambda_{\mathrm{th}} \approx 1.47\,\mu\mathrm{m}$ and hence does not carry thermodynamic information in the sense of $n(\mu)$. Although the simulation looks fine in the linear plot, experimental results in that region have to be interpreted with care.

A central issue in the reconstruction process is the modified density profile due to the finite trap depth $V_{\mathrm{max}} = 1.4\, k_{\mathrm{B}}T$. For the non-tilted box, the green circles in panel a) lie on the analytic expression (4.35). In panel b) several density cuts through a box of side length 80 µm and tilt energy $U_0/k_{\mathrm{B}}T = 50\,\mathrm{K}$ are shown for different trap depths but constant chemical potential. Due to the lower number of available modes, which energetically mostly lie above U_0 and thus have an approximately uniform contribution, the density drops uniformly when the trap depth is lowered. For $V_{\mathrm{max}} < U_0$, the density fully vanishes in the now forbidden regions. As already discussed in sec. 4.6.1, this circumstance leads to a false mapping of chemical potential onto density which can be corrected by scaling the chemical potential with a factor $\mathcal{A} = (1 - \exp(-V_{\mathrm{max}}/k_{\mathrm{B}}T))^{-1}$. As a verification of this thermodynamically derived factor, we take a box with fixed U_0 and V_{max} and vary the chemical potential offset μ_0 which results in different mode occupations. The profiles are then shifted along their x or μ-axis, respectively, up to the point where their densities match, i.e. $n_1(\mu_1) = n_2(\mu_1 + \Delta\mu)$, see panel c). By repeating the process one can then from finite size boxes iteratively extrapolate the density profile to larger systems. Comparison with $n_\infty(\mu)$ and $n_\infty(\mathcal{A}\mu)$ actually confirms that the stitching process reliably recreates the density distribution of larger systems as described by the modified EoS. This method works independent of the trap depths as seen in panel d) where the envelope of the stitched profiles (red, dashed) and the modified EoS lie close to each other. The small discrepancy lies within experimental error margins, hence no refinement of the model is required. Trap depths $V_{\mathrm{max}} \gtrsim 4\, k_{\mathrm{B}}T$ can to good accuracy here be regarded as infinitely deep. The difference between the EoS $n(\mu)$ for a trap depth limited untilted box and tilted box can be seen in panel a), where $n_{\mathrm{tilt}}(\mu)$ (dashed envelope) has a different slope than $n_\infty(\mu)$ instead of a scaling factor.

4.7.2 Measurement Procedure

Experiment The experimental procedure is similar to the numeric approach: The box is tilted with 110 piezo screw steps to a rather high angle of 35 mrad, corresponding to a tilt energy of $U_0/k_{\mathrm{B}} = 43(5)\,\mathrm{K}$. Higher tilt angles are not used since the initially parallel mirror pieces collide at their edges and above some point prevent smaller mirror separations. Similar to the calorimetry measurements (sec 4.5), the computer software saves around 10 images per second. Each time, the pump power is ramped down by a small amount which physically causes a reduction of μ or N, respectively. In the end, there are roughly 300 traces available with effective chemical potentials between $\mu/k_{\mathrm{B}} \approx 10^{-4}\,\mathrm{K}$ and 600 K. As the light levels on the camera sensor tend to become too low for a practical analysis at total photon numbers $N \lesssim 1000$, the pulse length is extended to 1500 ns and the camera gain increased to 100. The obtained camera images are then converted to intracavity photon surface densities via (4.8) and a cut profile is extracted from the vertical central region of the box image to obtain a density cut, which is not modified by boundary effects. The acquired traces are of a kind as in Fig. 4.13.

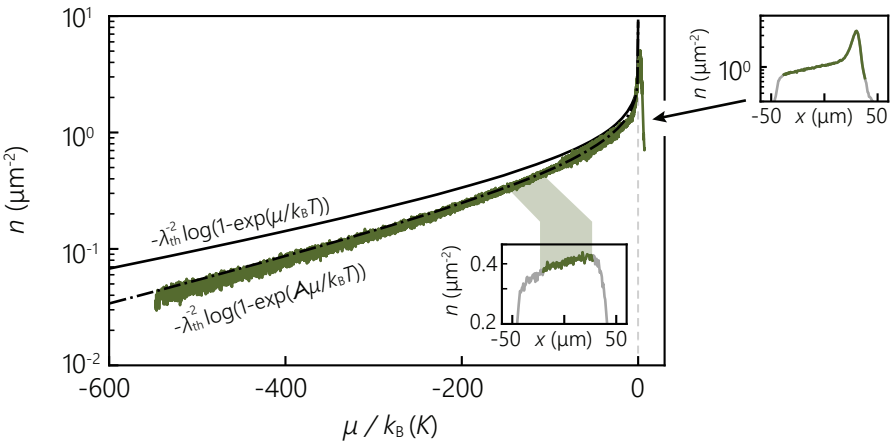

Fig. 4.15: Experimentally obtained equation of state (green). The analytic form of the infinite system is shown for comparison (solid line) as well as the finite depth corrected (dash-dotted line). The inset shows an exemplary density profile of a single recording, where the region used for stitching is marked in green.

Analysis The finite signal-to-noise ratio, especially at weakly occupations ($\mu \ll k_B T$), profiles makes it difficult to find a proper μ-shifting criterion for the pending stitching process. To simplify the problem, the density profiles are approximated by a linear fit function of the kind (4.37) in the region where the density appears to be linear, i.e. excluding boundary effects. Starting from the lowest occupation numbers, the next trace is shifted such that its leftmost (low μ) point crosses the previous linear fit function. To reduce stitching errors, the average μ-difference between two traces is $\Delta\mu/k_B \lesssim 2\,\mathrm{K} \ll U_0/k_B$. The fitting and stitching processes are automated. An initial global μ offset is chosen to shift the final stitched trace to the theoretical prediction of the EoS as the method only connects relative changes in μ.

Around the threshold region $|\mu|/k_B \lesssim 50\,\mathrm{K}$, where the density profiles can not anymore be substituted by a linear fit function over the whole trace, suited density profiles are directly employed to represent the EoS in that region as the density peak from the ground mode dictates their position. Here, the left edge of the ground mode has to be aligned to $\mu = 0$ as it corresponds to the offset energy of the mode.

Results The final result of the stitching process is shown in Fig. 4.15. In fact, with the here presented method we were able to recreate the modified equation of state (4.33) for a photon gas in a tilted finite-depth box (dash-dotted). The ripples of the graph stem from the large amount of overlapping density profiles, which naturally scatter in their amplitude although they are already integrated over a certain region of the box. In principle, the determined EoS would already suffice to infer the compressibility κ_T of the gas via a derivative ∂_μ. However, as the analysis requires manual input at several stages, a more robust method is presented in sec. 4.8. Moreover, for a measurement of κ_T it is eligible to measure for multiple values of U_0, which is here restricted to large values, hence another method is presented in sec. 4.8.

4.8 Compressibility

The isothermal compressibility κ_T of the photon gas, like the equation of state, also can be inferred from the density gradients in a tilted box. For the infinite ideal Bose gas one would expect an infinite compressibility in the condensed phase as any particle in the ground state does not exert any pressure to its environment. It turns out that this circumstance breaks down in finite size systems since the residual kinetic energy of the ground state due to the spatial confinement

("Heisenberg pressure", see sec. 4.3.3) acts against the system walls and above a certain density overshadows its infinitely compressible character.

For the infinite ideal Bose gas one obtains an analytical expression for κ_T when inserting (1.38) into (1.45) to get

$$\kappa_{T,\infty} = \frac{1}{n_\infty^2(\mu)} \left(\frac{\partial n_\infty(\mu)}{\partial \mu} \right)_{T,N} \tag{4.38}$$

$$= \frac{1}{k_\mathrm{B} T} \frac{e^{\bar{n}\lambda_\mathrm{th}^2} - 1}{\bar{n}^2 \lambda_\mathrm{th}^2} \tag{4.39}$$

which solely depends on the density of the gas. In the classical limit of low densities where $\exp(\bar{n}\lambda_\mathrm{th}^2) \simeq 1 + \bar{n}\lambda_\mathrm{th}^2$ the expression simplifies to

$$\kappa_{T,\mathrm{C}} \simeq \frac{1}{k_\mathrm{B} T} \frac{1}{\bar{n}} \tag{4.40}$$

$$= \frac{1}{p} \tag{4.41}$$

which, when integrated (reversing the κ_T definition), yields the ideal gas equation $pV = Nk_\mathrm{B}T$ and one finds the compressibility to be the inverse pressure of the gas. In the quantum limit (high phase space densities) we get an exponential growth with the phase space density as

$$\kappa_{T,\mathrm{Q}} \simeq \frac{1}{k_\mathrm{B} T} \frac{e^{\bar{n}\lambda_\mathrm{th}^2}}{\bar{n}^2 \lambda_\mathrm{th}^2} \quad . \tag{4.42}$$

Similar to sec. 4.6.1, the analytic form is not applicable in all regimes as we here work with a finite trap depth environment. The compressibility is obtained by inserting (4.35) into (1.45) and one finds that the system is more compressible by a constant factor

$$\kappa_{T,\mathrm{trunc}} = \mathcal{A}^2 \, \kappa_{T,\infty} \quad . \tag{4.43}$$

For a tilted box we get a slightly different analytical expression (4.33). Here we identify the compressibility with a derivative as

$$\kappa_{T,\mathrm{tilt}} = \mathcal{A} \, \kappa_{T,\infty} \quad . \tag{4.44}$$

In all scenarios, the equation of state and compressibility are adjusted by powers of the prefactor $\mathcal{A}$ within experimental accuracy.

Experimentally, one could in principle derive the obtained equation of state data from sec. 4.7. However, since the analysis method intrinsically has several (also manual) degrees of freedom, we aim for a more robust approach. For a start, we discuss the textbook definition of the compressibility, namely the relative volume change under external pressure change. Since this is experimentally unfeasible in the here used experiment a different method is presented, which in principle extracts equivalent information from the system. It allows to determine the isothermal compressibility of the finite-size homogeneously trapped photon gas.

4.8.1 Variation of the Box Size

The compressibility is defined as the relative volume change $\mathrm{d}V$ under external pressure change $\mathrm{d}p$. Changing the physical volume of the delaminated box potential structures during operation is not feasible with the current technical capabilities, especially during photon storage times below one nanosecond. To nevertheless give an intuitive picture of a compressed ideal Bose gas in a box, we start with a numerically computed $p - V$ diagram. Let a thermalized ensemble

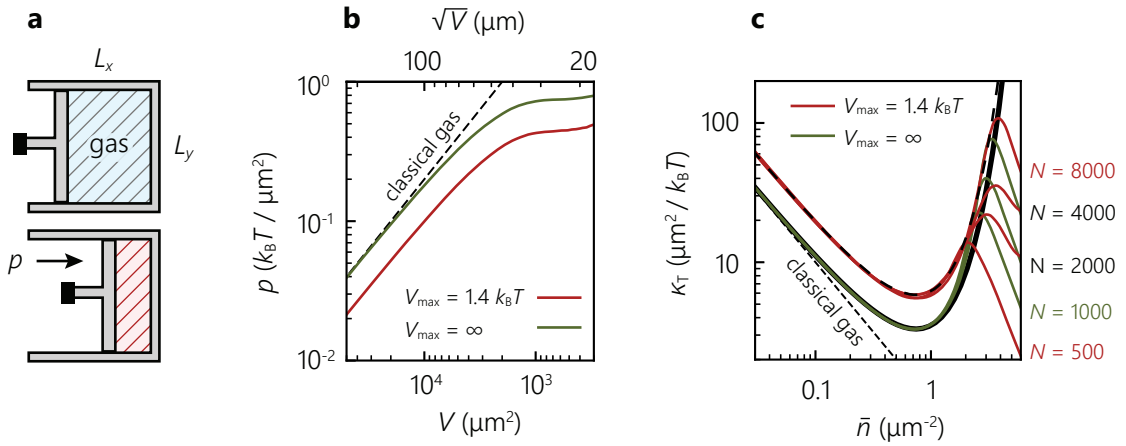

Fig. 4.16: Numeric exploration of the compressibility. **a)** Experimentally for the present photon system unfeasible concept of squeezing the box with a piston. **b)** Exemplary p-V diagram for $N = 2000$ photons during the compression process for finite and infinite potential depth V_{max}. **c)** Compressibility inferred from the p-V diagrams for different photon numbers and trap depths. For higher N, condensation sets in at box sizes closer to infinity, hence the graphs diverge from the analytic curve (solid black) at higher densities. The dashed black line shows the analytically obtained expected compressibility (4.43) for the truncated trap. Black N labels belong to both trap depths.

of N photons be initially trapped in a square box of side length L and volume (area) $V = L^2$. The relevant internal energy U of the gas is encoded in its transverse momentum, hence the photons exert a pressure onto the potential walls (force per length). Since there are only two (kinetic) degrees of freedom in our system, the thermal and caloric equation of state coincide, $pV = U = Nk_{\mathrm{B}}T$, hence the pressure is given by

$$p = \frac{U}{V} = \frac{U}{L^2} \qquad \text{(2d, homogeneous).} \tag{4.45}$$

Assuming that the box is now squeezed by decreasing its size $L \to L - \Delta L$, all single particle states shift upwards in energy due to the $1/L^2$ scaling, see Fig. 4.16a. The photons are then thermally redistributed over the new set of eigenstates (isothermal compression). Since N is constant, the average energy per particle increases while the critical particle number for condensation N_{c} decreases. Below a critical size L_{c}, the photons begin to condense into the new ground state, which eventually absorbs all motionally excited photons if the procedure is continued. Shifting the energy levels such that $E_{11} = 0$ is unphysical here as the compression is actually acting against the zero point energy, which is not anymore negligible in the given scenario. Exemplary numerical p-V diagrams and obtained compressibilities (including the finite trap depth) are shown in Fig. 4.16b/c. In the initial compression phase (high V, left), where the gas is expected to behave classically due to the low densities, the pressure fulfills the relation $p \propto 1/V$ as verified by the colinearity of the graph with respect to the behavior of an ideal classical gas (dashed). As the critical particle number for condensation N_{c} shrinks closely linear with the box volume (see sec. 2.4.2) the photons ultimately condense at densities of order $n \approx 1\,\mu\mathrm{m}^{-2}$, visible as the curve flattens. This sign of vanishing pressure response already hints at the infinite compressibility in the condensed regime. However, after a plateau, the pressure rises again due to the increasing ground state energy (Heisenberg uncertainty) which ultimately dominates for box sizes below $L \lesssim 20\,\mu\mathrm{m}$. The lower pressure for finite trap depth is well understood as higher energetic modes, which contribute higher pressure are cut off and low lying modes are overrepresented.

The isothermal compressibility is directly obtained from the p-V diagrams via $\kappa_T = -V^{-1}\partial V/\partial P$. For low densities, the infinitely deeply trapped gas well represents the classical ideal Bose gas compressibility indicated by the dashed line in Fig. 4.16c. The transition to a quantum gas starts

at particle densities above $\bar{n} \gtrsim 0.1\,\mu\text{m}^{-2}$ where classical and quantum value start to diverge. The minimal value is reached at $\bar{n}_{\text{min}} \approx 1.59/\lambda_{\text{th}}^2 \approx 0.74\,\mu\text{m}^{-2}$. At higher densities, the compressibility starts to increase again and theoretically diverges towards infinity as indicated by the solid black line. Finite size effects are pronounced more strongly than in the p-V diagram as the emerging Heisenberg pressure of the squeezed ground state ultimately renders the system incompressible, i.e. $\kappa_T \to 0$. For varying particle numbers, condensation sets in at different box sizes, where the larger boxes much better represent the infinite system limit and thus the extracted compressibilities show better agreement with the infinite system curve. We expect the system to be more compressible as there is a smaller force counteracting against the pushing piston which is revealed by the simulated curves; the behavior in the degenerate regime is analogous. For densities below the ones in the breakdown region, the analytic expression (4.43) well matches with the numerics (dashed black line).

4.8.2 Center of Mass Displacement

Changing the box volume is unfeasible during experimental operation, hence different observables have to be employed to extract the compressibility of the photon gas. A practical method to extract the compressibility of the gas is from its density response to infinitesimal perturbations as induced by a weak potential gradient, which can again be realized by a tilted cavity mirror, already discussed in sec. 4.6. Experimental density profiles are too noisy to reliably detect irregularities in the density profile at small tilts. A more suitable method is to pool the spatial information into a single quantity, namely the center of mass $\langle x \rangle$ of the photon cloud. For symmetry reasons, the problem is reduced to a single dimension x where the density profile is averaged to

$$\bar{n}(x) \equiv \int_{\text{ROI}} n(x,y)\,\mathrm{d}y \quad . \tag{4.46}$$

For experimental data, the integration is performed over a suited region of interest (ROI) as boundary effects disturb the reliability of the method. With the total photon number $N = \int_{\text{ROI}} \bar{n}(x)\,\mathrm{d}x$ the latter can be expressed via

$$\langle x \rangle = \frac{1}{N} \int_{\text{ROI}} x\,\bar{n}(x)\,\mathrm{d}x \quad . \tag{4.47}$$

Starting from the local density approximation and assuming small mirror tilts, we make a linear ansatz as in sec. 4.7 for the density profile like $x(\mu) = (\mu_0 - \mu)L/U_0$. Inserting into (4.47) and performing the variable substitution of position x to chemical potential μ yields

$$\langle x \rangle = \frac{1}{N} \int_{-L/2}^{L/2} x\,n(x)\,\mathrm{d}x \tag{4.48}$$

$$= \frac{1}{N} \int_{\mu_0+U_0}^{\mu_0} (\mu - \mu_0) \frac{L}{U_0}\, n(\mu)\, \frac{L}{U_0}\,\mathrm{d}\mu \tag{4.49}$$

$$\simeq \frac{L^2}{NU_0^2} \int_{\mu_0+U_0}^{\mu_0} (\mu - \mu_0) \left[n(\mu_0) + (\mu - \mu_0) \left.\frac{\partial n}{\partial \mu}\right|_{\mu_0} \right] \mathrm{d}\mu \quad . \tag{4.50}$$

Using the relation $\kappa_T = -V^{-1}\partial V/\partial P$ we finally arrive at

$$\langle x \rangle = -\frac{U_0 L^2}{12N} \left.\frac{\partial n}{\partial \mu}\right|_{\mu_0} \tag{4.51}$$

$$= -\kappa_T \frac{\bar{n} U_0 L}{12} \tag{4.52}$$

where in the last step, the photon surface density was further reduced to an entirely averaged density $\bar{n} = N/L^2$. From the center of mass response we can extract the isothermal compressibility via the relation

$$\kappa_T(\bar{n}) = -12\frac{\langle x\rangle/L}{U_0}\frac{1}{\bar{n}} \tag{4.53}$$

where the factor $\langle x\rangle/L \;/\; U_0$ is the relative center of mass displacement versus tilt energy; normalizing to the gas density yields the compressibility κ_T. The robustness of this method will be discussed using another numeric approach.

4.8.3 Experimental Implementation and Numerical Predictions

As discussed in sec. 4.7, the experiment offers a reliable method to introduce a linear potential gradient by tilting one of the cavity mirrors. Before performing the actual experiment, we carry out a numerical simulation to confirm the center of mass method and probe its limits. For this purpose, a set of density profiles is computed for $U_0/k_\mathrm{B} = -25\,\mathrm{K}$ to $25\,\mathrm{K}$ and photon numbers in the range $N = 100$ to $15\,000$. Exemplary density traces for different total photon numbers N and $U_0 = \{0, \pm 25\}\,\mathrm{K}$ are shown in Fig. 4.17a. For photon numbers $N \ll N_\mathrm{c}$, e.g. $N = 500$, the density profile has a linear gradient. The tilted box potentials as used in the simulation $V(x)$ are shown; the gradient is amplified by a factor of 2.5 for better visibility. At $N \approx 1000$ quantum degeneracy is predicted to emerge at the box edges. Note that as the low lying modes are already confined more tightly, degeneracy emerges at much lower photon numbers since the energy separation of those modes is increased. For $N = 2200$ the density profile is already highly nonlinear while condensation is finally reached at $N \approx 3200$. Next, we look at the center of mass response $\langle x\rangle/L$, see panel b). Below threshold, also including the nonlinear density profiles at $N = 2200$, the center of mass response is linear in the here shown U_0 range. In the condensed phase, the S-shaped response curves saturate which is physically understood as the ground mode is squeezed into the potential minimum at the box edge and can not move any further outwards. From hereon, the center of mass does not significantly change when the potential gradient U_0 is enhanced or more photons are added to the system. Nevertheless, the response is always approximately linear in a varying region around $U_0 = 0$, which will be the here employed validity criterion of the center of mass method. The compressibility $\kappa_{T,\mathrm{tilt}}$ is given by the slope of the response curves normalized to the mean density as in (4.53). Saturation of the center of mass already hints at a breakdown of the infinite compressibility (expected for $L \to \infty$), which is intrinsic for the given finite size systems (see sec. 4.8.1). The numerically inferred compressibility is shown along with experimental data in Fig. 4.18.

4.8.4 Experimental Procedure

Data Acquisition The here presented method partially relies on the density profile of the box ground mode, hence we are limited to box sizes of $L = 40\,\mu\mathrm{m}$ as larger (non-tilted) boxes do not reliably host a sinusoidal ground mode due to the residual mirror surface roughness. The box is tilted to a maximum value of +110 piezo steps, corresponding to a tilt energy of $U_0/k_\mathrm{B} = 22(3)\,\mathrm{K}$. Data sets for different densities are obtained by ramping down the pump beam power and simultaneous image acquisition. The box is then tilted back towards a parallel alignment $U_0 =$ in small steps and the procedure is repeated such that data is acquired in the form $n(\mu, U_0)$ for many μ and U_0. The used piezo screw steps are $\pm\{0, 2, 4, 6, 8, 10, 15, 20, 25, ..., 110\}$. Negative numbers here mean tilting in the opposite direction to improve data integrity. The measurements were performed at $q = 8$ and $\lambda_\mathrm{c} = 583\,\mathrm{nm}$ to avoid excessive mechanical stress between the cavity mirrors.

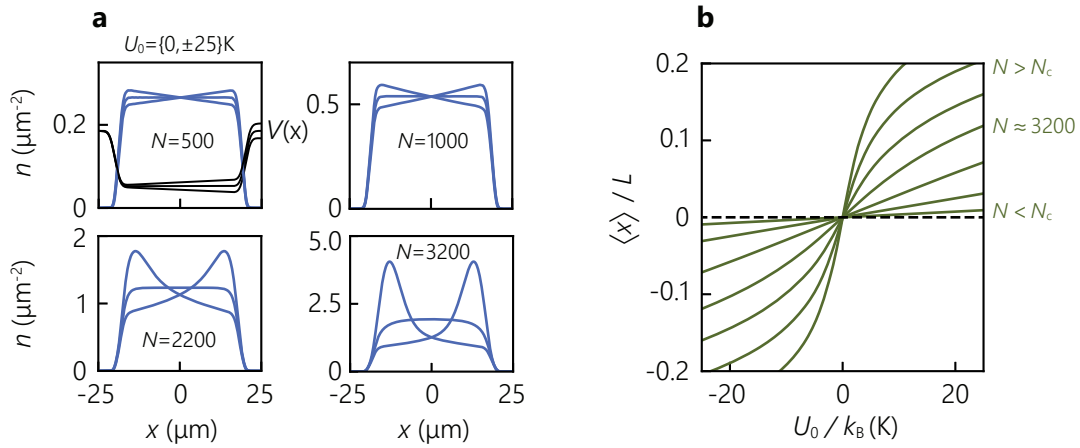

Fig. 4.17: a) Expected density profiles of the photon gas for different total photon numbers N and for $U_0 = \{0, \pm 25\}$ K. For increasing N, the density profile shows a transition from having a shallow linear gradient to highly nonlinear shapes in the condensed regime. The shown exemplary potential outlines $V(x)$ (arbitrary units) are enhanced in their gradient for better visibility. **b)** Center of mass response $\langle x \rangle / L$ of the photon cloud versus tilt energy U_0 for various N. Below threshold, the response is entirely linear in the here shown U_0 range while above, a saturation is observed owing to the finite size box, providing an upper limit for the center of mass displacement.

Analysis The acquired images are cropped to regions of interest of roughly $L_{\mathrm{ROI}} \approx 30\,\mu$m (box size is $L = 40\,\mu$m) to avoid the influence of the smeared out surface density at the box edges. The following evaluation is then similar to the procedure to the numerical simulation in sec. 4.8.3. The experimental density profiles have to be sorted by their occupation number. As the traces typically do not have equal photon number, the respective closest matching profiles for a target N are picked. The tilt energy U_0 is inferred from the piezo screw steps where as a post-correction, the zero point of the tilt angle can be inferred afterwards from the zero crossing of the center of mass and turns out to be around 2 K. A linear function is fitted in a region around the zero crossing. At low densities one can use the full data range as an input for the fit function due to the fully linear response. Above the degenerate regime, the fitting region is successively reduced down to $|U_0|/k_{\mathrm{B}} < 3\,$K for the highest occupations. From the slope of the fit we get the ratio of $\langle x \rangle / U_0$ for a certain value of $\bar{n} = N/L^2$ which resembles one data point.

Results Experimental density profiles at same N but different U_0 are shown in Fig. 4.18a. One can qualitatively observe the expected behavior of photons accumulating in the new potential minimum. Below threshold (top), the density profile in the inner regions can be well described by a linear function whose slope changes along with U_0. The extracted center of mass shift versus the tilt energy is shown in panel b) for three exemplary photon numbers: below ($N < N_{\mathrm{c}}$), around ($N \approx N_{\mathrm{c}}$) and above threshold ($N > N_{\mathrm{c}}$). Below threshold, the response of the center of mass is linear with respect to U_0 as verified by the good agreement with the linear fit function. For the S-shaped curve far above threshold, only the inner region around $U_0 \approx 0$ is employed for fitting to isolate the linear response. The obtained compressibility κ_T is shown in panel c) (red diamonds). At low densities we find the data points to significantly lie above the infinite system theory $\kappa_{\mathrm{T},\infty}$ (solid black). This is well understood to be a consequence of the finite trap depth as already explained in sec. 4.8.1. In fact, the data points agree well with the numerical prediction obtained using the center of mass displacement (solid red) explained in sec. 4.8.3 taking into account experimental parameters such as finite trap depth and smooth box walls. Another numeric curve from Fig. 4.16 representing the squeezed box (solid gray) is shown for comparison. Their difference at low densities is due to the fact that the photon gas in a tilted box

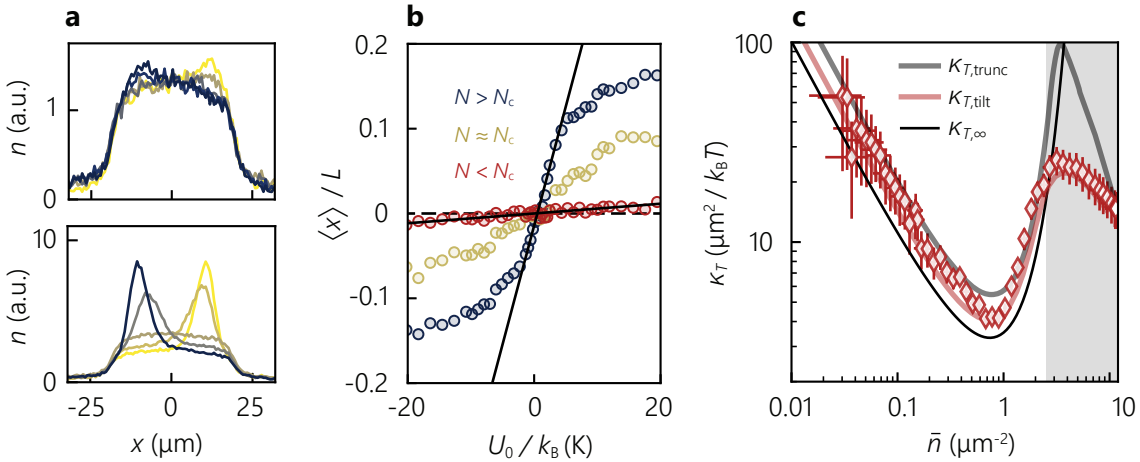

Fig. 4.18: Experimental compressibility measurement. **a)** Density profiles above (top) and below (bottom) threshold for various mirror tilts corresponding to $U_0/k_\mathrm{B} \approx \pm\{0, 5, 11\}\,\mathrm{K}$. **b)** Center of mass response of the photon gas with respect to the applied potential gradient U_0. Below threshold (red), the response is linear whereas it saturates in the condensed regime (dark blue). By restricting a linear fit to a region around $U_0 = 0$ one can extract the linear part of the response to determine the compressibility. **c)** Data for the isothermal compressibility κ_T. Solid black line shows the infinite system theory. Also shown are numerically obtained curves in a non-tilted box (gray) and a simulated center of mass method (red). Gray shaded region indicates where the infinite system theory becomes inapplicable as the local density approximation ceases to be valid in condensed finite size systems.

is described by a modified equation of state $n_\mathrm{tilt}(\mu)$, see sec. 4.6.1. The modified analytic curves for a finite depth (4.43) and the tilted box (4.44) (also finite depth) are not shown as they overlay with the instead shown numeric examples. The numeric curve for the untilted box (solid gray) rises higher because it was computed for 8000 photons, which condense at a larger box size and hence are more comparable to an infinite system. For $N \approx 3000$ it drops off in the same region, as seen in Fig. 4.16c. The shaded area at densities $\bar{n} \gtrsim N_\mathrm{c}/L^2 \approx 2.7\,\mu\mathrm{m}^{-2}$ marks the invalid region of the local density approximation, obtained when comparing the analytic expression for N_c (2.62) with the EoS (1.38). In this regime, the center of mass $\langle x \rangle$ no longer is a good quantity to extract the compressibility. The larger error bars in the low density regime arise from the here more noisy profiles.

We conclude that the here presented experiment reproduces the theoretically expected response of the density profile. The limits of the validity of the method are well understood and are also confirmed with the experimental data.

CHAPTER 5

Conclusion & Perspectives

In this doctoral thesis, investigations about the classical application of the dye-filled microcavity as a paraxial light concentrator as well as the quantum gas related experiments on homogeneously trapped photon gases have been carried out. The main results can be summarized as follows:

- The feasibility of the dye-filled microcavity apparatus as a platform for paraxial light concentration was investigated. Although the photon gas transforms from an initially hot to a room temperature cloud, a phase space build-up could not be observed. The results were understood by experimental and theoretical determination of the loss probability of spontaneously emitted photons from the microcavity providing an only one-dimensional bandgap.

- A platform for homogeneously trapped photon gases was established. The delamination technique in combination with the sufficiently low surface roughness of the employed mirrors for the first time allowed for the observation of textbook-like mode structure of a condensed photon cloud in a box-shaped potential. The spatial, momentum and spectral distributions agree with a thermal gas at $T = 300\,\mathrm{K}$, when predictions are corrected for an experimentally limited finite trap depth of $V_{\mathrm{max}} = 2\pi\hbar \times 8.7(14)\,\mathrm{THz} = 1.4(2) k_{\mathrm{B}} T$.

- From spectra the caloric properties, namely internal energy and specific heat for varying particle numbers across the transition from a thermal photon to a Bose-Einstein condensate could be determined. The findings revealed that in a two-dimensional finite box potential, those quantities are continuous across the condensation threshold, as expected in the absence of a second order phase transition.

- By superimposing a linear gradient to the box potential, the equation of state $n = n(\mu)$ could be measured over a chemical potential range of $2\,k_{\mathrm{B}}T$ by controlled stitching of multiple obtained traces. In a further measurement, the isothermal compressibility κ_T could be determined for various photon densities across the condensation threshold. The experimental data well follows finite size box theory as it starts to diverge towards infinity upon emerging quantum degeneracy but ultimately drops due to the nonzero ground state energy.

In future works, the light concentration efficiency could be improved by isotropic resonator confinement capabilities, e.g. via a three dimensional bandgap for the photon gas [141, 142], allowing for a more efficient redirection of the captured fluorescence. Other than dielectric mirrors, photonic crystal structures could here serve as a platform for modifying the local density of states and provide strong isotropic confinement [143, 144].

Concerning the measurements of the thermodynamics of photon gases in box potentials, it would

for the future be important to reveal the origin of the experimentally observed limitations of the potential depth. A possible approach to realize deeper wells is the use of shallow slopes as they could reduce the material stress in the border regions, preserving their reflectance. Moreover, current works aim for dielectric layer delamination without the employment of an Si layer by using ultraviolet light as a heating source as sufficient short-wavelength radiation gets absorbed directly by the Ta_2O_5 layers. To this day, the reflecting mirror surface structuring possibilities, including the maximum achievable trap depth, of correspondingly created potentials have not been investigated.

The critical photon number for condensation (2.62) was derived via coherence arguments, although the behavior remains to be verified in the here used box environment. Current works focus on the temporal and transverse coherence envelope function, which is here expected to be Gaussian in the classical, exponential in the degenerate and algebraic in the quasi-condensed regime [51]. Ongoing measurements carried out by Leon Espert Miranda following the procedure in [55] already hint that in the classical regime, the transverse first order coherence length in the order of the thermal wavelength and, upon macroscopic occupation of the ψ_{11} ground mode, a system-spanning function. Such an ideal gas system could serve as a candidate for verification of the universality of critical exponents as predicted by the Ginzburg-Landau theory [57, 145] by precise correlation measurements close to the phase transition for $(T - T_c)/T \to 0$.

The here presented compressibility measurements were carried out during a mechanical steady state of the cavity. A deeper investigation of the density response to potential gradients would be to induce the latter during the photon storage time and observe time-resolved spatial redistribution. Such potential gradients can be realized by thermally introduced refractive index gradients using e.g. picosecond laser pulses. Modifications of the potential landscape relying on thermally induced refractive index changes have already been investigated in our system under steady state conditions [26] and temporally changing on the nanosecond timescale [121, 124].

The two-dimensionality of our system can be further reduced to a one-dimensional system. Current works in our group in collaboration with the Freyman group in Kaiserslautern investigate photon gases in 3D-printed polymer structures on the mirror surface which imprint an attractive potential as their refractive index lies above that of the dye solvent [26]. Although the smoothness does not yet match the untreated mirror surface its diffraction limited transverse resolution of tens of nanometers [146] enables the creation of one dimensional potentials, a regime that is reached when one box side length falls below the thermal wavelength $\lambda_{\mathrm{th}} \approx 1.5\,\mu\mathrm{m}$ or, equivalently, the energy spacing in this dimension becomes larger than $k_{\mathrm{B}}T$ [147]. Contrary to atomic Bose gases, where thermalization is mediated via interparticle collisions which are unable to drive a one dimensional system into thermal equilibrium [148], the photon gas can overcome this limitation as the coupling to the dye heat bath is independent of the geometry.

Further possible interesting future studies include the observation of sound and vortices [17, 18, 20], the latter being enabled when introducing Kerr media [149] to the system. Previous investigations showed that the largest feasible nonlinear medium inside the cavity is the dye resonance itself [150], which would result in a dimensionless interaction parameter of $\tilde{g} \approx 10^{-6}$, which is too low to observe those effects. A more promising candidate could be the presence of a nonlinear crystal inside the resonator volume which provides an effective instantaneous photon self-interaction based on the phase shift of a virtual down- and upconversion inside the resonator volume; the topic is subject of current research [151].

Appendix

A.1 Electric Field Distribution in the Cavity

The highly reflective cavity mirrors used in this experiment employ a stack of thin dielectric material layers with thickness d_i and refractive index n_i. This structure represents a photonic crystal for which a simple yet powerful method to compute electromagnetic fields exists. At each material boundary ij a portion of the incident light field E_0 is reflected (E_r) or transmitted (E_t) as described by the Fresnel equations (here for normal incidence and $i, j = 1, 2$)

$$r_{12} = \frac{E_r}{E_0} = \frac{n_1 - n_2}{n_1 + n_2} \quad , \quad t_{12} = \frac{E_t}{E_0} = \frac{2n_1}{n_1 + n_2} \quad . \tag{A.1}$$

Hence, the resulting total electric field is the sum of many partial forward and backward propagating waves. If the layer thicknesses are chosen appropriately (typically $d_i \approx \lambda_0/4n_i$, λ_0 is the design wavelength) the backward propagating waves interfere constructively and ultimately cause a reflection of the incident beam (see sec. A.1.1 for more details). Contrary to metallic mirrors, this interference mechanism causes the wave nodes to not necessarily locate on the mirror surface but rather to form a nontrivial standing wave pattern that penetrates the dielectric environment. This distribution can be calculated with the so-called transfer matrix method [69] and helps to understand the interaction of the trapped photon gas with the enclosed dye solution. Let $E_{1,2}$ be the electric field on left / right side of an arbitrary position in the medium and $E_i^{+/-}$ be the right / left propagating component. An incident wave transforms into a transmitted and reflected part which are connected via

$$\begin{pmatrix} E_2^+ \\ E_1^- \end{pmatrix} = \hat{S} \begin{pmatrix} E_1^+ \\ E_2^- \end{pmatrix} \quad \text{or} \quad \begin{pmatrix} E_2^+ \\ E_2^- \end{pmatrix} = \hat{M} \begin{pmatrix} E_1^+ \\ E_1^- \end{pmatrix} \tag{A.2}$$

where $\hat{S}$ and $\hat{M}$ are called scattering matrix and transfer matrix. For a beam with wave vector k propagating in z direction one finds the following scattering matrices for propagation $\hat{S}_\mathrm{p}$ and partial reflection at a dielectric boundary $\hat{S}_\mathrm{b}$

$$\hat{S}_\mathrm{p} = \begin{pmatrix} e^{-\mathrm{i}k_0 z n} & 0 \\ 0 & e^{-\mathrm{i}k_0 z n} \end{pmatrix} \quad , \quad \hat{S}_\mathrm{b} = \begin{pmatrix} t_{12} & r_{21} \\ r_{12} & t_{21} \end{pmatrix} \tag{A.3}$$

The scattering matrix can be converted to the corresponding transfer matrix via the relation

$$\hat{M} = \frac{1}{\hat{S}_{22}} \begin{pmatrix} \hat{S}_{11}\hat{S}_{22} - \hat{S}_{21}\hat{S}_{12} & \hat{S}_{12} \\ -\hat{S}_{21} & 1 \end{pmatrix} \tag{A.4}$$

Only the transfer matrices can be reduced to a single operation by their reverse product

$$\hat{M}_\mathrm{total} = \prod_{i=0}^{N-1} \hat{M}_{N-i} = \hat{M}_N \cdot \ldots \cdot \hat{M}_2 \, \hat{M}_1 \tag{A.5}$$

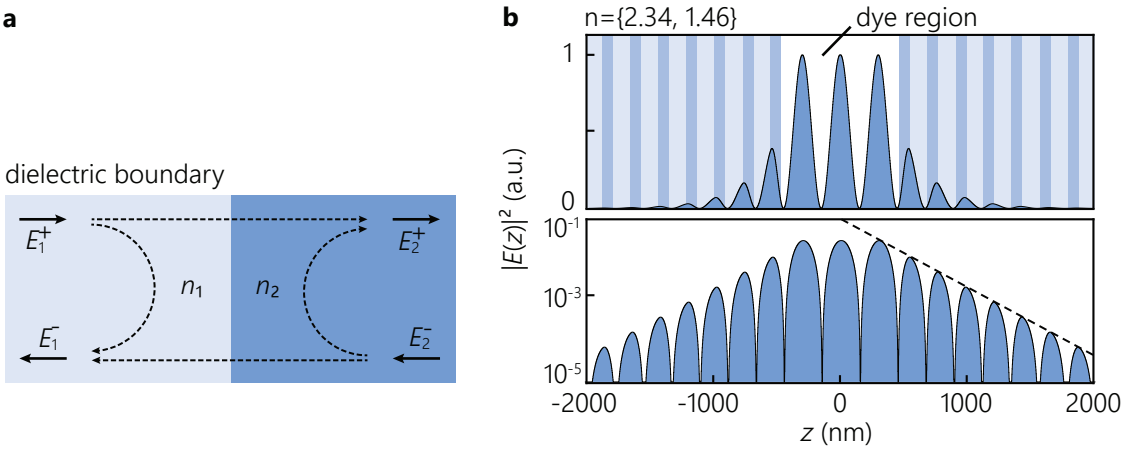

Fig. A.1: a) Effect of a dielectric boundary on forward and backward propagating waves. An incoming wave splits into a transmitted and a reflected part. **b)** Intensity of a resonant standing wave inside the cavity, in linear (top) and log scale (bottom). Dielectric layers are hinted as bars with alternating color in the background, with the darker colors corresponding to higher n. Dashed line is a fitted exponential decay $I(z) = I_0 \exp(-3.8\,\mu\text{m}^{-1} \cdot z)$.

which can then be back converted to a scattering matrix $\hat{S}_{\text{total}}$ by the same relation as (A.4) but swapping $\hat{S}$ and $\hat{M}$. When choosing $E_1^+ \in \mathbb{C}$ and $E_2^- = 0$ one can calculate E_1^- with (A.1). The field distribution along the photonic structure is then obtained by recursive application of $\hat{M}_i$ to the starting vector. An exemplary standing wave inside the microcavity is shown in Fig. A.1b. One sees how the light spends a certain amount of time inside the mirror material while the (squared) amplitude decays exponentially.

The energy density $\mathcal{W}$ is calculated by additional weighting of the squared amplitude with the local refractive index

$$\mathcal{W}(z) \propto \int_{z_1}^{z_2} n(z)\,|E(z)|^2 \mathrm{d}z \tag{A.6}$$

which is proportional to the time the light spends in a length element dz.

A.1.1 Properties and Design of Dielectric Mirrors

All cavity mirrors used in the scope of this thesis are based on dielectric thin film coatings, hence the name *dielectric mirror*. They are composed of several thin film layers with alternating high and low refractive index. By stacking many of these layer pairs one can reach a reflectivity of $R \lesssim 99.999\,\%$ in the visible spectral regime, see Fig. A.2 for an illustration of the working principle. Although the previously described matrix formalism already yields all necessary tools to calculate the reflective properties of such a mirror, one can still make some simplifications [69, 152]. The layers are coated on a substrate with refractive index n_s where each boundary contributes a partial wave with phase δ_j. Usually the property of interest is the total reflectivity value $R = |r|^2 = |v_1/v_2|^2$ of the layer stack with

$$\begin{pmatrix} v_1 \\ v_2 \end{pmatrix} = \begin{pmatrix} \eta_0 & -1 \\ \eta_0 & 1 \end{pmatrix} \left[\prod_{j=1}^{N} \begin{pmatrix} \cos(\delta_j) & \frac{\mathrm{i}}{\eta_j} \sin(\delta_j) \\ \mathrm{i}\eta_j \sin(\delta_j) & \cos(\delta_j) \end{pmatrix} \right] \begin{pmatrix} 1 \\ \eta_s \end{pmatrix} \tag{A.7}$$

$$\delta_j = k_j\, d_j \cos(\theta_j) = \frac{2\pi}{\lambda} \eta_j\, d_j \cos(\theta_j) \tag{A.8}$$

where η are the pseudo refractive indices, which are calculated from the normal refractive indices via $\eta_i = n_i \cos\theta_i$ for s-polarized light and $\eta_i = n_i / \cos\theta_i$ for p-polarized light. In the case of

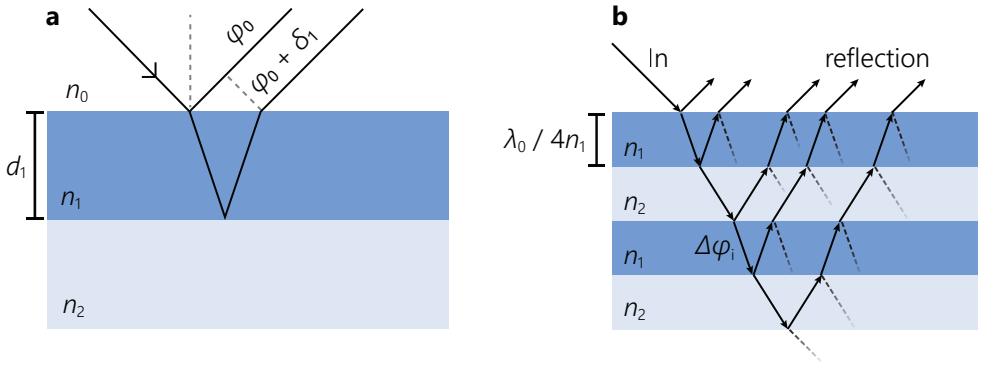

Fig. A.2: Working principle of a dielectric mirror. **a)** Illustration of the path length difference caused by a single layer. The propagation angle depends on the local refractive index, hence the path length is non-trivial. **b)** Exemplary partial waves in a Bragg-Mirror for angle of incidence $\theta = 45\,\text{deg}$. The highest reflectivity (at normal incidence $\theta = 0\,\text{deg}$) is achieved by choosing the thickness of each layer as $d_j = \lambda/4n_j$ for constructive interference of all reflected partial waves. Note that in reality, the incident beam is regarded as a planar wave front instead of a single ray.

supermirrors with $R \gtrsim 99.99\,\%$ the absorption and scattering losses $A \approx 5 \ldots 20\,\text{ppm}$ become significant. Reflectance, transmittance T and losses A are connected via $R + T + A = 1$. The transmission can acquire arbitrary low values while the reflectivity value is limited by material imperfections and depends on e.g. substrate quality and the coating process [130]. In the visible regime (contrary to infrared), $R = 99.999\,\%$ is mostly unreached. Commonly used materials are SiO_2 in combination with Ta_2O_5 ($n \approx 2.15$) or Nb_2O_5 ($n \approx 2.35$) [130].

Empirically one finds that if light approaches the layer stack from a medium with refractive index $\tilde{n}$, the transmission within the stop band is typically increased by this very factor $\tilde{n}$ with respect to vacuum/air due to the better index matching between the topmost layer and the medium.

A.2 Transmission Profiles of Commonly Used Mirrors

In Fig. A.3 are shown calculated transmission profiles of commonly used mirrors in our experiments. Parameters are

Mirror Type	Layer Structure
CRD550	13 alternating pairs of Nb_2O_5 and SiO_2. One additional Nb_2O_5 layer on top.
LO550	19 alternating pairs of Ta_2O_5 and SiO_2. One additional Ta_2O_5 layer on top.
LO2019	Custom coating, roughly speaking: Two stacked Bragg mirrors made of Ta_2O_5 and SiO_2: 18 layer pairs with $\lambda_0 = 570\,\text{nm}$ on top of 18 layer pairs with $\lambda_0 = 700\,\text{nm}$. Individual layer thicknesses were refined by the Laseroptik company.

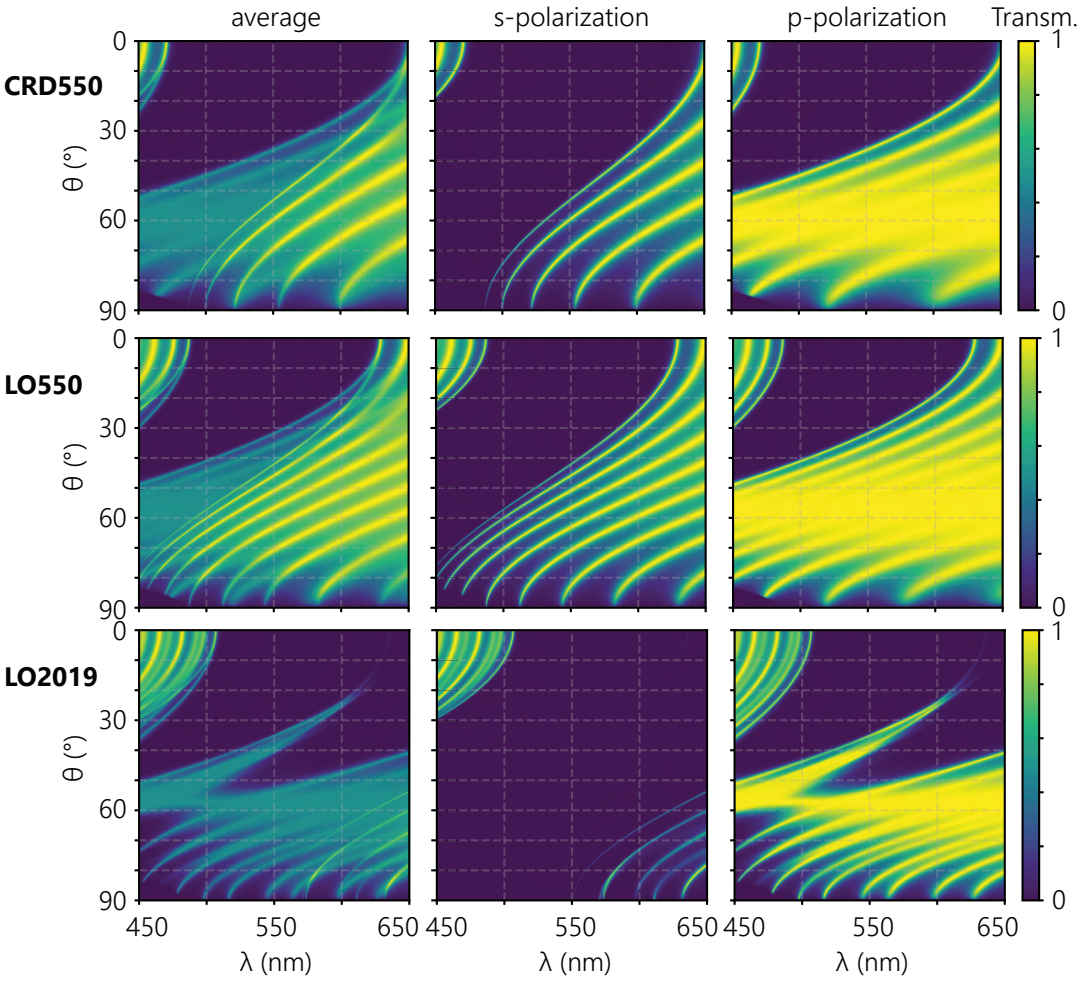

Fig. A.3: Calculated transmission profiles of various mirrors types in an environment with refractive index ($\tilde{n} \approx 1.44$).

References

1. Gowlett, J. A. *The discovery of fire by humans: a long and convoluted process.* Philosophical Transactions of the Royal Society B: Biological Sciences **371,** 20150164 (2016) (cit. on p. 1).
2. Ludlow, A. D., Boyd, M. M., Ye, J., Peik, E. & Schmidt, P. O. *Optical atomic clocks.* Reviews of Modern Physics **87,** 637 (2015) (cit. on p. 1).
3. Meinardi, F. *et al. Large-area luminescent solar concentrators based on 'Stokes-shift-engineered' nanocrystals in a mass-polymerized PMMA matrix.* Nature Photonics **8,** 392–399 (2014) (cit. on p. 1).
4. Van Sark, W. G. *et al. Luminescent Solar Concentrators-A review of recent results.* Optics express **16,** 21773–21792 (2008) (cit. on pp. 1, 13).
5. Welford, W. *Connections and transitions between imaging and nonimaging optics.* in International Conference on Nonimaging Concentrators. **441** (1984), 7–9 (cit. on pp. 1, 13).
6. Bloch, I., Dalibard, J. & Zwerger, W. *Many-body physics with ultracold gases.* Reviews of modern physics **80,** 885 (2008) (cit. on p. 1).
7. Diehl, S. *et al. Quantum states and phases in driven open quantum systems with cold atoms.* Nature Physics **4,** 878–883 (2008) (cit. on p. 1).
8. Carusotto, I. & Ciuti, C. *Quantum fluids of light.* Reviews of Modern Physics **85,** 299 (2013) (cit. on p. 1).
9. Bose, S. N. *Plancks Gesetz und Lichtquantenhypothese.* Z. Phys **26,** 178 (1924) (cit. on p. 1).
10. Einstein, A. *Quantentheorie des einatomigen idealen Gases* (Preussische Akademie der Wissenschaften, 1924) (cit. on p. 1).
11. Einstein, A. *Quantentheorie des einatomigen idealen Gases - Zweite Abhandlung.* Sitzungsberichte der Preussischen Akademie der Wissenschaften, 3 (1925) (cit. on p. 1).
12. Anderson, M. H., Ensher, J. R., Matthews, M. R., Wieman, C. E. & Cornell, E. A. *Observation of Bose-Einstein Condensation in a Dilute Atomic Vapor.* Science **269,** 198 (1995) (cit. on pp. 1, 4).
13. Davis, K. B. *et al. Bose-Einstein condensation in a gas of sodium atoms.* Physical review letters **75,** 3969 (1995) (cit. on p. 1).
14. Gaunt, A. L., Schmidutz, T. F., Gotlibovych, I., Smith, R. P. & Hadzibabic, Z. *Bose-Einstein condensation of atoms in a uniform potential.* Physical Review Letters **110,** 200406 (2013) (cit. on pp. 1, 5).
15. Mukherjee, B. *et al. Homogeneous atomic Fermi gases.* Physical Review Letters **118,** 123401 (2017) (cit. on p. 1).
16. Patel, P. B. *et al. Universal sound diffusion in a strongly interacting Fermi gas.* Science **370,** 1222–1226 (2020) (cit. on p. 1).

17. Christodoulou, P. *et al. Observation of first and second sound in a BKT superfluid.* Nature **594,** 191–194 (2021) (cit. on pp. 1, 88).

18. Ville, J. *et al. Sound propagation in a uniform superfluid two-dimensional Bose gas.* Physical review letters **121,** 145301 (2018) (cit. on pp. 1, 5, 88).

19. Hueck, K. *et al. Two-dimensional homogeneous Fermi gases.* Physical Review Letters **120,** 060402 (2018) (cit. on p. 1).

20. Estrecho, E. *et al. Low-energy collective oscillations and Bogoliubov sound in an exciton-polariton condensate.* Physical Review Letters **126,** 075301 (2021) (cit. on pp. 1, 88).

21. Walker, B. T., Ash, B. J., Trichet, A. A., Smith, J. M. & Nyman, R. A. *Bespoke mirror fabrication for quantum simulation with light in open-access microcavities.* Optics Express **29,** 10800–10810 (2021) (cit. on pp. 1, 55).

22. Klaers, J., Schmitt, J., Vewinger, F. & Weitz, M. *Bose-Einstein condensation of photons in an optical microcavity.* Nature **468,** 545 (2010) (cit. on pp. 2, 5, 13, 14, 65).

23. Marelic, J. & Nyman, R. *Experimental evidence for inhomogeneous pumping and energy-dependent effects in photon Bose-Einstein condensation.* Physical Review A **91,** 033813 (2015) (cit. on pp. 2, 5).

24. Greveling, S., Perrier, K. & van Oosten, D. *Density distribution of a Bose-Einstein condensate of photons in a dye-filled microcavity.* Physical Review A **98,** 013810 (2018) (cit. on p. 2).

25. Vretenar, M., Kassenberg, B., Bissesar, S., Toebes, C. & Klaers, J. *Controllable Josephson junction for photon Bose-Einstein condensates.* Physical Review Research **3,** 023167 (2021) (cit. on pp. 2, 55).

26. Karkihalli Umesh, K. *Investigation of 3D-printed potentials for photon gases.* masters thesis (Universität Bonn, 2021) (cit. on pp. 2, 88).

27. Weill, R., Bekker, A., Levit, B. & Fischer, B. *Bose–einstein condensation of photons in an erbium–ytterbium co-doped fiber cavity.* Nature communications **10,** 1–6 (2019) (cit. on p. 2).

28. Navon, N., Nascimbene, S., Chevy, F. & Salomon, C. *The equation of state of a low-temperature Fermi gas with tunable interactions.* Science **328,** 729–732 (2010) (cit. on p. 2).

29. Ho, T.-L. & Zhou, Q. *Obtaining the phase diagram and thermodynamic quantities of bulk systems from the densities of trapped gases.* Nature Physics **6,** 131–134 (2010) (cit. on p. 2).

30. Yefsah, T., Desbuquois, R., Chomaz, L., Günter, K. J. & Dalibard, J. *Exploring the thermodynamics of a two-dimensional Bose gas.* Physical Review Letters **107,** 130401 (2011) (cit. on p. 2).

31. Hung, C.-L., Zhang, X., Gemelke, N. & Chin, C. *Observation of scale invariance and universality in two-dimensional Bose gases.* Nature **470,** 236–239 (2011) (cit. on p. 2).

32. Ku, M. J., Sommer, A. T., Cheuk, L. W. & Zwierlein, M. W. *Revealing the superfluid lambda transition in the universal thermodynamics of a unitary Fermi gas.* Science **335,** 563–567 (2012) (cit. on p. 2).

33. Mordini, C. *et al. Measurement of the canonical equation of state of a weakly interacting 3d bose gas.* Physical Review Letters **125,** 150404 (2020) (cit. on p. 2).

34. Nolting, W. *Grundkurs Theoretische Physik. 6. Statistische Physik* (Springer, 2014) (cit. on pp. 3, 9).

35. Stephan, K. & Mayinger, F. *Thermodynamik: Grundlagen und technische Anwedungen: Band 2: Mehrstoffsysteme und chemische Reaktionen* (Springer-Verlag, 2013) (cit. on p. 3).

36. Jackson, J. D. *Classical electrodynamics* 1999 (cit. on p. 3).

37. Pauli, W. *Über den Zusammenhang des Abschlusses der Elektronengruppen im Atom mit der Komplexstruktur der Spektren.* Zeitschrift für Physik **31,** 765–783 (1925) (cit. on p. 3).
38. Yang, L.-P., Khosravi, F. & Jacob, Z. *Quantum spin operator of the photon.* arXiv preprint arXiv:2004.03771 (2020) (cit. on p. 4).
39. Pethick, C. J. & Smith, H. *Bose–Einstein condensation in dilute gases* (Cambridge university press, 2008) (cit. on pp. 4, 8, 29).
40. Ulitzsch, J., Babik, D., Roell, R. & Weitz, M. *Bose-Einstein condensation of erbium atoms in a quasielectrostatic optical dipole trap.* Physical Review A **95,** 043614 (2017) (cit. on p. 4).
41. Kasprzak, J. *et al. Bose–Einstein condensation of exciton polaritons.* Nature **443,** 409–414 (2006) (cit. on pp. 5, 32).
42. Jaeger, G. *The Ehrenfest classification of phase transitions: introduction and evolution.* Archive for history of exact sciences **53,** 51–81 (1998) (cit. on pp. 5, 32).
43. Max, P. *Zur theorie des gesetzes der energieverteilung in normalspectrum.* Verh. Deutsch. Phys. Gesell. **2,** 237–245 (1900) (cit. on p. 5).
44. Einstein, A. *Zur Quantentheorie der Strahlung, Deutsche Physikalische Gesellschaft.* Verhandlungen **16,** 47–62 (1916) (cit. on p. 5).
45. Einstein, A. *Strahlungsemission und -absorption nach der Quantentheorie.* Verh. Deutsch. Phys. Gesell. **18,** 318–323 (1916) (cit. on p. 5).
46. Kuypers, F. *Klassische Mechanik* (John Wiley & Sons, 2016) (cit. on p. 6).
47. Maxwell, J. C. *V. Illustrations of the dynamical theory of gases.—Part I. On the motions and collisions of perfectly elastic spheres.* The London, Edinburgh, and Dublin Philosophical Magazine and Journal of Science **19,** 19–32 (1860) (cit. on p. 6).
48. Heisenberg, W. *Über den anschaulichen Inhalt der quantentheoretischen Kinematik und Mechanik.* Zeitschrift für Physik **43,** 172–198 (3-4 1927) (cit. on p. 7).
49. Wiener, N. *Generalized harmonic analysis.* Acta mathematica **55,** 117–258 (1930) (cit. on p. 8).
50. Khintchine, A. *Korrelationstheorie der stationären stochastischen Prozesse.* Mathematische Annalen **109,** 604–615 (1934) (cit. on p. 8).
51. Hadzibabic, Z. & Dalibard, J. *Two-dimensional Bose fluids: An atomic physics perspective.* La Rivista del Nuovo Cimento **34,** 389–434 (2011) (cit. on pp. 8, 30, 88).
52. Naraschewski, M. & Glauber, R. *Spatial coherence and density correlations of trapped Bose gases.* Physical Review A **59,** 4595 (1999) (cit. on p. 8).
53. Wigner, E. *On the Quantum Correction For Thermodynamic Equilibrium.* Phys. Rev. **40,** 749–759 (5 1932) (cit. on p. 8).
54. Damm, T. *Kalorimetrie und Phasenkorrelationen eines zweidimensionalen Photonengases.* PhD thesis (Universitäts-und Landesbibliothek Bonn, 2017) (cit. on p. 8).
55. Damm, T., Dung, D., Vewinger, F., Weitz, M. & Schmitt, J. *First-order spatial coherence measurements in a thermalized two-dimensional photonic quantum gas.* Nature communications **8,** 158 (2017) (cit. on pp. 8, 13, 88).
56. Pitaevskii, L. & Stringari, S. *Bose-Einstein condensation and superfluidity* (Oxford University Press, 2016) (cit. on pp. 9, 11).
57. Fließbach, T. *Statistische Physik: Lehrbuch zur Theoretischen Physik IV* (Springer-Verlag, 2018) (cit. on pp. 10, 88).
58. Huang, K. *Statistical mechanics* (1987) (cit. on p. 10).

59. Dung, D. *Variable Potentiale für thermisches Licht und gekoppelte Photonenkondensate*. PhD thesis (Universitäts-und Landesbibliothek Bonn, 2018) (cit. on pp. 13, 55, 56, 57, 69, 70).
60. Kurtscheid, C. *et al. Realizing arbitrary trapping potentials for light via direct laser writing of mirror surface profiles*. EPL (Europhysics Letters) **130,** 54001 (2020) (cit. on pp. 13, 55, 57).
61. Damm, T. *et al. Calorimetry of a Bose-Einstein-condensed photon gas*. Nature communications **7** (2016) (cit. on pp. 13, 32, 71).
62. Landau, L. *Lifschitz, Statistical Physics, Chap. XIV* 1958 (cit. on p. 13).
63. Klaers, J., Vewinger, F. & Weitz, M. *Thermalization of a two-dimensional photonic gas in a 'white wall' photon box*. Nature Physics **6,** 512–515 (2010) (cit. on pp. 14, 30).
64. Schmitt, J. *et al. Observation of grand-canonical number statistics in a photon Bose-Einstein condensate*. Physical review letters **112,** 030401 (2014) (cit. on pp. 14, 33).
65. Schmitt, J. *et al. Thermalization kinetics of light: From laser dynamics to equilibrium condensation of photons*. Physical Review A **92,** 011602 (2015) (cit. on pp. 14, 54).
66. Pieper, A. *et al. Biomimetic light-harvesting funnels for re-directioning of diffuse light*. Nature communications **9,** 1–9 (2018) (cit. on p. 14).
67. Lauterborn, W. & Kurz, T. *Coherent optics: fundamentals and applications* (Springer Science & Business Media, 2003) (cit. on p. 15).
68. Klein, M. V. & Furtak, T. E. *Optik* (Springer-Verlag, 2013) (cit. on p. 15).
69. Saleh, B. E. & Teich, M. C. *Fundamentals of photonics* (john Wiley & sons, 2019) (cit. on pp. 16, 24, 50, 89, 90).
70. Lakowicz, J. R. *Principles of fluorescence spectroscopy* (Springer science & business media, 2013) (cit. on pp. 19, 34, 66).
71. *Product Specification, Rhodamine 6G* sigma-aldrich (2010) (cit. on p. 19).
72. Damm, T. *Entwicklung eines farbstoffdurchflossenen Resonatoraufbaus zur Bose-Einstein-Kondensation von Licht*. diploma thesis (Universität Bonn, 2011) (cit. on pp. 20, 45).
73. Lin, C. & Dienes, A. *Study of excitation transfer in laser dye mixtures by direct measurement of fluorescence lifetime*. Journal of Applied Physics **44,** 5050–5052 (1973) (cit. on p. 20).
74. O'Hagan, W., McKenna, M., Sherrington, D., Rolinski, O. & Birch, D. *MHz LED source for nanosecond fluorescence sensing*. Measurement Science and Technology **13,** 84 (2001) (cit. on p. 20).
75. Kasha, M. *Characterization of electronic transitions in complex molecules*. Discussions of the Faraday society **9,** 14–19 (1950) (cit. on p. 20).
76. Kennard, E. *On the thermodynamics of fluorescence*. Physical Review **11,** 29 (1918) (cit. on p. 21).
77. Kennard, E. *The excitation of fluorescence in fluorescein*. Physical Review **29,** 466 (1927) (cit. on p. 21).
78. Stepanov, B. I. *Universal relation between the absorption spectra and luminescence spectra of complex molecules*. in Doklady Akademii Nauk. **112** (1957), 839–841 (cit. on p. 21).
79. Kazachenko, L. & Stepanov, B. *Mirror symmetry and the shape of absorption and luminescence bands of complex molecules*. Optika i Spektroskopiya **2,** 339–349 (1957) (cit. on p. 21).
80. McCumber, D. *Einstein relations connecting broadband emission and absorption spectra*. Physical Review **136,** A954 (1964) (cit. on p. 21).

81. Van Roosbroeck, W. & Shockley, W. *Photon-radiative recombination of electrons and holes in germanium.* Physical Review **94,** 1558 (1954) (cit. on p. 21).
82. Klärs, J. *Bose-Einstein-Kondensation von paraxialem Licht.* PhD thesis (Universität Bonn, 2011) (cit. on pp. 21, 24).
83. Sawicki, D. A. & Knox, R. S. *Universal relationship between optical emission and absorption of complex systems: An alternative approach.* Physical review A **54,** 4837 (1996) (cit. on p. 21).
84. Kubin, R. F. & Fletcher, A. N. *Fluorescence quantum yields of some rhodamine dyes.* Journal of Luminescence **27,** 455–462 (1982) (cit. on p. 21).
85. Magde, D., Wong, R. & Seybold, P. G. *Fluorescence quantum yields and their relation to lifetimes of rhodamine 6G and fluorescein in nine solvents: Improved absolute standards for quantum yields.* Photochemistry and photobiology **75,** 327–334 (2002) (cit. on p. 21).
86. Demchenko, A. P. *Photobleaching of organic fluorophores: quantitative characterization, mechanisms, protection.* Methods and applications in fluorescence **8,** 022001 (2020) (cit. on p. 21).
87. Song, L., Hennink, E., Young, I. T. & Tanke, H. J. *Photobleaching kinetics of fluorescein in quantitative fluorescence microscopy.* Biophysical journal **68,** 2588–2600 (1995) (cit. on p. 21).
88. Demtröder, W. *Laser spectroscopy: basic concepts and instrumentation* (Springer Science & Business Media, 2013) (cit. on p. 22).
89. Nienhuis, G. & Allen, L. *Paraxial wave optics and harmonic oscillators.* Physical Review A **48,** 656 (1993) (cit. on p. 24).
90. Marte, M. A. & Stenholm, S. *Paraxial light and atom optics: the optical Schrödinger equation and beyond.* Physical Review A **56,** 2940 (1997) (cit. on p. 24).
91. Pare, C., Gagnon, L. & Bélanger, P. *Aspherical laser resonators: An analogy with quantum mechanics.* Physical Review A **46,** 4150 (1992) (cit. on p. 25).
92. Schwabl, F. *Quantenmechanik (QM I)* ISBN: 9783540431060 (Springer, 2002) (cit. on p. 26).
93. Jähne, B. *Digitale Bildverarbeitung* (Springer-Verlag, 2005) (cit. on p. 28).
94. *Python package for calculating wavefunctions for 1D and 2D potentials.* `https://github.com/jrjohansson/wavefunction` (2021) (cit. on p. 28).
95. Mermin, N. D. & Wagner, H. *Absence of ferromagnetism or antiferromagnetism in one-or two-dimensional isotropic Heisenberg models.* Physical Review Letters **17,** 1133 (1966) (cit. on p. 30).
96. Penrose, O. & Onsager, L. *Bose-Einstein condensation and liquid helium.* Physical Review **104,** 576 (1956) (cit. on p. 30).
97. Ferrell, R., Menyhard, N., Schmidt, H., Schwabl, F. & Szépfalusy, P. *Fluctuations and lambda phase transition in liquid helium.* Annals of Physics **47,** 565–613 (1968) (cit. on p. 32).
98. Schmitt, J. *et al. Spontaneous symmetry breaking and phase coherence of a photon Bose-Einstein condensate coupled to a reservoir.* Physical review letters **116,** 033604 (2016) (cit. on p. 33).
99. Özturk, F. E. *et al. Fluctuation dynamics of an open photon Bose-Einstein condensate.* Physical Review A **100,** 043803 (2019) (cit. on p. 33).
100. Öztürk, F. E. *et al. Observation of a non-Hermitian phase transition in an optical quantum gas.* Science **372,** 88–91 (2021) (cit. on p. 33).
101. Walker, B. T. *et al. Non-stationary statistics and formation jitter in transient photon condensation.* Nature communications **11,** 1–11 (2020) (cit. on p. 33).

102. Klaers, J., Schmitt, J., Damm, T., Vewinger, F. & Weitz, M. *Statistical physics of Bose-Einstein-condensed light in a dye microcavity*. Physical review letters **108,** 160403 (2012) (cit. on pp. 33, 34).

103. Kirton, P. & Keeling, J. *Nonequilibrium model of photon condensation*. Physical Review Letters **111,** 100404 (2013) (cit. on p. 33).

104. Kirton, P. & Keeling, J. *Thermalization and breakdown of thermalization in photon condensates*. Physical Review A **91,** 033826 (2015) (cit. on p. 33).

105. Keeling, J. & Kirton, P. *Spatial dynamics, thermalization, and gain clamping in a photon condensate*. Physical Review A **93,** 013829 (2016) (cit. on pp. 33, 35, 51, 65, 75).

106. Demtröder, W. *Atoms, molecules and photons* **7** (Springer, 2010) (cit. on p. 33).

107. Jansen, A. P. J. *An introduction to kinetic Monte Carlo simulations of surface reactions* (Springer, 2012) (cit. on p. 37).

108. Bortz, A. B., Kalos, M. H. & Lebowitz, J. L. *A new algorithm for Monte Carlo simulation of Ising spin systems*. Journal of Computational Physics **17,** 10–18 (1975) (cit. on p. 37).

109. Bezanson, J., Edelman, A., Karpinski, S. & Shah, V. B. *Julia: A fresh approach to numerical computing*. SIAM review **59,** 65–98 (2017) (cit. on p. 37).

110. Wahl, C. *Phase Dynamics of a Statistically Flickering Photon Bose-Einstein Condensate*. masters thesis (Universität Bonn, 2014) (cit. on pp. 39, 70).

111. *Manual for Verdi G-Series* Coherent, Inc. (2018) (cit. on pp. 41, 56).

112. *iXon Ultra Hardware Guide v1.1* Andor Technology (2013) (cit. on p. 43).

113. Purcell, E. M. *Proceedings of the american physical society*. Phys. Rev **69,** 674–674 (1946) (cit. on p. 44).

114. Silfvast, W. T. *Laser fundamentals* (Cambridge university press, 2004) (cit. on p. 50).

115. Andreani, L. C., Panzarini, G. & Gérard, J.-M. *Strong-coupling regime for quantum boxes in pillar microcavities: Theory*. Physical Review B **60,** 13276 (1999) (cit. on p. 50).

116. Kristensen, P. T., Van Vlack, C. & Hughes, S. *Generalized effective mode volume for leaky optical cavities*. Optics letters **37,** 1649–1651 (2012) (cit. on p. 50).

117. Mazonka, O. *Solid angle of conical surfaces, polyhedral cones, and intersecting spherical caps*. arXiv preprint arXiv:1205.1396 (2012) (cit. on p. 51).

118. Koyama, K., Yoshita, M., Baba, M., Suemoto, T. & Akiyama, H. *High collection efficiency in fluorescence microscopy with a solid immersion lens*. Applied Physics Letters **75,** 1667–1669 (1999) (cit. on p. 51).

119. Wu, Q., Ghislain, L. P. & Elings, V. *Imaging with solid immersion lenses, spatial resolution, and applications*. Proceedings of the IEEE **88,** 1491–1498 (2000) (cit. on p. 51).

120. Young, A. T. *Rayleigh scattering*. Applied optics **20,** 533–535 (1981) (cit. on p. 53).

121. Dung, D. *et al. Variable potentials for thermalized light and coupled condensates*. Nature Photonics **11,** 565 (2017) (cit. on pp. 55, 57, 88).

122. Kurtscheid, C. *et al. Thermally condensing photons into a coherently split state of light*. Science **366,** 894–897 (2019) (cit. on pp. 55, 65).

123. Bashir-Elahi, D. *Thermo-optically induced microstructured potentials for photonic condensates and all-optical gates*. masters thesis (Universität Bonn, 2015) (cit. on pp. 55, 57).

124. Busley, E. *Coupled Photon Condensates in a Microstructured Double Well Potential*. masters thesis (Universität Bonn, 2016) (cit. on pp. 55, 57, 69, 88).

125. Schilz, C. *Microstructuring and surface characterization of mirror surfaces for optical quantum gas confinement.* masters thesis (Universität Bonn, 2016) (cit. on pp. 55, 69, 70).

126. Redmann, A. *Variable Mirror Structuring for Quantum Gases of Light.* masters thesis (Universität Bonn, 2019) (cit. on pp. 55, 57, 70).

127. Rancourt, J. D. *Optical thin films: user handbook* (SPIE Press, 1996) (cit. on p. 55).

128. Spaepen, F. *Interfaces and stresses in thin films.* Acta materialia **48,** 31–42 (2000) (cit. on p. 55).

129. Ali, M. Y., Hung, W. & Yongqi, F. *A review of focused ion beam sputtering.* International journal of precision engineering and manufacturing **11,** 157–170 (2010) (cit. on p. 55).

130. Laseroptik GmbH. private communication. 2019 (cit. on pp. 56, 91).

131. Gioia, G. & Ortiz, M. *Delamination of compressed thin films.* Advances in applied mechanics **33,** 119–192 (1997) (cit. on p. 56).

132. Wolf, F. *Microstructured Multi-Site Potentials for Quantum Gases of Light.* masters thesis (Universität Bonn, 2021) (cit. on p. 56).

133. Malacara, D. *Optical shop testing* (John Wiley & Sons, 2007) (cit. on p. 58).

134. *Millenia eV Datasheet* Newport Corporation (2021) (cit. on p. 60).

135. *iXon Ultra X-8272 performance sheet* Andor Technology (2013) (cit. on p. 62).

136. Espert Miranda, L. *A Microcavity Apparatus for Homogeneous Photon Gases in a Box.* masters thesis (Universität Bonn, 2021) (cit. on p. 63).

137. Hesten, H. J., Nyman, R. A. & Mintert, F. *Decondensation in nonequilibrium photonic condensates: when less is more.* Physical Review Letters **120,** 040601 (2018) (cit. on pp. 65, 75).

138. Greveling, S., van der Laan, F., Jagers, H. & van Oosten, D. *Polarization of a Bose-Einstein condensate of photons in a dye-filled microcavity.* arXiv preprint arXiv:1712.08426 (2017) (cit. on p. 66).

139. Moodie, R. I., Kirton, P. & Keeling, J. *Polarization dynamics in a photon Bose-Einstein condensate.* Physical Review A **96,** 043844 (2017) (cit. on p. 66).

140. Ketterle, W. & Van Druten, N. *Evaporative cooling of trapped atoms.* Advances in atomic, molecular, and optical physics **37,** 181–236 (1996) (cit. on p. 70).

141. Noda, S., Tomoda, K., Yamamoto, N. & Chutinan, A. *Full three-dimensional photonic bandgap crystals at near-infrared wavelengths.* Science **289,** 604–606 (2000) (cit. on p. 87).

142. Blanco, A. *et al. Large-scale synthesis of a silicon photonic crystal with a complete three-dimensional bandgap near 1.5 micrometres.* Nature **405,** 437–440 (2000) (cit. on p. 87).

143. Nikolaev, I. S., Lodahl, P. & Vos, W. L. *Fluorescence lifetime of emitters with broad homogeneous linewidths modified in opal photonic crystals.* The Journal of Physical Chemistry C **112,** 7250–7254 (2008) (cit. on p. 87).

144. Zhang, F., Deng, Y., Shi, Y., Zhang, R. & Zhao, D. *Photoluminescence modification in up-conversion rare-earth fluoride nanocrystal array constructed photonic crystals.* Journal of Materials Chemistry **20,** 3895–3900 (2010) (cit. on p. 87).

145. Comaron, P. *et al. Dynamical critical exponents in driven-dissipative quantum systems.* Physical review letters **121,** 095302 (2018) (cit. on p. 88).

146. Hohmann, J. K., Renner, M., Waller, E. H. & von Freymann, G. *Three-Dimensional μ-Printing: An Enabling Technology.* Advanced Optical Materials **3,** 1488–1507 (2015) (cit. on p. 88).

147. Stein, E. & Pelster, A. *Thermodynamics of Trapped Photon Gases at Dimensional Crossover from 2D to 1D.* arXiv preprint arXiv:2011.06339 (2020) (cit. on p. 88).

148. Wenger, T., Kinoshita, T. & Weiss, D. *A quantum Newton's cradle*. Nature **440,** 900–903 (2006) (cit. on p. 88).

149. Gladilin, V. N. & Wouters, M. *Vortices in nonequilibrium photon condensates*. Physical Review Letters **125,** 215301 (2020) (cit. on p. 88).

150. König, F. *Nonlinear Kerr Media as a Future Platform for Interacting Photon Condensates*. masters thesis (Universität Bonn, 2018) (cit. on p. 88).

151. Kerkhof, K. *A Nonlinear Optical Cavity for the Realization of Photon-Photon Interactions*. masters thesis (Universität Bonn, 2021) (cit. on p. 88).

152. Larouche, S. & Martinu, L. *OpenFilters: open-source software for the design, optimization, and synthesis of optical filters*. Applied optics **47,** C219–C230 (2008) (cit. on p. 90).

Danksagung

Es ist soweit: Nach knapp über zehn Jahren an der Bonner Universität wird es mit der Promotion allmählich Zeit für neue Wege. Rückblickend möchte ich mich daher bei einigen Personen bedanken, die mich auf diesem prägenden Weg begleitet haben.

In erster Linie dafür natürlich bei Prof. Dr. Martin Weitz für das Angebot meine Dissertation in seiner Arbeitsgruppe anzufertigen. Zusätzlich danke ich Prof. Dr. Sebastian Hofferberth für die unkomplizierte Übernahme des Korreferats.

Weit vorne ist an dieser Stelle auch Dr. Julian Schmitt für die ausgiebige Betreuung in der Anfangs- und Endzeit meiner Arbeit zu nennen zusammen mit Dr. Frank Vewinger, der mir seit der Bachelorarbeit für fachliche Probleme jeder Art zur Verfügung stand.

Was wäre die bis hier zweite Hälfte meines Lebens gewesen ohne Christian "Der Navarro" Kurtscheid, mit wem ich bereits die Schulbank auch später zeitweise das Büro geteilt habe. Mal sehen, wie lange unser Lebenslauf noch identisch bleibt. Während meiner Doktorandenzeit war außerdem Thilo vom Hövel stets mit von der Partie, wenn es galt den Brand nach Kaltgetränken zu stillen.

Ich danke dem Rest der AG Quantenoptik für die familiäre Atmosphäre und besonders meinen Bachelor- und Masterstudenten Fabian König, Frederik Wolf, Kirankumar Karkihalli Umesh und Leon Espert Miranda für die gute Zusammenarbeit.

Außerhalb des Physikalltags verdanke ich viele großartige Momente dem Jazzchor der Uni Bonn, welcher über die Jahre stets eine kleine Parallelwelt zum Arbeitsalltag geschaffen hat. Außerdem erinnere ich mich gerne an die Unternehmungen des "Physikerbowl 2015 n.e.V." und die Gemeinschaft der Physikshow.

Zuletzt danke ich meiner Freundin Nicole für die gemeinsame Lebensgestaltung und dass sie mir in der Endphase dieser Arbeit etwas den Rücken freigehalten hat.